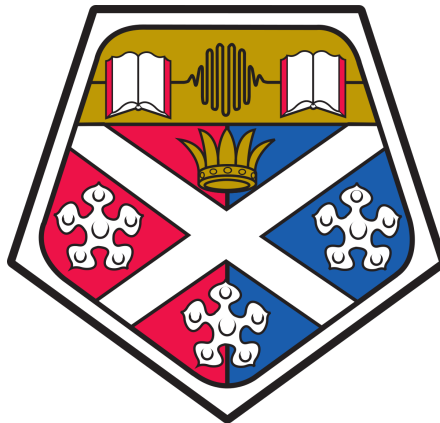# A Dual-Beam Free-Induction-Decay Magnetometer

Allan McWilliam

A thesis presented for the degree of

Doctor of Philosophy

Department of Physics

University of Strathclyde

2024

Abstract

This thesis describes an optically pumped magnetometer system incorporating various microfabricated caesium vapour cells. The experiment operates in a free-induction-decay configuration, where two co-propagating laser sources are used for optical pumping and probing, granting independent control of both. Intense pumping on the D_2 transition line is employed to generate a high spin-polarisation, resulting in excellent performance levels. Magnetic bias field amplitudes of 50 µT emulate the Earth's field in a magnetically shielded laboratory setting. Sensitivities at the $fT/\sqrt{Hz}$ levels are demonstrated in both 3 mm and 6 mm thick cells for tuneable Nyquist-limited sensor bandwidths between 250-500 Hz. A peak sensitivity of 118 ± 11 $fT/\sqrt{Hz}$ is obtained for a 6 mm thick cell.

A novel enhancement to the achievable spin-polarisation created during the optical pumping stage is established, with promising use in real-world sensing applications. This technique also enables heating of the vapour cell to be performed during the conventional dead-time of the sensor. The distribution of the atomic spins is also manipulated to utilise the sensor as an atomic comagnetometer. The extraction of the intrinsic longitudinal relaxation rates from multiple cells, as a function of nitrogen buffer gas pressure content is also undertaken. A minimum relaxation rate of 140 Hz is determined at a pressure of 115 Torr. The versatility of the sensor is also demonstrated with successful 1D and 2D magnetic image reconstructions of DC and AC fields.

Preface/Acknowledgements

Great thanks is due to several people who have assisted me in my journey. Firstly, I would like to express my sincerest gratitude to my principal supervisor, *Erling Riis*, whose expertise, dedication, and drive has been invaluable to me. His motivation and guidance helped shape my research and writing, and his support both inside and outside of the lab over the years has been continually solid. This is greatly appreciated.

Of course, the opportunity to embark on this research journey would not be possible without the confidence instilled by my co-supervisor and lecturer *Paul Griffin*. I thank him for his continuous enthusiasm and encouragement throughout.

Verbalising my work over the previous four years has been challenging, yet also satisfying. I would like to thank the members of my thesis committee, *Gordon Robb* and *Ifan Hughes*, for their time spent reading the document and for an enjoyable discussion, along with constructive critiques and insightful comments.

Enjoying my academic journey is a source of pride, and has validated my decision to pivot into this area. The whole process has made easier from working with several people in the department. Special thanks goes to *Dominic Hunter* for his help and patience throughout. My time has been greatly enhanced from our work together. I would also like to acknowledge *Sean Dyer* for an enjoyable time spent measuring pressures together.

Guidance has also been provided by *James McGilligan*, *Terry Dyer* and *Stuart Ingleby* for which I am extremely grateful. Thank you all for many valuable discussions and helpful advice.

A special thanks goes to the people most close to me. I am extremely appreciative of my family. To my parents, *Peter* and *Elaine*, and sister *Kirsty* who have always

provided unwavering support and encouragement. I wish to extend my total thanks to my partner and best friend *Rachel*, who I have shared this whole experience with.

Next up in our lives together will be an adventure, wherever it takes us.

Contents

List of Figures

Chapter 1

Introduction

1.1 Magnetic Sensing

Magnetic fields permeate the universe, spanning from the macro scale of everyday objects surrounding us to the colossal scale of planetary magnetospheres within our own solar system. The modern age offers an abundance of magnetic subjects for characterisation, ranging from the intricate workings of electronic circuits, the complexities of the human brain, the mapping of Earth's magnetic field, to the measurement of celestial bodies in space. In today's society, both natural and man-made magnetic field sources are ubiquitous, each with associated signatures. Achieving more precise and accurate measurements of these necessitates the continuous progression of sensing technologies.

Historically, magnetic field sensing has played an invaluable role, with the monitoring of our geomagnetic field critical for navigation in previous centuries. The creation of the compass greatly improved the success of maritime expeditions [1, 2]. A plethora of applications now exist in diverse areas such as space [3], archaeology [4], geophysical surveying [5], detecting undetonated ordinance [6], and within the medical field, including magnetocardiography (MCG) [7–9] and magnetoencephalography (MEG) [10–12]. Traditionally, the most sensitive measurements used for monitoring neural activity, have been obtained through superconducting quantum interference devices (SQUIDs), which spearheaded the precision measurement industry [13]. However, their cost, bulkiness, and operational need for cryogenic cooling poses a major impediment.

Responding to the demand for more pragmatic sensing tools across a wide range of applications has led to the development and rise of optically pumped magnetometers (OPMs) [14], along with their integration with microelectromechanical systems (MEMS) vapour cell technology [15]. These scalable devices are progressively evolving into more practical packages that are more robust while maintaining high performance [16].

Providing extremely accurate magnetic field measurements, OPMs operate by monitoring the behaviour of atomic vapour after interacting with resonant laser light. Unlike other technologies, OPMs do not require calibration or suffer from drift, due to the fixed and enduring nature of atoms. Although engineering challenges exist, the inherent properties of these devices are conducive for low maintenance operation, while achieving exemplary levels of precision. The most sensitive sensor to date is the spin-exchange relaxation free (SERF) magnetometer, which operates at near-zero field within shielded enclosures. Arrays of these devices have now been commercialised and utilised as MEG measuring devices [17]. As published in [18], an exceptional sensitivity of 160 aT/$\sqrt{\text{Hz}}$ has been demonstrated in the SERF regime. However, possessing a dynamic range of around 100 nT, these sensors are not readily suitable for portable magnetic sensing applications in unshielded environments i.e the Earth's field of $\sim$ 50 µT.

1.2 Optically Pumped Magnetometers

A significant breakthrough emerged in the 20th century with the first demonstration of optical pumping, as a drastic advancement was born: a higher realisable degree of spin-polarisation. In 1957, optical pumping was extended to induce an atomic orientation in a sample of sodium atoms [19]. This type of work amongst others pioneered our understanding of light-atom interactions. The kHz scale of magnetic resonances provided a technically accessible tool for investigations. OPMs now have a firm foothold in the magnetic sensing industry.

Fundamentally, the core mechanism of an OPM involves measuring the Larmor precession frequency of atomic spins as they precess around an external magnetic field

[20]. A net spin-polarisation in the atomic ground state is induced through optical pumping. The magnetic field exerts a torque on each atom's magnetic moment, μ, via an externally applied field resulting in spin precession. A probe beam facilitates the detection and measurement of this atomic precession, which is directly related to the magnitude of the magnetic field, $\vec{B}$, via the simple relation,

$$\omega_{L} = \gamma \vec{B}, \tag{1.1}$$

where γ is the gyromagnetic ratio, representing the ratio of a particle's magnetic moment to its angular momentum. This ratio varies according to the atomic species. For the ground states of Cs it is approximately 3.5 kHz/μT [21]. Larmor precession is an angular frequency, with $\omega_{L}/2\pi = $ f, the frequency of oscillation. The total measurable time is limited by the spin-relaxation rate. All OPM configurations utilise this fixed atomic precession frequency in a variety of experimental configurations to measure fields such as the Earth's or sources of minute magnetic fields. For example, OPMs are now utilised for studies of neural activity [22–24] emitting signals on the order of 100 fT. They have also been proposed for detecting cosmic axions through nuclear magnetic resonance (NMR) interactions [25]. Each approach comes with its own set of pros and cons. It is productive to consider the design complexities, practicalities and overall performance of each configuration, and assess whether accuracy or sensitivity takes precedence for a given application.

This introduces the OPM sensor utilised in this work: the free-induction-decay (FID) magnetometer [26–28], where the atomic spins are first prepared, e.g. with a strong laser pulse, with their induced precession around a magnetic field then observed as the atomic polarisation decays away due to spin-relaxation. The work during this PhD aims to enhance the prospects of FID sensor integration using MEMS vapour cells for both laboratory based and unshielded sensing purposes. The amalgamation of the FID device with MEMS cells presents promising future sensing exploration in both shielded and unshielded settings. The laboratory based sensor in this work has yielded

$fT/\sqrt{Hz}$ level sensitivities at bias field magnitudes emulating the Earth's, equating to 2-3 parts per billion (ppb) resolution in fractional sensitivity terms.

1.3 Free-Induction-Decay Magnetometer

The FID magnetometer, also commonly referred to as the free-spin-precession magnetometer, stands out as an excellent choice for magnetic sensing purposes. The system is straightforward, sensitive, and versatile. Categorised as a finite field sensor, it detects the total magnetic field, therefore functioning as a scalar measuring device. The FID technique is well established in the field of NMR, where nuclear spins are polarised in a similar fashion to the optically active electrons in this work [29, 30]. An illustration of the process utilised in this work is presented in Fig. 1.1.
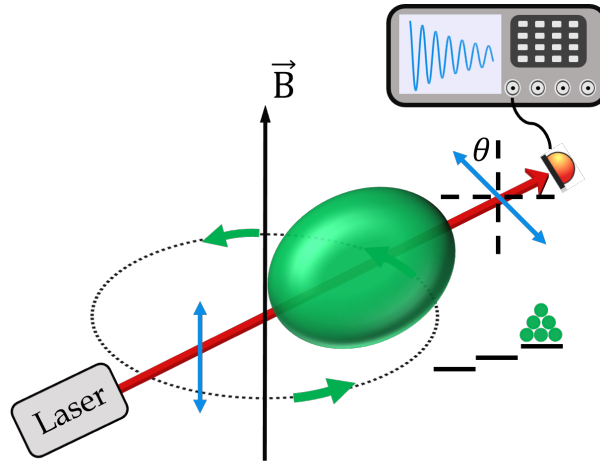
Figure 1.1: Optical pumping of an atomic vapour creates a net spin polarisation in the form of an atomic orientation moment (green). The pump light is then extinguished, allowing the polarised ensemble to precess around a transverse magnetic field, $\vec{B}$ as it also decays due to spin-relaxation. The resulting polarisation rotation of a probe beam (blue) is manifested in the form of an FID signal, which is detected using a balanced polarimeter.

The overall FID process can be separated into three key phases: atomic state preparation, detection of atomic spin-evolution, and subsequent data analysis. The initial step involves polarising the atoms into an asymmetric distribution across the Zeeman state

sublevels through optical pumping. Ideally, most atoms will occupy the stretched Zeeman state. Stretched states have either the maximum, $m_F = F$ or minimum, $m_F = -F$ magnetic quantum number, and are the quantum mechanical equivalent of the classical orientated spin vector. Subsequently, the pump light is extinguished, permitting the atomic ensemble to freely precess around the magnetic field. This precession is detected by capturing transmitted light from a weaker probe beam on a balanced polarimeter which is connected to a data-acquisition (DAQ) device. The induced spin precession causes a polarisation rotation of the probe, generating a signal resembling a decaying sinusoid. Data analysis is relatively simple, as the oscillation frequency, f, is directly proportional to the strength of the magnetic field. A damped sinusoidal fitting process is applied to the data, facilitating an assessment of the relevant signal parameters. Alternative signal analysis methods also exist [31, 32].

Adopting a FID configuration for the purpose of absolute magnetic field measurements is entirely feasible, particularly when integrated with a Ramsey-like detection scheme [33] akin to its use in atomic clocks [34]. In this scheme, the unperturbed atomic evolution offers a definitive measurement of the magnetic field. In comparison to other magnetometry schemes which resonantly drive the sensor such as radio-frequency (RF) [35] or double-resonance [36, 37] magnetometers, the FID approach excels in providing extremely high accuracy. As a result, the technique is used to calibrate the field producing coils in other OPM experiments [38–40]. The accuracy of a sensing device is paramount for measuring fundamental physical constants [41] and for mapping of the Earth's field [42].

Additionally, the sensor boasts a wide dynamic range, enabling its implementation in both magnetically shielded or unshielded environments. Earth's ambient field is susceptible to deviations, therefore, employing a sensor with no need for prior knowledge of the field is beneficial, in particular for portable measurements [43]. In FID systems, the precession frequency is obtained directly giving advantages over driven magnetometer methods which can be subject to frequency shifts and phase errors in the feedback signal [27]. Its fully optical nature also circumvents the issue of crosstalk between the network of adjacent sensors necessary in contemporary OPM-MEG studies.

1.4 Microfabricated Vapour Cells

OPM sensor heads typically feature a singular atomic vapour species, which are either fashioned using traditional glass-blowing techniques [44], or produced via wafer-scale microfabrication [45]. However, in certain cases, they may incorporate multiple species i.e. in atomic comagnetometers. The vapour cell-design approaches differ in terms of scalability and cost, with the larger glass-blown cells being more realistically suited for fixed-laboratory experiments requiring long atomic coherence times. A larger cell provides a longer measuring time, which translates to obtaining higher magnetic sensitivities (assuming proper experimental practices are adhered to), at the expense of sensor bandwidth. FID configurations using glass blown cells have demonstrated sensitivities in the $fT/cm/\sqrt{Hz}$ levels in gradiometric configurations, [46] including in unshielded environments [47]. However, these types of cells are not suited for efficient or mass production and are therefore not a scalable technology.

Accordingly, MEMS vapour cells are the chosen magnetic sensing elements used in this work [16]. These are firmly established in both quantum sensing applications and for precise measurements of time. Their capacity for mass production at the wafer scale presents immediate cost advantages over their glass-blown cell counterparts. Over 100 constituent cells with yields exceeding 90 % [48] have been demonstrated on single silicon wafers, with custom geometries and multi-chamber designs realisable [49]. Furthermore, their smaller footprint facilitates their integration into deployable, portable sensing packages. An example wafer containing Cs MEMS vapour cells prior to constituent cell dicing is displayed in Fig. 1.2.

MEMS cell fabrication will continue to be a favourable route towards producing magnetic sensing devices. The production of these are key for ubiquitous deployment of sensors outside of research laboratories. As the demand for sensitive and stable measurements increases, there is a corresponding requirement for improved cell design and properties.

6
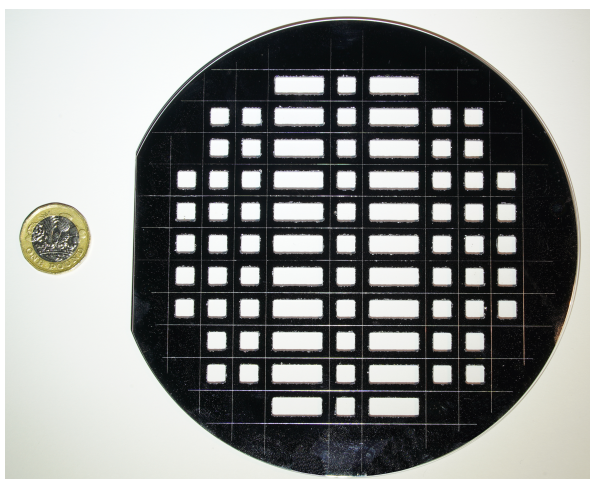
Figure 1.2: A 3 mm thick silicon wafer before dicing. The 8" wafer accommodates various Cs MEMS vapour cells of different dimensions, allowing for streamlined and efficient manufacturing.

All OPM cell design strategies employ measures to reduce the rate of atomic spin-relaxation. However, after a period, atomic-wall depolarisation inevitably occurs. Anti-relaxation coatings have been successfully used in glass blown vapour cells for decades. This technique is not translatable to MEMS vapour cells, as the high temperatures necessary for anodic bonding during cell fabrication ($\simeq$ 300 °C) exceeds the coated layers melting point [14]. Coatings such as paraffin are used as they exhibit a weak adsorption energy for colliding atoms, reducing their total contact time, and in some cases allowing thousands of impacts before depolarisation [50]. The extent to which atomic coherence is maintained is dependent on the quality of applied coating, and therefore, the skilled practitioner. This is in contrast to MEMS cells which incorporate a buffer gas to slow the atomic diffusion process and reduce the wall collision rate.

Selecting a sensor for magnetometry involves many factors including the atomic species, cell size and dimensions, and buffer gas pressure [51]. A single species, and also a single isotope is preferential. The species used for this work is caesium (Cs) due to the higher vapour pressure compared to rubidium (Rb) and potassium (K) at similar temperatures meaning there is less power required, providing a benefit for portability [52, 53]. Additionally, each vapour cell also contains N_2 as a buffer gas.

1.5   Thesis Structure

This thesis strives to showcase the potential of MEMS vapour cells using a FID magnetometer. Chapter 2 covers the fundamental principles of OPMs, encompassing atom-field and atom-light interactions, with a specific focus on atomic behavior within the framework of MEMS vapour cell technology. Chapter 3 details the core mechanisms of the FID technique, including a description of the experimental arrangement predominately employed in this work. A characterisation of noise in the system is also provided, along with a description of the signal fitting process and an overview of the sensitivity estimation. Furthermore, it provides additional insights into accurately assessing the ground-state relaxation rate.

The subsequent chapters focus on noteworthy achievements from developing the system throughout this work. Chapter 4 introduces a novel spin-polarisation technique, which is used consistently throughout the remainder of the thesis. This method displays promise for effective use in real world applications. The initial sections of this chapter involves the work presented in the publication by Hunter *et al.* [32]. The latter part of the chapter (Section 4.4) explores utilising an equitable atomic distribution for comagnetometry purposes. Chapter 5 offers an overview of the performance of MEMS vapour cells as a function of buffer gas pressure. This study involved the extraction of the point of the minimum intrinsic relaxation rate, along with a display of the sensitivity performance. This builds on the results published by Dyer *et al* in [54] in which a controlled N_2 depletion was performed. A publication of the findings in this chapter is in preparation. The utility of the FID technique is further explored in Chapter 6, with a demonstration of its effectiveness for magnetic imaging. The outcomes from this Chapter have been previously described in [55].

Publications Arising from this Work

- S. Dyer, A. P. McWilliam, D. Hunter, S. Ingleby, D. P. Burt, O. Sharp, F. Mirando, P. F. Griffin, E. Riis, and J. P. McGilligan, "Nitrogen buffer gas pressure tuning in a micro-machined vapor cell" Applied Physics Letters; **123**: 074001 (2023).

- D. Hunter, C. Perrella, A. P. McWilliam, J. P. McGilligan, M. Mrozowski, S. Ingleby, P. F. Griffin, D. P. Burt, A. Luiten, and E. Riis, "Free-induction-decay magnetic field imaging with a microfabricated Cs vapor cell" Optics Express **31**, 33582-33595 (2023).

- D. Hunter, M. Mrozowski, A. P. McWilliam, S. Ingleby, T. Dyer, P. F. Griffin, and E. Riis,"Optical pumping enhancement of a free-induction-decay magnetometer" Journal of the Optical Society of America B **40**, 2664-2673 (2023).

- A. P. McWilliam, S. Dyer, D. Hunter, M. Mrozowski, P. F. Griffin, J. P. McGilligan, and E. Riis, "Longitudinal spin-relaxation optimization for miniaturized optically pumped magnetometers" *In preparation*

Chapter 2

Atomic Magnetometry Theory

A description of MEMS vapour cells is provided in this chapter. The structure of the Cs atom, which is a member of the alkali-metals and is situated in group 1A of the periodic table is then examined. Following this, the interaction and behaviour of atoms in the presence of a magnetic field is discussed. The latter sections delve into light-atom interactions, encompassing the influence of N_2 buffer gas on the optical spectra. Subsequently, the focus shifts to an explanation of the optical pumping process used to manipulate the atoms into specific Zeeman sublevel states, along with the atom-probe interaction key for detection. The chapter concludes by detailing the depolarising mechanisms which begin to occur immediately after the optical pumping sequence, leading to the loss of spin-coherence.

2.1   MEMS Cell Fabrication

The vapour cells in this work have been manufactured by Texas Instruments (TI), Kelvin Nanotechnology (KNT), and at the University of Strathclyde (UoS), with cell thicknesses of 1.5 mm, 3 mm and 6 mm. The author was not directly involved in the cell manufacture, therefore only an outline of this is provided. Fig 2.1 displays an example of the various cell thicknesses and designs, all of which have been utilised in this work.
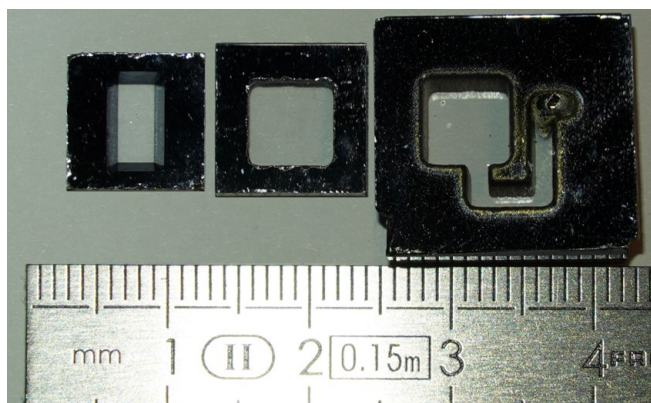
Figure 2.1: 1.5 mm, 3 mm and 6 mm thick MEMS cells investigated in this work. The smallest cell dimension limits the performance of the OPM device.

The fabrication of all cells involved a common approach of anodically bonding silicon wafers to glass wafers [16, 56]. An overview of the anodic bonding procedure is described in [54]. However, the cell manufacturing techniques have incorporated different approaches for each constituent cell design, etching of the cell, and the subsequent alkali deposition and activation method. A brief description for each fabrication procedure is provided below.

2.1.1   Etching

Individual cells on a silicon wafer are initially etched into the desired cell geometry via a wet-etch or water-jet cut process. A wet-etch was applied for the 1.5 mm thick cells. The wet-etch technique results in the cavities of the cell exhibiting a trapezoidal cross section. The lower surface of the cell cavities are etched in the (100) plane with the sides of the cell cavities etched in the (111) crystal direction, leading to an angle of 35.3° to the vertical axis [51], easily visible on the 1.5 mm thick cells. The sloping walls of the wet-etch technique becomes a problem due to the reduction in cell volume. Additionally, wet-etching becomes technically challenging and time consuming for thicker wafers. Hence, a new technique was required as these became available.

Water-jet cutting is a fairly straightforward method for cell fabrication which combines an abrasive mixture with a high-pressure water-jet. The water-jet approach was

11

successfully employed for both the 3 mm [55] and 6 mm thick cells [54] implemented in this work. A cuboid cell geometry was produced for the 3 mm cells, whereas both cuboid and cylindrical cell geometries were created for the 6 mm thick cells.

2.1.2 Caesium-azide Cells

Cells produced by TI (1.5 mm thick) and KNT (3 mm thick) involved applying an aqueous Cs-azide solution (CsN_3) [57] to each individual cell [26]. In the first bonding step, borosilicate glass is used to anodically bond to the lower surface of the wafer before the solution is deposited within each cavity. The liquid then evaporates and another glass wafer adheres to the surface of the silicon in the second anodic bonding stage, which is carried out under vacuum. The cells can then be irradiated with UV light which results in the dissociation of the azide into Cs and N_2. The UV light process causes a saturation of Cs vapour in the cell which is confirmed by inspecting the cell and observing Cs droplets condensed to the glass walls.

2.1.3 Pill-activated Cells

An alternative approach was incorporated for the 6 mm thick cells, with the alkali source stemming from the the heating of a Cs-dispenser pill [54]. During the second anodic bond stage the wafers are pumped down to a pressure of 10^{-5} Torr. Subsequently, N_2 gas is then back-filled across the wafer. The pill consists of a Cs-chromate compound fused with a non-evaporable-getter compound (NEG). The inclusion of the pill serves two purposes; it releases Cs and also acts as a pumping source, thus removing residual gas. The design of these cells in this work involve a dual-chamber structure. This enables the main chamber where the spectroscopic and OPM measurements are performed to be clear, avoiding solid Cs droplets condensing on the glass after irradiation. The dispenser pill is placed in a distinct chamber, adjacent to the science chamber. The two areas are interlinked by a channel allowing the diffusion of Cs from the pill region to the main chamber. A high power laser (3W) is used to activate the pill and release the alkali.

A significant aspect of this thesis relates to a recently explored technique for reducing the N_2 content of a cell through laser irradiation of the dispenser pill. An investigative study into the OPM performance of these vapour cells as a function of buffer gas pressure is presented in Chapter 5. Since Cs-azide is considered hazardous, the ability to bypass this method and instead generate pill-activated cells while sustaining performance levels is favourable.

2.2   Alkali-Metals

The structure of alkali-metal atoms is presented with a description of the various angular momenta within an atomic system. This lays the foundation for describing atom-light and field-atom interactions, which are the primary mechanisms behind magnetic measurements using OPMs. Alkali-metal atoms in a vapour phase serve as extremely suitable platforms for magnetic sensing due to them having only one optically active unpaired valence electron in their outermost energy shell. This property enables an approximation in which only the atomic nucleus and this single valence electron are considered. Conveniently, the nature of this atomic structure allows this electron to be manipulated into desired energy levels, made possible experimentally through optical interaction. Numerous diode lasers capable of stabilising to a specific hyperfine transition for state preparation (optical pumping) and read-out (probing) are readily accessible.

2.2.1   Atomic Structure

Firstly, electrons exhibit two fundamental angular momentum properties: orbital angular and spin angular momentum. The total orbital angular momentum $\vec{L}$ emerges from the electron's motion around the nucleus and is restricted to values between $0 \leq L \leq n - 1$, with n representing the principal quantum number. In alkali-metal atoms the solitary valence electron inhabits the outer subshell, characterised as a 6s shell, with orbital angular momentum equal to 0. The valence electron possesses a spin value of S = 1/2, with the total spin angular momentum of an electron occupying the

ground state $\vec{S} = 1/2$. The coupling of $\vec{L}$ and $\vec{S}$ yields the total angular momentum of the electron $\vec{J} = \vec{L} + \vec{S}$, with $\vec{J}$ confined to values within the range $|L - S| \leq J \leq L + S$. Consequently, for the ground state $J = 1/2$.
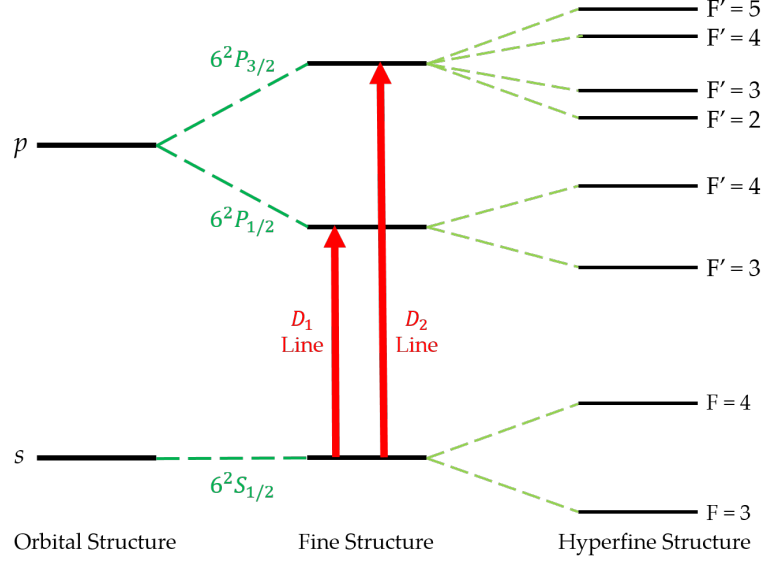
Figure 2.2: Energy structure of the ground states and first excited states of a Cs atom. Includes the orbital structure, fine-structure splitting, hyperfine structure splitting, and the D_1 and D_2 optical transition lines.

The orbital structure exhibits a splitting known as fine-structure splitting, resulting from spin-orbit coupling, which arises due to the interaction between the electron's spin and the magnetic field generated by its orbital motion. The structure of the first excited state, denoted as a 6p shell bearing orbital angular momentum $L = 1$, is divided into separate fine-structure splittings $6^2P_{1/2}$ and $6^2P_{3/2}$ for $J = 1/2$ and $J = 3/2$ respectively. Electron transitions from the ground to each excited state is possible through interaction with resonant laser light. These excitation routes are referred to as D_1 $(6^2S_{1/2} \rightarrow 6^2P_{1/2})$ and D_2 $(6^2S_{1/2} \rightarrow 6^2P_{3/2})$ transitions, occurring at 894.6 nm and 852.3 nm respectively. The utilisation of these transition lines is ubiquitous throughout atomic physics [14].

Additionally, as a result of the interaction of the electron's angular momentum $\vec{J}$, with the nuclear spin $\vec{I}$, the atomic energy levels experience further separation, leading

to the emergence of hyperfine structure splitting. This gives rise to the total atomic spin, $\vec{F}$, with $\vec{F} = \vec{I} + \vec{J}$. These states can be conceptualised as configurations where the atomic and nuclear spins are aligned in parallel, while the electron spin can be oriented either parallel (F = I + J) or anti-parallel (F = I - J) to both. Values of $\vec{F}$ have magnitudes in the range $|J - I| \leq F \leq J + I$. The nuclear spin for Cs is I = 7/2.

Due to selection rules, the only permitted transitions from the ground to excited state are from F to F' = (0, +1, −1). Therefore, under these constraints there exists four possible transitions for the D_1 line and six possible transitions for the D_2 line. Figure 2.2 displays an energy structure diagram for Cs.

2.3 Field-Atom Interaction

2.3.1 Zeeman Splitting

Each hyperfine level consists of 2F + 1 distinct sublevels, which are called the Zeeman, or m_F sublevels. In the absence of an external magnetic field, these sublevels are degenerate. In an external magnetic field, however, the degeneracy is broken and the states are separated. The field-atom interaction depends on the strength of the magnetic field, with the Hamiltonian described by

$$\mathcal{H}_{B} = \frac{\mu_{B}}{\hbar} \left(g_{S}\vec{S} + g_{L}\vec{L} + g_{I}\vec{I} \right).\vec{B}, \tag{2.1}$$

where μ_B is the Bohr magneton, $\vec{B}$ represents the magnetic field and $\hbar$ is the reduced Planck constant. g_I, g_L and g_S are dimensionless proportionality constants, referred to as Landé g-factors, which represent the nuclear, electron orbital and electron spin g-factors. These constants pertain to their respective angular momentum interactions with the magnetic dipole moment. Values for g_S and g_I have been measured experimentally [58]. g_L has a value approximately equal to 1; however, a slight adjustment exists due to the dependence on the nuclear mass, with $g_L = 1 - m_e/m_{nuc}$ where m_e and m_{nuc} represent the electron and nuclear mass respectively.

As atomic magnetometry centers on the study of induced Larmor precession as

its core aspect, the interaction with the magnetic field is a fundamental concept. An applied magnetic field that results in an energy shift which is smaller than the hyperfine-splitting (i.e. when $E_B << E_{HFS}$) permits the interaction Hamiltonian to be expressed as

$$\mathcal{H}_B = g_F \mu_B \vec{F}.\vec{B},\qquad(2.2)$$

where the Landé g-factor, g_F, following the convention formulated in [59], is given by

$$g_F = \frac{1}{\mu_B}\left(-\frac{\mu_I}{I} \pm \frac{-\mu_J/J + \mu_I/I}{2I + 1}\right),\qquad(2.3)$$

where μ_J and μ_I represent the magnetic moment of the electron and the nuclear magnetic moment. For an electron with L = 0, μ_J = -1.001159652μ_B whereas μ_I = 2.582025μ_N, where μ_N is the nuclear magneton.. The $\pm$ sign in Eq. 2.3 highlights the difference in g_F factors which ultimately leads to opposing directional precession for atoms occupying each hyperfine level. Atoms in F = I - J (F = 3) will precess counter-clockwise to those in F = I + J (F = 4) and at a slightly different frequency (for the same m_F value). These possess respective values of $g_{F=4} \approx 0.250390$ and $g_{F=3} \approx -0.251194$. Although these only differ by $\approx 0.3\%$, a discrepancy of $\Delta_f \approx 560$ Hz emerges for atoms precessing in the respective hyperfine manifolds when $\vec{B}$ = 50 µT. This Zeeman-effect energy shift is expressed by a lowest order approximation given by

$$\Delta E_{|F,m_F\rangle} \approx \mu_B g_F m_F B.\qquad(2.4)$$

This equation describes the linear Zeeman effect, providing a valid representation for weak magnetic fields. In frequency terms this shift between adjacent Zeeman sublevels is expressed as

$$\omega_L = \frac{E_{\Delta_{m_F=1}}}{\hbar} = \frac{g_F \mu_B B}{\hbar} = \gamma B.\qquad(2.5)$$

Equation (2.5) defines the Larmor precession frequency, with $\omega_L = 2\pi f$. In this weak field regime, the energy splitting between adjacent Zeeman sublevels is equal. Stronger

16

magnetic fields present a slightly more challenging description. Conveniently, an exception exists for the case of the ground-state manifold (with angular momentum J = 1/2), which is analytically described by the Breit-Rabi equation [60],

$$E_{|F=,m_F\rangle} = \frac{\Delta E_{HFS}}{2(2I+1)} + g_I \mu_B m_F B \pm \frac{\Delta E_{HFS}}{2} \left(1 + \frac{4 m_F x}{(2I+1)} + x^2 \right)^{1/2}, \qquad (2.6)$$

with $\Delta E_{HFS} = A_{HFS(I+1/2)}$. A_{HFS} is the magnetic dipole constant and x is a parameter constant, which is given by

$$x = \frac{\mu_B B(g_S - g_I)}{\Delta E_{HFS}}. \qquad (2.7)$$
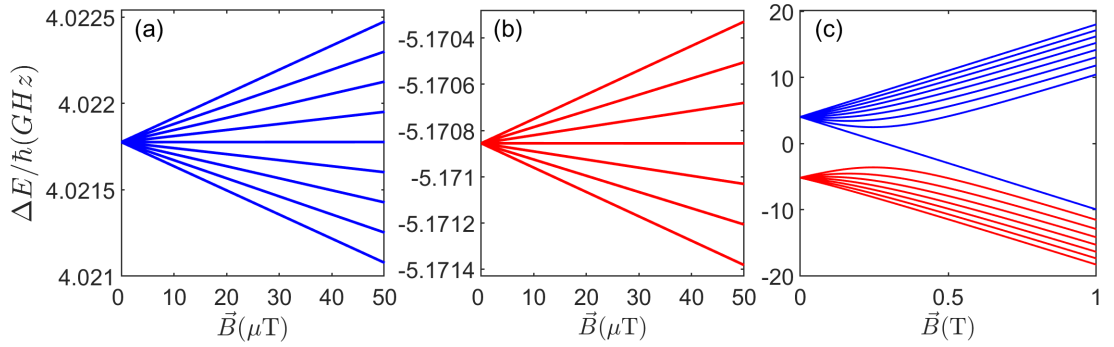
Figure 2.3: Breit-Rabi diagram representing the distinct m_F energy splittings of the $6^2S_{1/2}$ ground state hyperfine structure caused by an external magnetic field. The F = 4 and F = 3 sublevels are displayed in (a) and (b) respectively, for a magnetic field up to $\vec{B}$ = 50 µT. (c) highlights the nonlinear effect at higher fields. At low magnetic field strengths (µT range) the splitting is linear and is referred to as the linear Zeeman effect. Nonlinear splitting occurs as the value of $\vec{B}$ increases.

The exact energies of each m_F ground state sublevel are computed using Eq. 2.6. Figure 2.3 displays the energies of the F = 4 (a) and F = 3 (b) ground state hyperfine levels of Cs for up to a 50 µT field strength, which is pertinent to this work. As illustrated in (c) a linear energy dependence is evident for both low and high magnetic fields, while a nonlinear dependence emerges at intermediate field strengths. At low bias fields of a few µT, where x << 1, a linear approximation describes the energy splitting well. However, at field strengths close to the geomagnetic field range, there is also a small contribution from the second order effect which needs to be considered.

This quadratic phenomenon, known as the nonlinear Zeeman splitting (NLZS) effect, causes a further deviation in the energy (and frequency) between Zeeman sublevels of the same hyperfine level. This can be simplified by neglecting the second order term and approximating $g_I = -0.0004 \approx 0$, leading to the energy splitting between adjacent Zeeman states formulated as,

$$\frac{E_{|F=,m_F+1\rangle} - E_{|F=,m_F\rangle}}{h} = f\left(1 - \frac{f}{f_{HFS}}(2m_F + 1)\right), \qquad (2.8)$$

where $f_{HFS} = 9.193$ GHz describes the frequency difference caused by the hyperfine splitting. This equation can then be utilised to calculate the frequency separation between two adjacent Zeeman sublevels caused by NLZS, denoted as Δf_{NLZS}, through the following,

$$\Delta f_{NLZS} = \frac{2f^2}{f_{HFS}}. \qquad (2.9)$$

The NLZS effect induces a frequency disparity of $\Delta f_{NLZS} \approx 6.7$ Hz between adjacent Zeeman sublevels at a magnetic field strength of 50 µT. In contrast, at lower field strengths (< 10 µT), the frequency disparity Δf_{NLZS} is less than 0.3 Hz, rendering it negligible. Given that much of the work presented in this thesis is focused on emulating the geomagnetic field strength, the impact of Δf_{NLZS} is a factor. It contributes notably to the broadening of the magnetic linewidth, and this broadening, in turn, leads to a quadratic increase in the decohering effect with increasing field strength.

2.4 Light-Atom Interactions

2.4.1 Optical Resonance and Broadening

The Beer-Lambert law governs the extent of light absorption within a vapour cell.

$$I = I_0 e^{-\alpha L}, \qquad (2.10)$$

where, I, is the intensity of transmitted light after passing through the vapour with an

initial intensity I_0. α is the absorption coefficient, its value contingent upon the underlying broadening mechanisms and the characteristics of the atomic species involved. The absorption coefficient of a photon is dependent on the atomic frequency response about the resonance frequency ν_0. L is the path length of the light through the vapour.

For efficient utilisation of atomic transitions, laser light with a narrower linewidth than that of the atomic transition is required. Nevertheless, within OPM systems, several mechanisms contribute to the broadening of these transitions. The atomic structure splitting as described in Section 2.2 gives rise to several possible resonances. Each transition, including the D_1 and D_2 transitions encompasses a spectrum of feasible frequencies governed by the transition linewidth. The natural resonant linewidth of an atomic transition is determined by the natural excited state lifetime, τ. The natural linewidths, Γ_{nat}, of the respective D_1 and D_2 transitions in ^{133}Cs are approximately $\Gamma_{\mathrm{nat}}/2\pi = 4.6$ MHz and 5.2 MHz. This natural linewidth broadening is a mechanism which homogeneously broadens the resonance, and is characterised by a Lorentzian spectral distribution given by

$$\phi_{\mathrm{L}}(\Delta\nu) = \frac{\Gamma_{\mathrm{nat}}/2\pi}{(\Delta\nu)^2 + (\Gamma_{\mathrm{nat}}/2)^2}, \tag{2.11}$$

where $\Delta\nu$ denotes the laser frequency detuning from resonance, and Γ_{nat} represents full width at half maximum (FWHM) of the spontaneous decay rate from the excited state.

Conveniently, most atomic magnetometers operate at temperatures that are at or above room temperature, negating the need for laser cooling [61]. However, this results in a variation in atomic velocities within the sample, given by the temperature dependent Maxwell-Boltzmann distribution, which leads to them encountering a different laser frequency due to the Doppler effect. This results in an inhomogeneously broadened system resulting in a frequency response exhibiting a Gaussian profile

$$\phi_{\mathrm{D}}(\Delta\nu) = \frac{2\sqrt{\ln2/\pi}}{\Gamma_{\mathrm{D}}}\exp\left(\frac{-4\ln2\Delta\nu^2}{\Gamma_{\mathrm{D}}^2}\right), \tag{2.12}$$

with a FWHM described by

$$\Gamma_D = 2\frac{\nu_0}{c}\sqrt{\ln 2 \frac{2k_B T}{m}}, \tag{2.13}$$

where ν_0 is the resonant frequency, c, is the speed of light and k_B is Boltzmann's constant. T and m are the atomic temperature and mass respectively. In a system unaffected by pressure broadening, this temperature-dependent effect emerges as the dominant source of broadening. For example, the D_2 line transition exhibits $\Gamma_D \simeq$ 409 MHz at 80 °C which far exceeds that of Γ_{nat}. This is a common operating temperature for numerous OPM sensors, including those used in this study.

However, the N_2 buffer gas leads to another significant broadening mechanism known as pressure broadening, Γ_{Pr}. This stems from N_2 collisions perturbing the excited Cs atoms through electromagnetic interactions, leading to a shift of the optical resonance and homogeneous broadening of the system. The effect can also be described by a Lorentzian profile and incorporated into Eq. 2.11. Nevertheless, the impact of both the homogeneous and inhomogeneous broadening mechanisms are required to fully describe the overall resonance lineshape, which is possible through a convolution of the two described by the Voigt profile [52, 62],

$$\phi_V(\Delta\nu) = \int_{-\infty}^{\infty} \phi_L(\nu - \nu')\phi_G(\nu' - \nu_0)d\nu', \tag{2.14}$$

which can be rewritten as

$$\phi_V = \frac{2\sqrt{\ln 2/\pi}}{\Gamma_D}f\left(\frac{2\sqrt{\ln 2/\pi}(\Delta\nu - i\Gamma_{nat}/2)}{\Gamma_D}\right), \tag{2.15}$$

where f(x) is the complex error function given by

$$f(x) = \exp(-x^2)\text{erfc}(-ix). \tag{2.16}$$

A more extensive description on the Voigt profile is provided in [51] and [63].

The presence of the N_2 buffer gas imparts a characteristic signature on the observed optical spectra. The first signature effect is the rate of homogeneous pressure broadening, which is denoted by γ_{BN_2}. A secondary effect is the rate of the collisional

frequency shift of the optical resonances denoted by δ_{SN_2}. When N_2 serves as the buffer gas species, a red-shift in the relative frequency is manifested. Other buffer gas species such as He broaden the spectra but causes a relative blue-shift along the frequency axis. These incurred effects are determined from analysis of the spectra in conjunction with a fitted Voigt profile. These rates exhibit a vapour temperature dependence and scale according to the power laws given by [63]:

$$\gamma_{BN_2}(T) = \gamma_{BN_2}(T_r)\left(\frac{T_r}{T}\right)^{0.5}, \tag{2.17}$$

$$\delta_{SN_2}(T) = \delta_{SN_2}(T_r)\left(\frac{T_r}{T}\right)^{0.82}, \tag{2.18}$$

with T and T_r representing the operating and reference temperatures. Numerous works including [64, 65] have attempted to quantify the collisional shift and broadening on the D_1 line of Cs caused by various buffer gases. To deduce that no inadvertent gas species is present in the cell, one can observe a correlation between the ratio of the collisional broadening and shift (i.e. $\gamma_{BN_2}/\delta_{SN_2}$). This does display a slight temperature dependence, however, an agreed ratio in the literature is $\approx 2.24 \pm 0.02$ (D_1 line). The published data in [54], related to Chapter 5 in this thesis agrees with [65] for this ratio. The induced broadening and shift coefficients stand at 19.8 MHz/Torr and - 9.8 MHz/Torr respectively (at 21 °C) . Spectroscopic analysis which results in this consistent ratio throughout multiple measurements verifies that other inadvertent gas species are not present in the cell to a significant extent, and that the broadening and shifts are the result of N_2 alone. Alternative values from various sources are outlined in [51].

2.4.2 Spectroscopy Analysis

The ground states of Cs are separated by 9.193 GHz. The vapour cells that have been explored in this work contain a maximum of 240 Torr of N_2 (at 70 °C) equating to a pressure broadening ≤ 5 GHz. Thus, the ground states have always been optically resolvable. Measurements relating to vapour cells containing sufficiently high buffer gas

pressures which broaden and merge the ground-state transitions have been performed in [51] and [63].
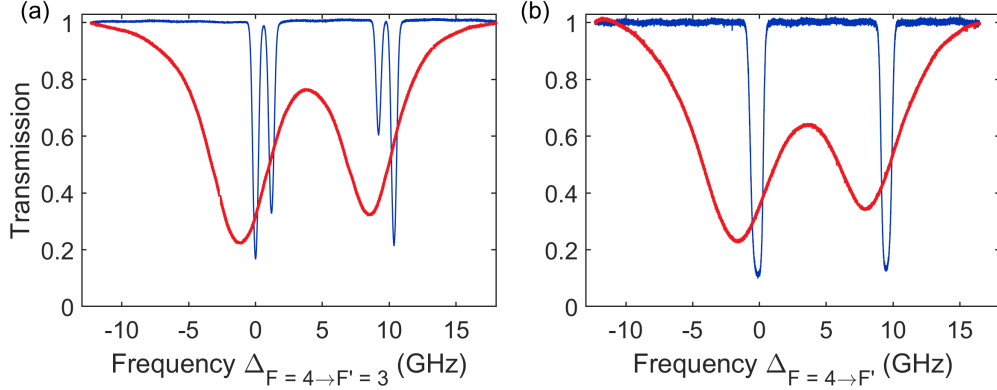
Figure 2.4: D_1 (a) and D_2 (b) absorption profiles for a 3 mm thick Cs MEMS cell containing approximately 220 Torr of N_2 (red) in comparison to a Cs reference cell containing no buffer gas (blue). The vapour cell was heated to a temperature of 80 °C. In (a) the excited states of the Doppler broadened reference cell are spectrally resolvable, whereas in (b) Γ_D is greater than the frequency spacing of the ground to individual excited state transitions. The convention is to display the frequency axis in terms of the relative frequency detuning from the F = 4 to F' = 3 transition.

When utilising the D_1 transition line (F' = 3, 4), the excited states on a Doppler broadened reference cell are spaced 1.38 GHz apart, making them optically resolvable. On the D_2 line however, the transitions (F' = 2,3,4,5) are separated by 151, 201 and 251 MHz respectively. Doppler broadening at room temperature on the D_2 line is $\Gamma_D \simeq 374$ MHz, rendering these unresolvable using a simple absorption spectroscopy setup. One can perform saturated absorption spectroscopy (Doppler-free) in order to distinguish these if so desired [66]. The inclusion of buffer gas however makes this rather redundant since the optical transitions within the MEMS vapour cells are severely collisionally broadened. When quantifying the N_2 content, absorption spectroscopy is performed using the D_1 transition line in this work for this reason. For clarity however, as this work employs lasers operating on both transition lines a comparison of the absorption profiles generated from scanning across these is presented in Fig. 2.4. In both datasets the temperature of the MEMS cell was maintained at 80 °C. The figure highlights the impact of the collisional shift and broadening on the MEMS cell's optical

spectra, consisting of two resolvable peaks.
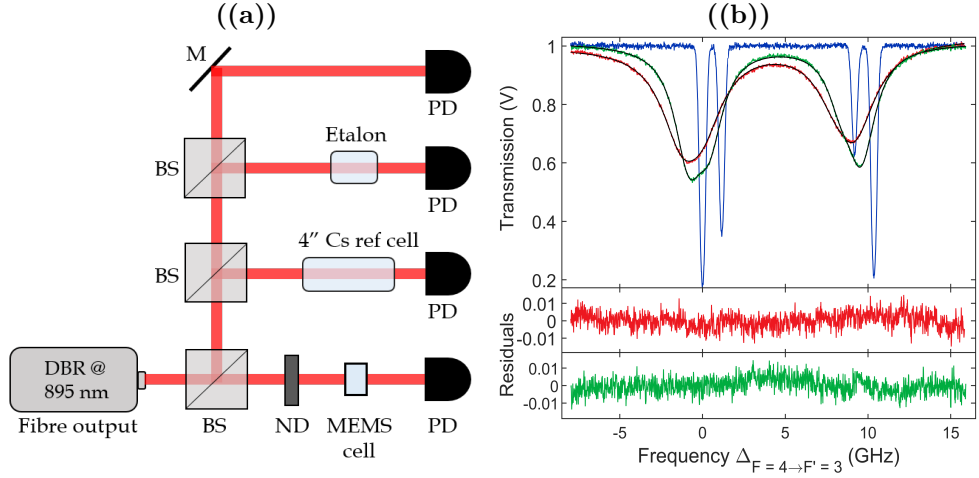
Figure 2.5: (a) Schematic of spectroscopy setup used to characterise the N_2 pressure content. BS: Beamsplitter, M: Mirror, ND: Neutral density filter, PD: Photo-diode. (b) Cs reference cell (blue) and 6 mm thick MEMS cell containing 150 Torr (red) and 100 Torr (green) of N_2 buffer gas. Pressures calculated following a Voigt fit and extracting the induced broadening and shift coefficients. The residuals from the respective fits are shown below highlighting the agreement with the data.

Throughout this work, absorption spectroscopy was performed in order to characterise the N_2 pressure within a variety of vapour cells using the methods described in the previous section. A spectroscopic analysis was performed using a Distributed Bragg Reflector (DBR) laser resonant with the D_1 line using the setup illustrated in Fig. 2.5 (a). Four separate photodiodes monitored the intensity of the laser frequency scan, etalon (Fabry-Perot cavity used to calibrate the laser frequency scan), Cs reference cell and the MEMS cell under study. The intensity monitor was used to normalise intensity variations in the laser, whereas the etalon and reference cell provided a relative and absolute frequency reference [51]. Figure 2.5 (b) displays an example of the collisionally broadened optical spectra as a result of 150 Torr and 100 Torr of N_2 measured at 70 °C. The beam directed towards the MEMS cell involved a $1/e^2$ beam diameter of 1.4 mm, providing an average intensity of 0.75 µW/mm² (3% of I_{Sat}) [58]. Greater broadening and shift rates are evident for the higher pressure cell.

2.4.3   FID Principles

In FID systems, optical pumping is performed using a pulsed approach with the pumping and probing confined to two separate temporal stages [28]. The basic principle is to create a high net polarisation in the atomic ensemble through strong optical pumping and then to switch off this light and monitor the FID with either an independent or a less intense probe laser. This temporal separation enables the polarised spins to precess unperturbed by the intense optical pumping light. An illustration of the basic principle of the FID scheme is displayed in Fig. 2.6.
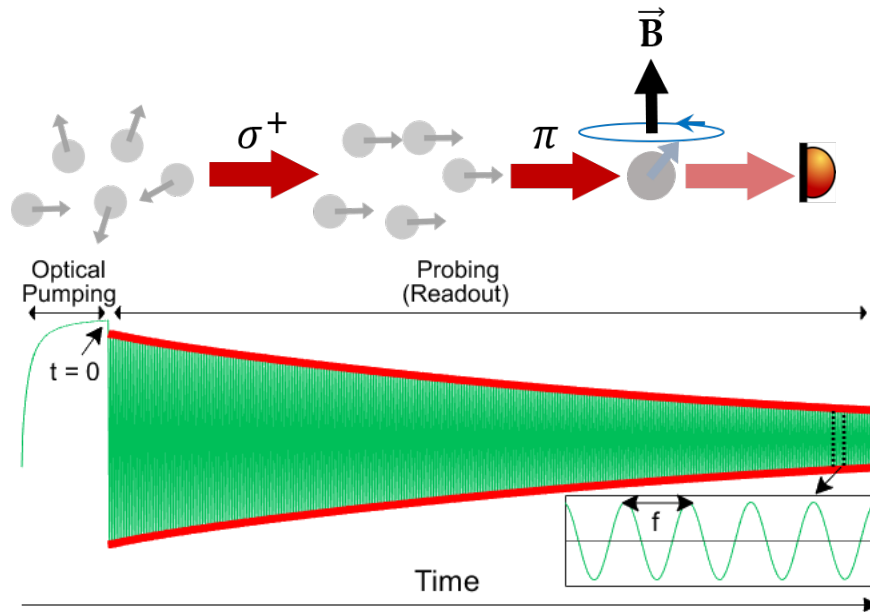
Figure 2.6: Depiction of FID process: The pump and probe stages are separated in the time domain. A circularly polarised optical pumping pulse creates a net spin-orientation in the sample transverse to the magnetic field, $\vec{B}$ before it is then extinguished. Commencing at t = 0, the induced atomic polarisation then precesses around $\vec{B}$, which is detected using a linearly polarised probe beam. An example trace of real FID data is displayed, representing a typical signal obtained throughout this work. The red lines highlight the relaxation envelope caused by several depolarising mechanisms.

2.4.4   Optical Pumping

Optical pumping transfers angular momenta from the laser light source to the atom, proving an effective method for their distribution into specific Zeeman states. In this

work the direction of beam propagation (x) is transverse to that of the applied magnetic field (z). Classically, this transfer of the angular momenta results in the atomic-spin orientation being maximally projected along the beam propagation axis which defines the quantisation axis. This relates to the directional preference along which the spin-polarised atoms become orientated due to the optical pumping light.

The approach in this work is to employ circularly polarised light on the D_2 line. This induces a σ^+ (left-handed) or σ^- (right-handed) transition, transferring angular momentum of $\Delta m_F = +1$ or -1 along the beam propagation axis [67]. The resonant pump light excites atoms to the excited state (F′), until spontaneous emission results in their decay down to a specific Zeeman ground-state sublevel, according to the branching ratios set by the Clebsch-Gordan coefficients.
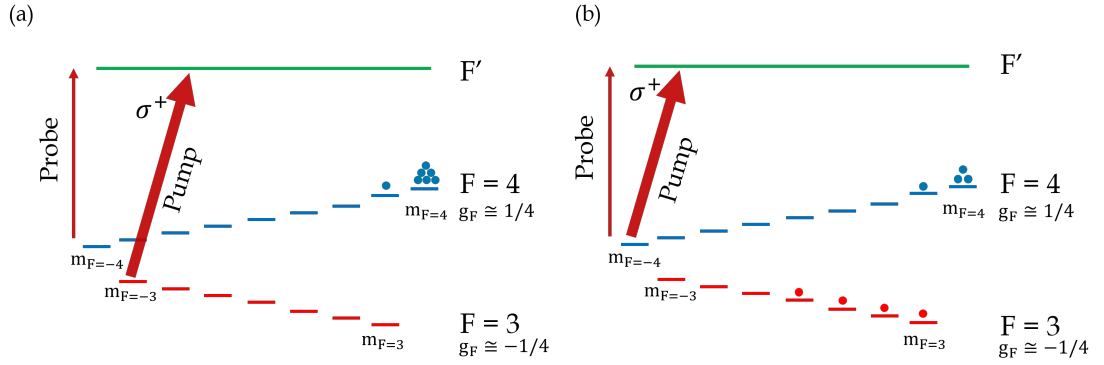
Figure 2.7: Simplified illustration of the optical excitation process for Cs atoms with D_2 line optical pumping. The excited states have been conveyed as one merged state due to the degree of collisional broadening. (a) Pumping on F = 3 leads to a greater atomic polarisation accumulation into a stretched Zeeman state and is therefore a more favourable approach. (b) Pumping on F = 4 will accrue atoms in the F = 4 stretched state, however, they may also escape to F = 3 and become distributed across this level. Here, they are lost from the optical pumping process.

The use of N_2 as a buffer gas offers an additional advantage as it serves as a quenching agent. When atoms in the excited state collide with the quenching gas molecules, they can transfer their excess energy to rotational or vibrational modes. This process enables the excited atoms to transition back to the ground state without emitting a photon. Therefore, this mitigates re-absorption of unpolarised photons, minimising the effect of radiation trapping [68, 69].

Collisional mixing of Cs atoms whilst in the excited states materialises, resulting in a possible redistribution route into either ground state. Nonetheless, optical pumping on the F = 3 to F' transition with circularly polarised light also re-evacuates atoms that have been redistributed to F = 3, thereby, significantly reducing the atomic population present in the F = 3 level. This is akin to the hyperfine-repump technique employed in [70], albeit without an additional laser source. Moreover, the continuous absorption and emission process transfers a large net spin polarisation into a stretched Zeeman state.

The degree of spin-polarisation is equivalent to the proportion of atoms occupying the stretched state, a condition that is enhanced by implementing intense optical pumping, as the results from this thesis will demonstrate. Tuning the pump frequency on resonance to the F = 3 to F' transition achieves a high net polarisation by manipulating atoms into the F = 4 ground state. This boosts the signal, improves the SNR (signal to noise ratio), and also extends the coherence time of the precessing atomic ensemble by circumventing a large degree of depolarising spin-exchange collisions, which are discussed in the next section.

Conversely, when tuning the pump frequency to the F = 4 to F' transition, a significant proportion of atoms are redistributed into both ground states, reducing the overall attainable spin-polarisation in the ensemble. This is illustrated in a simplified diagram in Fig. 2.7. The excited states are conveyed as one level due to the degree of collisional broadening caused by the buffer gas. Further data relating to the impact of pump frequency is presented in this thesis, with a particular focus in Section 4.4, where the distinction between pumping on F = 3 and F = 4 is discussed.

2.4.5 Probing: Detection

As the atoms mainly occupy the F = 4 ground state after optical pumping, the probe beam is detuned by several GHz from this transition and implemented at much lower intensities (typically $\simeq 1$ %). The lower atom-light interaction during the readout stage is vital as it drastically reduces any further perturbation or depolarisation of atoms along the beam propagation axis, preserving the phase coherence of the precessing

ensemble. Detection is performed on the D_1 transition with linearly polarised light, leading to a two-colour pump-probe scheme (see Section 3.1).

Optical rotation of the polarisation plane of the transmitted probe light occurs as a result of the induced macroscopic magnetisation vector precessing transversely to the orientation of the magnetic field. This alters the birefringence of the sample, resulting in the two orthogonal circular components of the linearly polarised probe beam enduring different refractive indices. In the energy level picture, the spin precession corresponds to the population fluctuations between the stretched states with the different atomic interactions occurring depending on which stretched state the atom occupies.
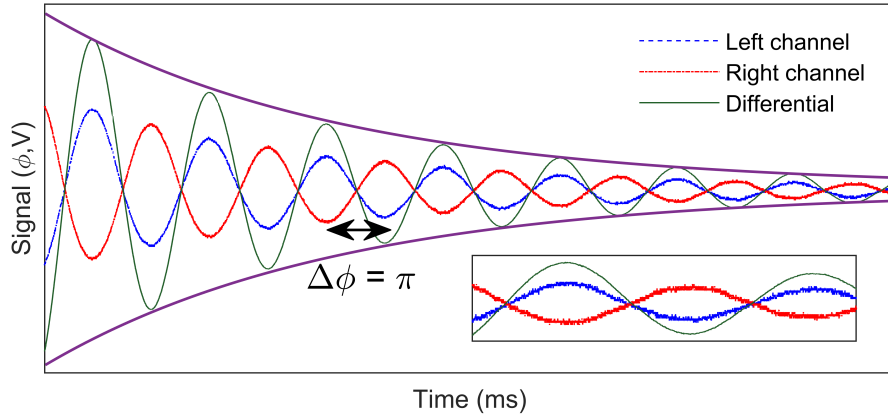
Figure 2.8: Two orthogonal polarisation states of light (blue and red traces) are each directed to a separate channel of a balanced polarimeter. A π phase difference facilitates a differential measurement (green trace), leading to signal enhancement. Additionally, the signal is amplified due to the gain of the detector. The purple lines highlight the temporal profile of the exponentially decaying sinusoidal signal (see Eq. 3.3). A clear reduction in noise is evident through the common-mode noise rejection with a calculated 20 fold improvement in SNR. All data is experimentally obtained, however, for a clearer depiction the amplitudes of the orthogonal polarisation states (blue and red) have been increased by a factor of 27.5.

The FID signal directly represents this optical rotation caused by the atomic precession, with the frequency of oscillation, f, equivalent to the Larmor precession frequency $\omega_L/2\pi = f$. The signal embodies a decaying sinusoid due to the spin-relaxation mechanisms which are described in Section 2.5. Two states of light, corresponding to the y and z projections of the probe light are split into independent channels via a Wollaston

27

prism (WP). These are detected using a balanced polarimeter (connected to a DAQ device) with outputs for both individual channels and a differential output. Subtracting one of the signals from the other is the essence of the differential measurement, which is employed as it produces a greater signal amplitude and higher SNR through common-mode noise rejection. The differential measurement is feasible solely as a result of the π phase difference between the two channels. The light intensity in each channel, I_1 and I_2, described using Malus' law are provided through the following.

$$I_1 = I_0 \sin^2\left(\phi - \frac{\pi}{4}\right) \tag{2.19}$$

$$I_2 = I_0 \cos^2\left(\phi - \frac{\pi}{4}\right) \tag{2.20}$$

The total light intensity before separation is given by I_0. ϕ denotes the polarisation angle of the light with respect to the beam propagation direction. The total intensity on each channel is converted to ϕ through Eq. 2.21 [31].

$$\phi = \arcsin\frac{I_1 - I_2}{2(I_1 + I_2)} \tag{2.21}$$

ϕ is the initial signal amplitude, which is directly related to the spin-polarisation. Typical rotation angles for maximum signal amplitudes obtained were approximately $\phi \approx 70$ mrad ($\pm$ 35 mrad). However, in this thesis, the rotation is presented in units of Volts as the signals are initially obtained in these units. Capturing I_1 and I_2 in addition to the differential channel is data-intensive and unnecessary. After subtraction of one orthogonal light state from the other, amplification is performed by the polarimeter which provides the differential signal. The dynamic range of the detector is $\pm$ 10 V_{pp} which sets the signal saturation limit. An illustration using experimental data containing both individual channels and the differential measurement is provided in Fig. 2.8, where the common-mode noise rejection is evident, demonstrating its advantage.

28

2.5 Spin Relaxation

Maintaining the spin coherence in the sample is crucial for prolonging the measurement time and enhancing the sensitivity of the sensor. However, several decohering mechanisms that limit this time arise from various factors. The magnetic linewidth, which limits the ultimate precision of a magnetic measurement is itself constrained by the transverse atomic coherence lifetime, T_2, and is expressed by

$$\Delta B = \frac{1}{\gamma T_2}. \tag{2.22}$$

T_2 describes the duration during which spin-polarised atoms in the ground state manifold remain coherently precessing together, directly observed via the FID signal. Maximising T_2 is therefore crucial for maximising the sensor performance. Many relaxation processes are intrinsic to the design of the vapour cell. These intrinsic depolarising mechanisms that limit T_2 are presented in this section following the description from [71].

A source of depolarisation in all OPM systems are atomic collisions with cell walls. N_2 buffer gas is critical in reducing the alkali-wall collision rate. However, a high density of buffer gas can also lead to increased depolarisation if the rate at which alkali-buffer gas collisions exceeds the rate at which cell-wall collisions occur. Therefore, an optimal buffer gas pressure that maximises T_2 exists between these two depolarising mechanisms.

The wall relaxation rate, γ_{WC}, for a cylindrical geometry (closely resembling a cuboid geometry used for the majority of this work) is given by [71]

$$\gamma_{WC} = \left[\left(\frac{\pi}{t} \right)^2 + \left(\frac{2.405}{r} \right)^2 \right] \frac{n_0 D_{0:Cs-N_2}}{\eta} \sqrt{\frac{T}{273.15K}}, \tag{2.23}$$

with t and r representing the cell thickness and radius. $D_{0:Cs-N_2}$ is a constant given at 1 amg [1], relating to the diffusion of Cs in the N_2 buffer gas. η is the N_2 number density, whilst n_0 is the Loschmidt constant given at 1 amg.

---

[1] The Amagat (amg) is a unit for number density, representing the quantity of ideal gas molecules within a given volume under standard conditions of temperature and pressure (T = 273 K, P = 1 atm).

The spin-relaxation contribution from Cs-N$_2$ collisions is given by

$$\gamma_{\mathrm{BC}} = \eta\, n_0\, \sigma_{\mathrm{Cs-N_2}}\, \overline{\nu}_{\mathrm{Cs-N_2}}, \tag{2.24}$$

with $\sigma_{\mathrm{Cs-N_2}}$ [2] describing the cross section of $\mathrm{Cs-N_2}$ depolarising collisions. $\overline{\nu}_{\mathrm{Cs-N_2}}$ is the relative thermal velocity between the two elements, which can be calculated through the following relation,

$$\overline{\nu} = \sqrt{\frac{8\mathrm{k_B T}}{\pi \mathrm{m}^*}}, \tag{2.25}$$

where, T, is the temperature and m* is the relative mass. For Cs-N$_2$ collisions this becomes a reduced mass constant given by,

$$\mathrm{m}* = \frac{\mathrm{m_{Cs}}\mathrm{m_{N_2}}}{\mathrm{m_{Cs}} + \mathrm{m_{N_2}}}. \tag{2.26}$$

Minimisation of the relaxation rate occurs at the point of intersection of the crossover of contributions from Eqs. 2.23 and 2.24, which confirms the ideal buffer gas pressure for a given cell geometry.

Depolarising spin-destruction collisions which stem from a spin-polarised Cs atom colliding with another, leading to its complete decoherence is given through the following,

$$\gamma_{\mathrm{SD}} = \mathrm{q}\, \eta_{\mathrm{Cs}}\, \sigma_{\mathrm{SD}}\, \overline{\nu}, \tag{2.27}$$

where, q denotes the nuclear slowing down factor which characterises the extent to which atomic spin coherence is maintained in the polarised ensemble [52]. This parameter varies between values of 1/8 and 1/22 for high and low polarisations respectively [72]. η_{Cs} is the Cs vapour density and σ_{SD} is the spin-destruction cross section

---

[2]Among the literature there is a range of measured values relating to the constants $D_{0:\mathrm{Cs-N_2}}$ and $\sigma_{\mathrm{Cs-N_2}}$. A collated list of these is provided in Table 5.1 where one can see a broad spectrum of measured values, particularly for $\sigma_{\mathrm{Cs-N_2}}$. There is a variability, particularly with a stark difference in values pertaining to the case where larger vapour cell sizes were employed, raising uncertainty on the accuracy of these. These parameters are relevant to this work, where a measurement of intrinsic spin-relaxation rates are presented in Section 5.2.

rate of Cs-Cs collisions. However, this effect is minor in comparison to the other sources of depolarisation.

The overall longitudinal relaxation rate, denoted by γ_{10}, includes all of these described depolarising mechanisms. This nomenclature exists as this occurrence causes the atomic spin vector to become realigned parallel to the magnetic field, thus bringing a halt to any atomic precession generated from optical pumping. The rate at which this occurs is given by,

$$\gamma_{10} = \gamma_{WC} + \gamma_{BC} + \gamma_{SD}. \tag{2.28}$$

For finite-field magnetometers, spin-exchange collisions are a significant source of depolarisation, particularly when operating at elevated vapour densities. These collisions cause atoms precessing in mutual ground-state hyperfine levels to undergo a change of hyperfine state after colliding, with the overall energy being conserved. However, atoms precessing in opposing hyperfine levels have an anti-phase relation and will precess in opposite directions, as illustrated in Fig. 2.9. Therefore, while this occurrence does not cease atomic precession, it acts as an avalanche depolarising effect and results in a reduction in the transverse magnetisation components created after optical pumping. Accordingly, this limits the measurable precession time and thus degrades the accuracy and precision of the sensor. The spin-exchange collision cross-section, σ_{SE}, is two orders of magnitude more likely than that of σ_{SD} (2.2 x 10^{-18} m^2 compared to 2.03 x 10^{-20} m^2) [73]. The rate of spin-exchange collisions is denoted by γ_{SE} in the following equation:

$$\gamma_{SE} = q_{SE} \, \eta_{Cs} \, \sigma_{SE} \, \overline{\nu}. \tag{2.29}$$

Here, $q_{SE} = 7/32$ represents a spin-exchange broadening factor, a necessary inclusion for systems operating at finite magnetic fields. The rate at which spin-exchange collisions occur scales with increasing cell temperature. This is, however, a trade-off as the larger vapour density gives rise to a larger signal amplitude, therefore also boosting the sensitivity. During the experimental operation in this project, the vapour cells are primarily raised to elevated temperatures, meaning that spin-exchange is the dominant

31
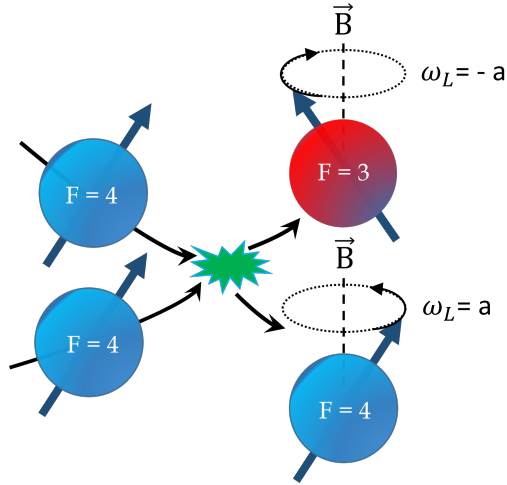
Figure 2.9: Spin exchange collisions can lead to atoms in mutual ground states decohering after colliding, result in an exchange of energy which causes one or both to change hyperfine level.

relaxation mechanism.

Eliminating the effect of spin-exchange collisions is the fundamental concept behind SERF OPMs. In finite field magnetometers, reducing spin-exchange is achievable through exploiting the light narrowing effect [74]. This approach aims to populate almost all atoms into the stretched state (see Section 2.4.4) of a single ground-state hyperfine level, thereby reducing the occurrence of spin-exchange collisions and thus narrowing the magnetic linewidth [75]. Collisions between atoms occupying the stretched state do not result in redistribution into the other ground-state sublevels. Achieving light-narrowed operation in the literature tends to be performed by pumping on the D_1 transition line, benefiting from the presence of a dark state in the $m_F = F = 4$ ground state. The process is augmented by employing an additional pump laser to evacuate atoms from the $F = 3$ level so that they redistribute into $F = 4$ [70].

In this work, however, intense D_2 line pumping effectively evacuates atoms from $F = 3$ and distributes a significant majority into $m_F = 4$. This is particularly effective at low vapour densities where γ_{SE} is inherently low. This is expanded on further in Chapter 5 where measurements using intense pump light in conjunction with linearly decreasing probe intensities across a range of buffer gas pressures facilitate a determination of γ_{10}.

The transverse relaxation rate γ_{20} includes all depolarising mechanisms inherent to the vapour cell, including those of spin-exchange,

$$\gamma_{20} = \gamma_{\text{SE}} + \gamma_{10}. \tag{2.30}$$

Therefore, this sets the total intrinsic depolarisation, caused by a combination of cell-wall collisions, Cs-N_2 collisions, spin-destruction collisions, and the contribution from spin-exchange collisions. Note that the described depolarising contributions do not account for operational or systematically induced effects. For instance, residual optical pumping from the probe light can occur, acting to depolarise the atomic spins from the coherently precessing ensemble, which will be discussed in Section 3.3.3. Additionally, other systematics, including magnetic gradients across the vapour cell, can play a role if present. Magnetic gradients cause atoms in different regions of the cell to precess at slightly different frequencies, accelerating the depolarisation of the overall atomic spin vector. In this work, magnetic gradients are found to contribute towards the overall atomic relaxation. The impact of gradients on the coherence time increases as a function of magnetic field strength. The lower limits on experimental magnetic gradients utilising different coil assemblies are presented in Chapters 4 and 6. Extracted intrinsic relaxation rates in this work are denoted as γ_{10} and γ_{20}, including when extrapolating to zero probe light power. When operationally induced spin-relaxation is incurred they are referred to as γ_1 and γ_2.

Chapter 3

Free-Induction-Decay Magnetometry

This chapter presents the principal mechanisms of the FID magnetometer system. An introduction to the technique along with the experimental setup predominately used for the work in this thesis is provided. Details on the employed optical pumping techniques are revealed, including a recently developed enhanced spin-polarisation technique. The distribution of atoms into specific ground states has a significant impact on the FID signals, including both the SNR and sensitivity. The detection scheme is also discussed, along with a description of the signal processing analysis used to calculate sensitivity. A characterisation of the sensor itself, including various noise contributions is also presented.

3.1   Experimental Configuration

A crucial element in any OPM scheme is the alkali vapour sensing element itself. This work has involved the use of several cells of various geometries and N_2 buffer gas pressures. Due to advancements in cell fabrication, the project progressed to a point where thicker cells became attainable. Consequently, the magnetometer performance was enhanced due to the increased optical path length resulting in a reduction of alkali-wall collisions. Additionally, the increased optical path length leads to an increase in

the optical rotation signal from the probe beam, culminating in greater SNRs and sensitivities. The cells have thicknesses of 1.5 mm, 3 mm, and 6 mm with pressures of around 50 to 240 Torr. The coherence time is ultimately constrained by each cells smallest dimension. The experimental configuration is designed to enable swift insertion of each cell without causing significant disruption.

The project experienced additional vital improvements, playing crucial roles in transitioning from a system with $pT/\sqrt{Hz}$ sensitivities to $fT/\sqrt{Hz}$ sensitivities. These significant steps and realisations made throughout the experimental work will be discussed in this chapter. Additionally, the data acquisition system was improved by D. Hunter, with an integrated GUI software connected to a picoscope (Model 5444D), enabling a smooth and efficient data capture process.

Figure 3.1 depicts the primary setup used, covering the majority of work in this thesis. The major advancement in the sensitivity performance was the improvement in SNR obtained through employing independent pump and probe lasers. This enabled optimal polarisation for both the pump and probe sequences. Furthermore, improvement was found from implementing an enhanced spin polarising technique discussed in detail in Chapter 4.

A MEMS Cs vapour cell serving as the magnetic sensing element is placed within a three-layer μ-metal shield, which suppresses the ambient magnetic field and magnetic noise contributions from external sources. Inside the shield, surrounding the cell are sets of Helmholtz coils (either 2 or 3 pairs) which provide the static magnetic field control and orientation along arbitrary directions. Two separate coil apparatus setups were used in this work. A 3-axis coil pair was employed for the 3 mm thick cells (as discussed in Chapter 6), while a 2-axis coil assembly proved more suitable for the 1.5 mm and 6 mm cells. The choice of coil assembly was influenced by practical considerations, and custom 3D printed mounts were designed to ensure the best alignment for each vapour cell under study. The FID scheme operates most effectively when orientating the static magnetic field transversely to the direction of beam propagation. The field was primarily applied along the z-axis. A low noise custom current supply source (3-axis), with a $\pm$ 75 mA range, described in [76] was used to drive the coils. Similarly, a battery

voltage source (12 V:Pro-Elec Lead Acid) connected in series with a resistor was also utilised, due to it imparting a very low level of magnetic noise. A suitable resistance can be incorporated to produce a variety of bias field strengths. Most commonly the system was set to produce a field magnitude of 50 µT. Unshielded real-world measurements do not require an injected bias field as the Earth's own magnetic field is often measured. However, emulating the magnitude of the field within a magnetic shield provides a benchmark for future FID OPM devices.
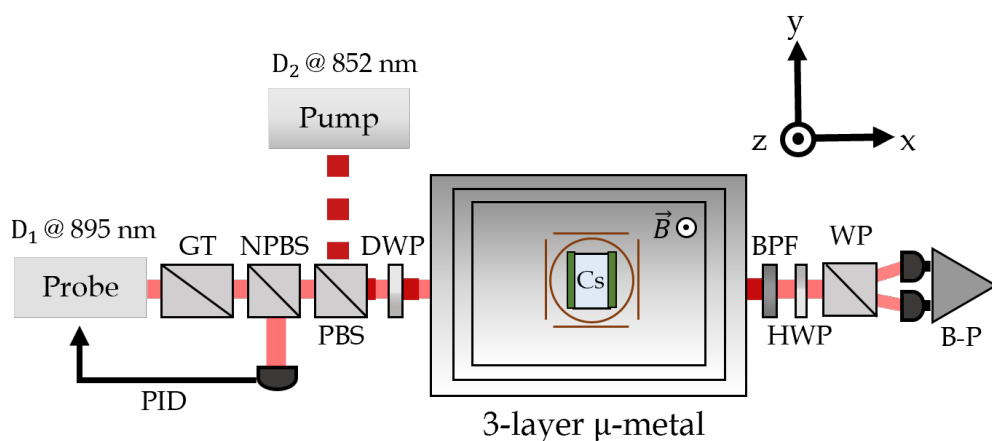
Figure 3.1: A dual laser system with independent pump and probe control is employed. The collinearly propagating beams overlap at the centre of the Cs vapour cell within a three-layer µ-metal shield. A set of Helmholtz coils is used to produce a bias magnetic field $\vec{B}$ along the z direction. A band-pass filter blocks the 852 nm pump light and allows the 895 nm probe light to be directed towards the polarimeter for detection. GT: Glan-Thompson polariser; NPBS:Non-polarising beam-splitter; PBS: Polarising beam-splitter; DWP: Dual-wavelength waveplate; BPF: Band-pass filter; WP: Wollaston prism; B-P: Balanced polarimeter

Raising the temperature of the cell is critical in raising the atomic vapour density to invoke greater light-atom interaction and therefore SNR. Counteracting the positive impact of raising the density is the increased decoherence rate which occurs at higher temperatures, therefore a balance between these is needed. Depending on the cell thickness, temperatures ranging from 60 °C to 88 °C provided optimal sensing conditions. Heating of the cell was carried out via a variety of methods. Avoiding introducing additional magnetic noise from the heating process is desirable. In this sense,

synchronising the heating to coincide with the optical pumping pulse before both being switched off during the probing stage proved the most effective method. Two printed circuit boards (PCBs) were placed in thermal contact to either side of the cell. The cell was resistively heated by applying a current to the PCBs. As described in [32, 55], the PCBs also serve as a route for enhanced optical pumping. Further details on this are provided in Chapter 4.

Two independent laser sources which collinearly propagate and overlap at the vapour cell are employed. This decouples the optical pumping and probing stages. Both are operated and controlled using separate acousto-optic modulators (AOMs). These are driven at 110 MHz using an RF signal generator (Marconi 2022) whose output is connected to separate frequency mixers and amplifiers. Customisable waveforms are supplied to each AOM using a single Keysight function generator (Model 33600A), together with a common DC voltage source. A volume holographic grating (VHG) diode laser (LD852-SEV600), packaged in a TO can, and tuned to the collisionally broadened F = 3 to F' transition (852 nm) is used to pump the atoms and create a high net spin-polarisation. An intense pulse of light between 0.8 - 1.7 W/cm^2 (60 - 130 mW peak power with a 3.1 mm beam diameter) creates a population imbalance such that atoms occupy the stretched m$_F$ = F = 4 state.

An optical isolator (not shown in Fig. 3.1) is placed immediately after the lasers output to prevent unwanted feedback from reflections back to the laser diode. The pump laser power is adjusted via a combination of waveplates and polarising beam splitters (PBSs). A fraction of the light is directed towards a wave-meter (MOGLABS) for monitoring and control of the laser frequency. The wave-meter provides a PID functionality that ensures the frequency is kept on resonance to within ± 100 MHz of the collisionally broadened spectra. The AOM is used to switch on and off the pump light. During the stage when it is on, the beam follows its aligned path along the first diffracted order towards an optical fibre (Oz Optics), with a typical diffraction efficiency > 80 %, along with a fibre coupling efficiency of 70 %. During the period when the pump is off, the beam remains undeviated in the zeroth order where it is deposited into a beam dump, with an extinction ratio of > 20000:1 measured after the fibre.

A distributed Bragg reflector (DBR) laser (model DBR895PN), typically detuned by several tens of GHz from the collisionally broadened F = 4 – F' transition (895 nm Cs line) is used for probing. Linearly polarised probe light imparts a lesser AC Stark shift compared to circular or elliptical light [77]. This shift introduces inaccuracies in the measured Larmor frequency, leading to erroneous readings of the magnetic field. Further elaboration on this is provided in Section 3.3.3. A separate AOM is used for the probe beam in a similar fashion to that of the pump. The diffracted probe light is also directed to a distinct optical fibre.

A linear polarisation of both laser beams is ensured through controlling a combination of polarising optics and waveplates. The fibre coupling approach is implemented for practicality reasons for future experiments. The fibre approach is also conducive for coupling both lasers into fibre splitters, enabling complete spatial overlap. This may be of benefit for a variety of experiments including for magnetic imaging (see Chapter 6). A Glan-Thompson polariser cleans the polarisation of the probe and converts polarisation noise into intensity noise. It is then separated via a 50:50 non-polarising beam splitter (NPBS) to direct light towards the experiment and to a monitor photodiode. An option of actively intensity stabilising the optical probe power delivered to the experiment, or switching the probe light on (when the pump light is off) or off (when the pump light is on) is facilitated through an analog PID controller (SRS SIM960). The data in this thesis relates to intensity stabilised probe light. As the AOMs are driven from the same RF and DC voltage source, there is a straightforward synchronisation between the pump and probe periods of the respective laser sources.

As seen in Fig. 3.1 the separate laser beams are directed towards a dual-wavelength waveplate (DWP) which is adjusted to ensure that the 852 nm pump light is circularly polarised, σ^+ and the 895 nm probe light is linearly polarised, π. The beams then pass through an aperture in the shield, overlapping at the cell. A band-pass filter reflects the pump light and allows the probe light to be directed towards the detection stage. A WP splits the probe light into two orthogonal states of light. This optical component has a far greater extinction ratio than other commonly employed polarisation optics such as PBS's. The separate polarisation states of light are directed to two separate PDs

via the use of a half-wave-plate (HWP) and WP combination. This is achieved using a balanced polarimeter where a differential measurement suppresses common mode noise (illustrated in Fig. 2.8), increasing the SNR and sensitivity. The polarimeter is connected to a data acquisition device which converts the analog optical rotation signal to a digital signal. The DAQ device and its noise performance is discussed further in Section 3.3.1.

3.1.1 Optical Pumping Techniques

In the course of this work, different spin-polarising techniques have been explored. Each incorporate amplitude modulation (AM) of the optical pumping light. These pumping schemes consist of either a single laser pulse, synchronous modulation administered at the Larmor frequency, or thirdly, a single laser pulse along with a polarising magnetic field pulse. These three respective pump modulation techniques are depicted in Fig. 3.2.
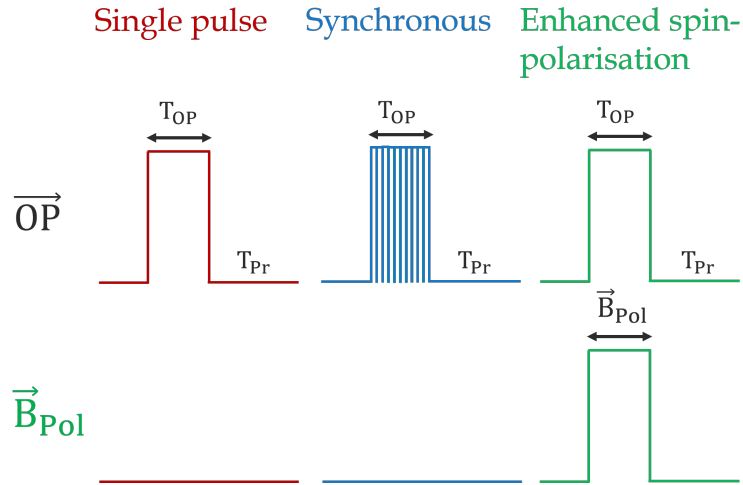
Figure 3.2: Optical pumping techniques used in this work. All are a form of AM. In each case the pump light is switched on to a high intensity before being switched off during the probing stage. An enhancement to the generated spin-polarisation can be to synchronously modulate the atoms at ω_L. Alternatively, a strong polarising magnetic field, $\vec{B}_{Pol}$, can be implemented which is discussed further in Chapter 4.

The commonality between these regimes is the utilisation of higher laser intensity during the pumping stage, carried out for a duration, T_{OP}, followed by the termination of the

pumping light which heralds the probing stage, T_{Pr}. In the synchronous regime, the Larmor precession is enhanced by modulating the pump light intensity at ω_L. Several pulses of light are employed to coincide with the precession frequency of the atoms as they traverse around the field. This serves as an effective way of building up and maintaining the spin-coherence in the sample. Other modes of modulation also exist, such as frequency modulation, described using a single laser beam setup in [26], and polarisation modulation. Neither of these methods have been pursued in this work due to the implementation of the independent laser system.

Conventionally, the appropriate choice between single pulse and synchronous AM is dependent on the magnitude of the operational bias field. The dynamic range of the sensor at the low end is inhibited by the number of detectable oscillations with which a reliable frequency can be extracted. For lower magnetic field strengths of up to a few µT, utilising a single light pulse can effectively polarise the atomic ensemble in preparation for the signal readout during the probing stage. However, at higher magnetic field strengths, the efficiency of single pulse optical pumping decreases due to the depolarisation caused by the higher precession frequency around the transverse field. At these elevated field strengths (on the order of tens of µT and above), synchronously modulating the light intensity at ω_L is beneficial to the total atomic spin-polarisation, coherence time and sensitivity [51]. Synchronous modulation tends to perform poorly at lower magnetic fields as there is a limit on the total number of Larmor oscillations due to the lower precession frequency.

During this work the newly implemented technique of introducing a strong polarising field was developed. This was found to be of particular benefit at higher field strengths, although it yielded excellent results regardless of the operational bias strength, across the OPMs conventional dynamic range (i.e. $0.5 \leq |\vec{B}| \leq 100$ µT). Nonetheless, the technique culminated in improved spin-polarisation, sensitivity, dynamic range and accuracy, which will be extensively discussed in Chapter 4. The optical pumping duration also impacts the spin-polarisation and sensitivity. Throughout the work presented in this thesis, the time allocated for T_{OP} was typically chosen to reach signal amplitude saturation, rendering any additional time allocation unnecessary.

3.2 Signal Processing

This section provides context on the modelling and processing of the FID signals. This will include the analysis of FID signal trains. Signal trains contain numerous FID pump-probe cycles set by the driving frequency or repetition rate of the sensor, denoted as $f_d = 1/T$, where T is the total pump-probe duration. A detailed presentation of the signal analysis and fitting procedure is presented in [51], with the same approach used in this work.

3.2.1 Fitting Analysis

The optical rotation described in Section 2.4.5 is directly related to the spin-polarisation, which can be represented as a magnetisation vector $\dot{\vec{M}}$. The dynamical evolution of this magnetisation, $\dot{\vec{M}}$, is emulated in a macroscopic sense through the semi-classical Bloch equations [78]. Equation 3.1 describes this magnetisation precession

$$\dot{\vec{M}} = \gamma \vec{M} \times \vec{B} - \gamma_2 \vec{M}, \tag{3.1}$$

with γ_2 the total spin-polarisation relaxation rate which covers all decohering processes that result in the atoms returning to thermal equilibrium. This vectorial model portrays the atomic orientation (polarisation moment of rank one) in the sample generated with circularly polarised light [79]. A model encompassing both ground states with all 16 Zeeman sublevels found through the density matrix formalism is required to fully capture the system dynamics [80]. However, this is computationally intensive and has not been pursued in this work. Instead, the FID signal stemming from the optical rotation of the probe is designated by the following nonlinear equation, modelling a damped sinusoidal function and providing a more intuitive representation:

$$M_x(t) = M_0 \sin(\omega_L t + \phi_0) e^{-\gamma_2 t}. \tag{3.2}$$

M_0 relates to the total spin-polarisation created during the optical pumping stage, ω_L is the Larmor precession frequency, and ϕ_0 is the initial phase. The inherent characteristic

of FID dictates that the overall spin-polarisation decreases as a function of time, at the rate given by the total relaxation rate, γ_2. Measurements of the relaxation rate will be presented in Chapter 5.

After digital conversion of the FID evolution by the DAQ device operating at a sample rate f_s, the following model is used to fit to and extract the aforementioned FID parameters.

$$S_n = A \sin\left(\omega_L \, n \, \Delta t + \phi_0\right) e^{-\gamma_2 \, n \, \Delta t} + \epsilon_n. \tag{3.3}$$

Here, A, is the FID signal amplitude, relating to the spin-polarisation generated during the optical pumping phase. Δ_t is the time interval between adjacent data points and n relates to the sample data point under consideration. ϵ_n relates to the noise present in the signal. DAQ devices convert the analogue FID signal to a digitised (discretised) sample. The DAQ device samples at a rate of $f_s = 125$ MHz and functions with 15 bit voltage resolution. The sample rate far exceeds the signals of interest oscillating at 175 kHz. Therefore, over-sampling is performed which averages N successive data points (typically 25 and 50) resulting in an ultimate sample rate of $f_s = 1/\Delta_t = 2.5$ or 5 MHz. This act also artificially increases the bit resolution from 15 to either 17.32 (2.5 MHz) or 17.82 (5 MHz) according to the equation from [81],

$$f_{os} = 4^w . f_s, \tag{3.4}$$

where f_{os} is the oversampling frequency, w is the number of additional bits and f_s is the sampling frequency.

3.2.2 Sensitivity Assessment

A magnetometer is often characterised by its sensitivity which describes either the smallest magnetic field detectable, or the smallest magnetic field fluctuation detectable [53]. As described in [51], the most sensitive method of frequency extraction involves the use of a nonlinear fit using Eq. 3.3. The proficiency of the fit is judged from calculating the reduced chi-squared statistic calculated using the Levenberg-Marquardt

(LM) algorithm [82]. Successive FID iterations, with the duration of each cycle set by f_d, are amassed to generate a time series of magnetic field data by extracting ω_L from each individual trace. This series conveys the magnetic field fluctuations from which the sensitivity is determined. This is performed through a Discrete Fourier Transform (DFT) which presents the data in the frequency domain, and considers the bandwidth of the measurement, which, set by the Nyquist limit is limited to half the driving frequency, $f_d/2$ [83]. Viewing the data in the frequency domain in the form of a root spectral density (RSD: the square root of a power spectral density) permits sources of magnetic noise to be conveyed and the noise floor of the sensor to be estimated. An example of this overall process is presented in Fig. 3.3.

Welch's method is utilised to average N consecutive 1 s signal trains, improving the uncertainty [84]. A Hanning window is also implemented which improves the estimation on the noise floor. All experimental sensitivities in this thesis are calculated using a minimum of a 1 s time series of FID data which is processed via this method. The fitting strategy impacts the frequency response of the sensor, which can be accounted for. Similarly, the response of the OPM is impacted by the relevant FID signal parameters such as the signal amplitude, A, and the T_2 time. Slightly lower peak amplitudes are detected for signals oscillating at frequencies approaching the Nyquist limit of the sensor. The frequency response of the sensor can be assessed by applying a known AC magnetic field over a range of detectable frequencies and extracting the amplitude value. A characterisation of a 3 mm thick vapour cell containing 220 Torr of N_2 in this respect at a bias field of $\vec{B_0} \approx 50$ µT was undertaken to showcase this response.
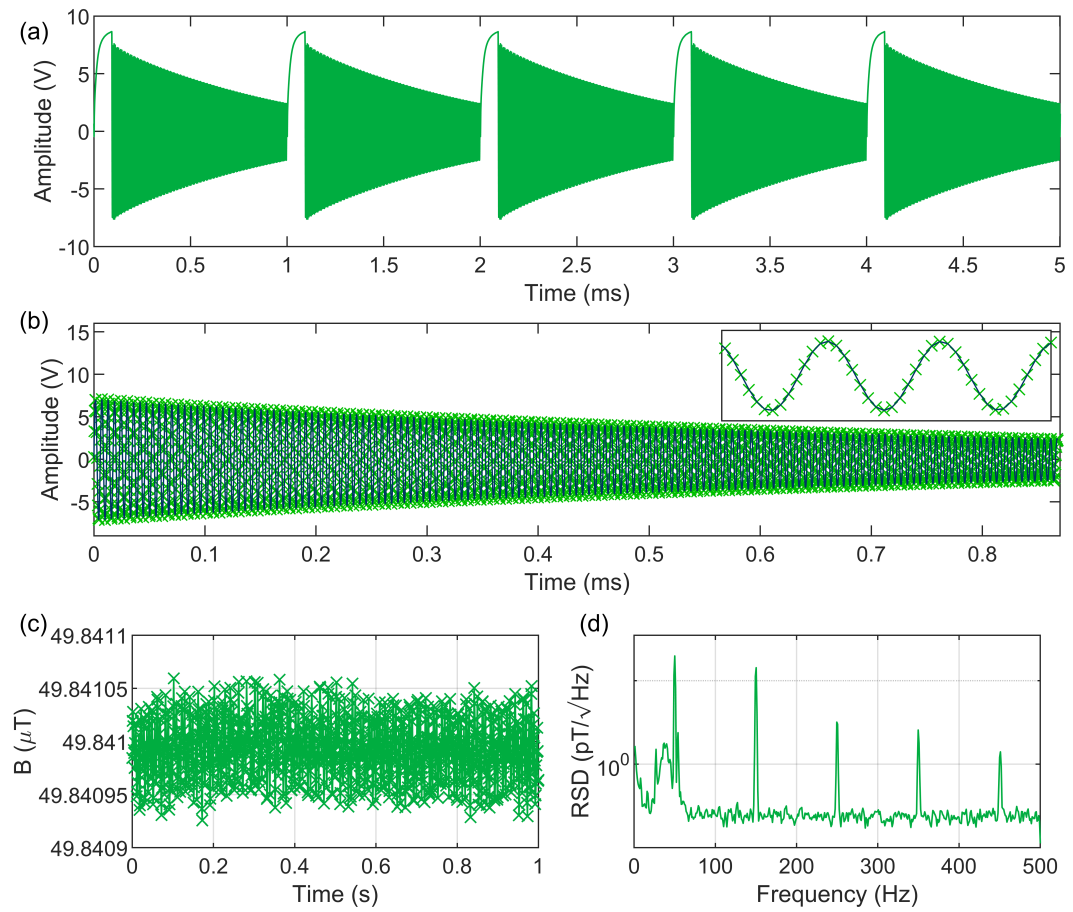
Figure 3.3: (a) Pump and probe sequences of the first 5 FID cycles from a 1 s FID signal train driven at $f_d = 1$ kHz. (b) Single FID probe cycle. Data points (green) with the associated fit displayed in black. Inset displays the first three oscillations. (c) Magnetic field time series data collected from extracting ω_L from each probe cycle over the full signal train. (d) Magnetic sensitivity performance after computing a DFT to multiple 1 s signal trains using Welch's method. The bandwidth is limited to $f_d/2$.

44
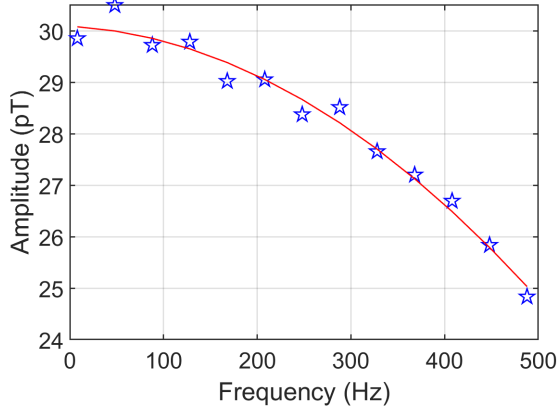
Figure 3.4: Data points (blue) relate to extracted peak amplitude values for a 3 mm thick cell operating in a bias field of $\vec{B_0} \approx 50$ µT along with a fit to guide the eye (red). Test signals oscillating at various frequencies are used to characterise the frequency response of the OPM. This enables a corrective scaling to be performed when assessing the sensitivity performance, which is presented in Fig. 3.5.

Figure 3.4 displays the data relating to a range of test signals passed through a Helmholtz coil pair comprised of a single turn. Each test signal consisted of a peak voltage of V = 20 V in series with a 10 MΩ resistor. The peak amplitude was software demodulated following the method described in [85]. An approximate 17 % decrease in the measured amplitude at the maximum detectable frequency is observed. Therefore, the true sensitivity of the OPM in this configuration should be scaled according to this roll-off.

Figure 3.5 showcases an example of a computed RSD for three different cell thicknesses. In the case of the 1.5 mm cell, only 1 s of data was collected (at f_d = 1 kHz), resulting in a large standard deviation and, therefore, large error estimation of the sensor's noise level. In contrast, for both the 3 mm and 6 mm cells, 40 independent 1 s datasets were respectively captured (at f_d = 1 kHz and 500 Hz respectively), significantly improving the sensor's noise level estimation. The uncertainty in the noise floor is determined from the standard deviation across a chosen frequency range. For the three respective datasets, it is calculated in the regions excluding technical noise peaks, yielding sensitivities and associated uncertainties of 2.8 ± 1.8 pT $/\sqrt{\text{Hz}}$, 0.26 ± 0.03 pT $/\sqrt{\text{Hz}}$ and 0.14 ± 0.01 pT $/\sqrt{\text{Hz}}$. The 3 mm cell has also been scaled according to

the frequency response calculated from the data in Fig. 3.4. For the remaining data in this thesis this frequency scaling has not been performed.
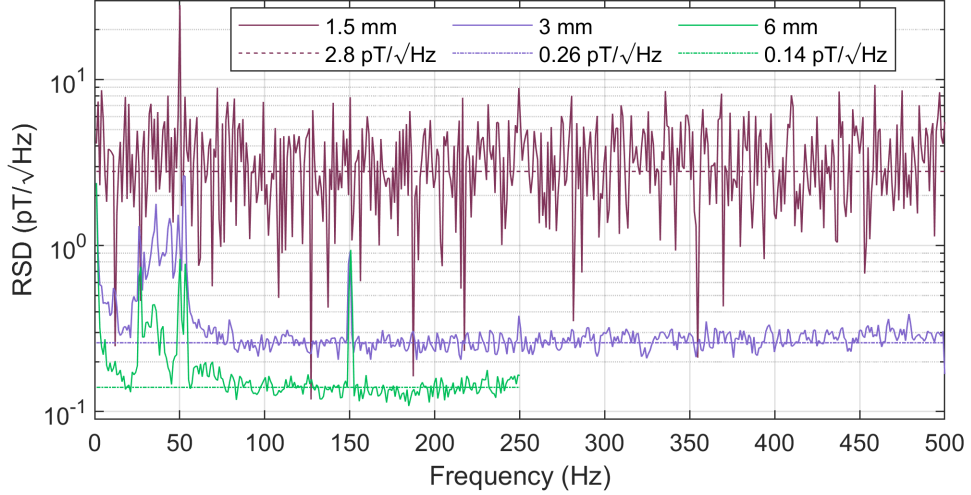
Figure 3.5: Sensitivity spectra captured using different cell geometries. The sensitivity increases as a function of cell thickness. Data capture advancements enabled more in-depth data collection. Capturing multiple 1 s data-sets lead to an improvement in the estimation of the noise floor as the 3 mm and 6 mm datasets display. The dataset for the 3 mm cell has also been scaled to account for the slight roll-off experienced by the OPM. The reduced line noise (50 Hz and harmonics) compared to Fig. 3.3 (c) is due to using a 12 V battery current driver, providing lower magnetic noise.

Other approaches, such as applying a DFT to the full signal train exhibits diminished usefulness, as the spin-coherence times of the MEMS cells (order of 1 ms) sets a limit on the frequency resolution. This results in the spectrum containing multiple peaks spaced at f_d.

3.2.3   Cramer-Rao Lower Bound (CRLB)

Another way of assessing the ultimate precision of the magnetic performance is through calculation of the Cramer-Rao Lower Bound (CRLB) [86, 87]. The CRLB sets the statistical lower limit on the uncertainty of establishing an unbiased estimator from a signal of interest. This relates to extracting the frequency parameter, f, from a single exponentially decaying FID trace, valid when the signal is embedded in white Gaussian noise. This uncertainty in Hz of f, denoted by σ_f in Hz is described by:

$$\sigma_f \geq \frac{\sqrt{12C}}{2\pi(A/\rho_A)T_m^{3/2}}. \tag{3.5}$$

A represents the signal amplitude (V_{RMS}), and ρ_A is the noise spectral density ($V_{RMS}/\sqrt{Hz}$). Thus, the term in parenthesis symbolises the SNR. T_m relates to the measurement duration (probe duration). A correction factor, C, is a necessary inclusion for any signal undergoing a damping effect. This correction factor is presented in Eq. 3.6,

$$C = \frac{N^3}{12} \frac{(1-z^2)^3(1-z^{2N})}{z^2(1-z^{2N})^2 - N^2 z^{2N}(1-z^2)^2}, \tag{3.6}$$

where N relates to the number of data points in the signal and with $z = e^{-\gamma_2/NT_m}$. For other magnetometry schemes that maintain continuous pumping and probing, and with the sensor not limited by spin-relaxation processes (i.e no damping), this correction factor approaches C = 1 [88]. Typical values in this work range from C = 3 ($\gamma_2 = 0.6$ kHz) to C = 10 ($\gamma_2 = 1.25$ kHz).

A simple conversion to uncertainty in magnetic field arises through $\sigma_B = 2\pi f/\gamma$, providing:

$$\sigma_B \geq \frac{\sqrt{12C}}{\gamma(A/\rho_A)T_m^{3/2}}. \tag{3.7}$$

Equation 3.7 in conjunction with Eq. 3.6 demonstrates that minimising σ_B, i.e. attaining a higher sensitivity is inversely related to γ_2 and proportional to both measurement time and SNR. To include the bandwidth of the measurement, which is an important factor in magnetic field sensing, the statistical uncertainty σ_B can be adapted into a noise density ρ_B through the following relation

$$\rho_B = \sigma_B \sqrt{f_d/2}. \tag{3.8}$$

Calculating the magnetic noise density ρ_B also supposes that the magnetometer is limited by white Gaussian noise, such that there is a flat noise density across all frequencies in the bandwidth range. All OPM systems, however, suffer from 1/f technical noise and often line noise. Therefore, a flat noise density is evident in all areas except for

these regions.

Inserting the extracted experimental parameters from an optimised FID signal into Eqs. 3.7 and 3.8 yields an indication of the overall sensitivity of the OPM. Figure 3.6 provides an overview of the sensitivity expectation calculated from the CRLB condition for parameters matching those throughout this work.
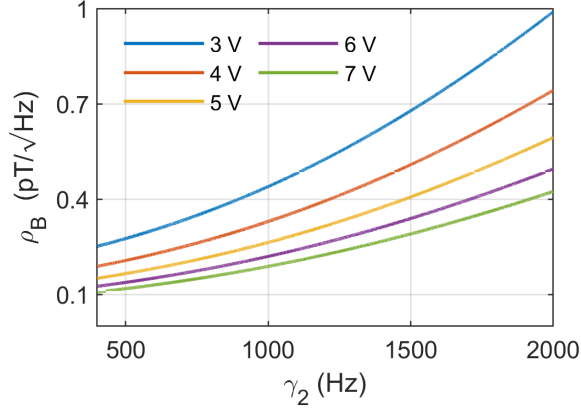
Figure 3.6: Simulated CRLB sensitivity calculated using Eq. 3.8 using parameters resembling those found in this work. Higher SNRs and T_2 times improve the sensitivity. The noise level and measurement duration are assumed to be constant.

As the data in this thesis will demonstrate, the calculated CRLBs match the experimental noise floors. The strategy most commonly implemented was the capture of a signal train of FID data, which provides numerous independent FID cycles (typically either 500 or 1000 depending on f_d). The overall statistical uncertainty in each of the extracted parameters from Eq. 3.3 is therefore low. The primary source of uncertainty in the determination of σ_B stems from the uncertainty in the level of noise (ρ_A) present. Determining this noise level is discussed further in the next section and in Chapter 4.

3.3 System Characterisation

The ensuing section presents a characterisation of the OPM system. This includes detailing the optical noise regime and identifying sources of magnetic noise.

3.3.1 Optical and Detector Noise

The sensitivity of OPM systems are fundamentally limited by either photon-shot noise or spin-projection noise [14, 89]. In the FID configuration the sensitivity limit is set by the former, as a negligible contribution to the noise floor stems from the much lower spin-projection noise. The photon shot noise density, with units $V/\sqrt{Hz}$ can be calculated using:

$$\rho_{\text{SN}} = G\sqrt{2ePR},\tag{3.9}$$

where, G, is the trans-impedance gain of the amplifier, e is the electron charge, P, is the incident optical power and R is the responsivity of the detector. The detector used primarily in this work is a Thorlabs balanced polarimeter (Model PDB210A) exhibiting $G = 5 \times 10^5$ V/A and R = 0.6 A/W.

The nature of OPMs is such that a probe beam is required to measure the Larmor precession. The act of measuring therefore imparts noise in the system. Heightened optical intensities will increase the current generated by the photodiode, ultimately raising the level of noise in the detection system. However, depending on the status of experimental operation and the light level i.e. the number of photons used, the sensor may be operating in a regime limited by technical noise. Technical noise can arise as a result of laser intensity fluctuations, whether from the laser source directly or from mechanical issues such as unstable optics. Equation 3.10 presents the additive sources of noise in the system following the convention from [90], giving the total noise power N_p:

$$N_P = \alpha P^0 + \beta P^1 + \epsilon P^2,\tag{3.10}$$

where, P, represents the average incident optical power. The total noise in the system scales according to this equation, where, α relates to the electronic or detector noise, β, represents the photon-shot noise, and ϵ symbolises the technical noise contribution. The system is considered shot-noise limited when $\beta P^1 > \epsilon P^2$ and $\beta P^1 > \alpha P^0$, i.e. where

there is a linear dependence.
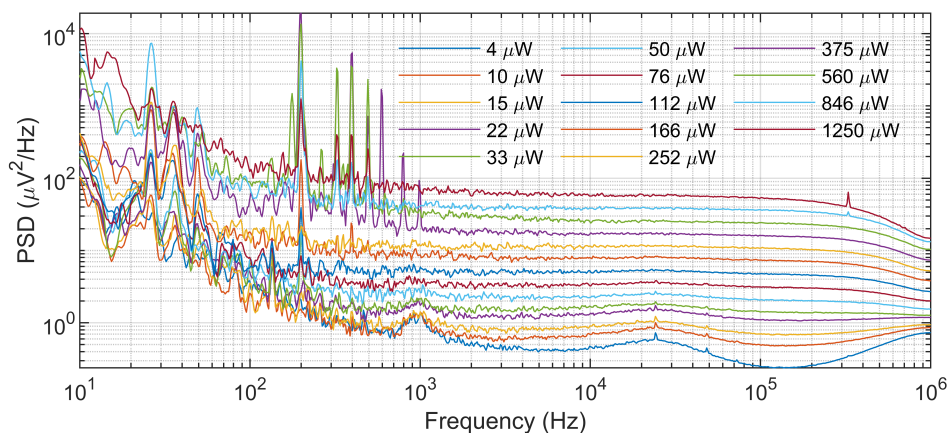
Figure 3.7: Power spectral density (PSD) displaying the optical noise level as a function of frequency. A variety of probe powers were measured, which impinge on the detector after being transmitted through a room temperature MEMS vapour cell.

To clarify that this OPM system operated within the photon-shot-noise limited regime, an analysis of the noise in the probing and detection facets as a function of light intensity was conducted. This was performed in the absence of optical pumping light and without applying any external magnetic field. The vapour cell was kept at room temperature in order to exhibit a low atomic vapour density, and the probe beam was set far detuned from optical resonance. This enables the base level of noise in the system to be determined, without any additive noise due to atom-light or atom-field interactions which can amplify the noise. The bandwidth of the detector is 1 MHz.

Figure 3.7 displays the PSD for the various probe powers employed. This enables an estimation of the optical and detector noise as a function of frequency to be determined. Higher noise levels are obtained with increasing probe powers (photons incident). The appropriate noise level relating to ρ_A can be inserted into Eq. 3.7 to calculate an expectation of the sensitivity of the sensor.

Most commonly, the OPM was set to operate at a Larmor frequency of 175 kHz, which exhibits a slightly lower noise level than lower frequencies. Around this value, the optical noise level remains relatively consistent. Calculation of the noise levels of the respective probe powers over a specified frequency range of interest (170 to 180 kHz) is

50

then performed to assess the dominant noise source according to Eq. 3.10. The result of this is displayed in Fig. 3.8.
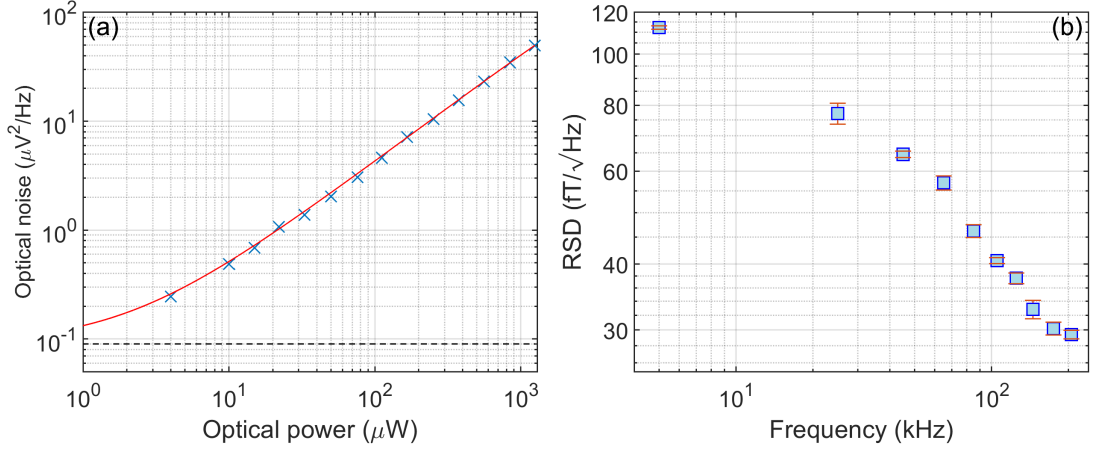
Figure 3.8: (a) Data points relate to the mean of the noise level between 170 - 180 kHz from Fig. 3.7. The black dashed line indicates the detector noise. The red line is the fit using Eq. 3.10. A linear dependence is found between $\approx$ 30 µW to 1 mW verifying shot-noise is the dominant noise source. (b) Noise level measured directly from the DAQ with statistical error bars. The overall measured noise is lower as the frequency of a AC signal increases, leading to $\approx$ 30 fT/$\sqrt{\text{Hz}}$ at Earth's field strength where f = 175 kHz.

The overall linear dependence validates that the sensor is shot-noise limited for optical powers between 30 µW and 1000 µW. Below the former, the number of photons detected is low, therefore, the noise from the detector is the main contributor. Above 1000 µW, a second order effect is found, confirming that technical noise starts to become relevant. Probe powers were selected to ensure that the total incident light on the detector remained within the shot noise-limited range, ensuring optimal performance.

Quantifying the level of noise from the DAQ device itself was also carried out. This was performed by passing AC signals from a function generator (Keysight) between a frequency range of 5 - 200 kHz. The amplitude of the signals were 20 V_{pp}, equivalent to the typical FID amplitude and data capture range of $\pm$ 10 V. Several independent 1 s time domain datasets were captured using the DAQ device which was subsequently converted to a RSD. The results of these are displayed in Fig. 3.8 (b). The noise level determined via this method demonstrates a reduction in noise as a function of increased

frequency. This actually coincides well with demonstrating high sensitivities at Earth's field strength. At a frequency of 175 kHz the overall DAQ noise contribution is around $30\,\text{fT}/\sqrt{\text{Hz}}$, compared to a contribution closer to $100\,\text{fT}/\sqrt{\text{Hz}}$ when operating at lower frequencies. This is directly related to a lower value of the noise density, ρ_B, leading to an improvement in sensitivity at higher field strengths (for signals with identical parameters according to Eq. 3.7). The level of DAQ noise adds in quadrature to the noise level set by the CRLB.

An alternative calculation of the noise in the system is to consider all sources of noise present when operating the magnetometer optimally. Noise contributions from independent sources can be found following the method presented in [32]. Noise spectra are obtained via computing RSD datasets following the same approach described in Section 3.2.2. Successive DFTs applied to numerous non-overlapping FID traces are performed in order to get a true reflection of the noise present when the magnetometer is fully running and performing optimally for sensitivity. This includes the presence of the applied magnetic field, and the pump and probe light. The computed RSD then provides an indication of the total noise in the system through calculating the average noise density across a specified range, centered at the Larmor frequency. This noise level fully encompasses the true properties of the sensor when performing as a magnetometer, hence, would seem the best means of characterising noise. This will be elaborated on further in Chapter 4. This noise estimation approach provides values which result in CRLB estimates that closely align with the experimental sensitivities.

3.3.2 Magnetic Noise

Imparting magnetic noise results in the overall noise floor being raised, which reduces the magnetic field measurement precision. For example, the driving source used to provide current to the Helmholtz coils and generate the bias field, $\vec{\text{B}}$, can contribute substantial magnetic noise. Figure 3.9 (a) demonstrates a noise floor comparison for the OPM, arising from differing current sources. The highest sensitivities can only be reached using experimental apparatus that does not inject major noise into the system.
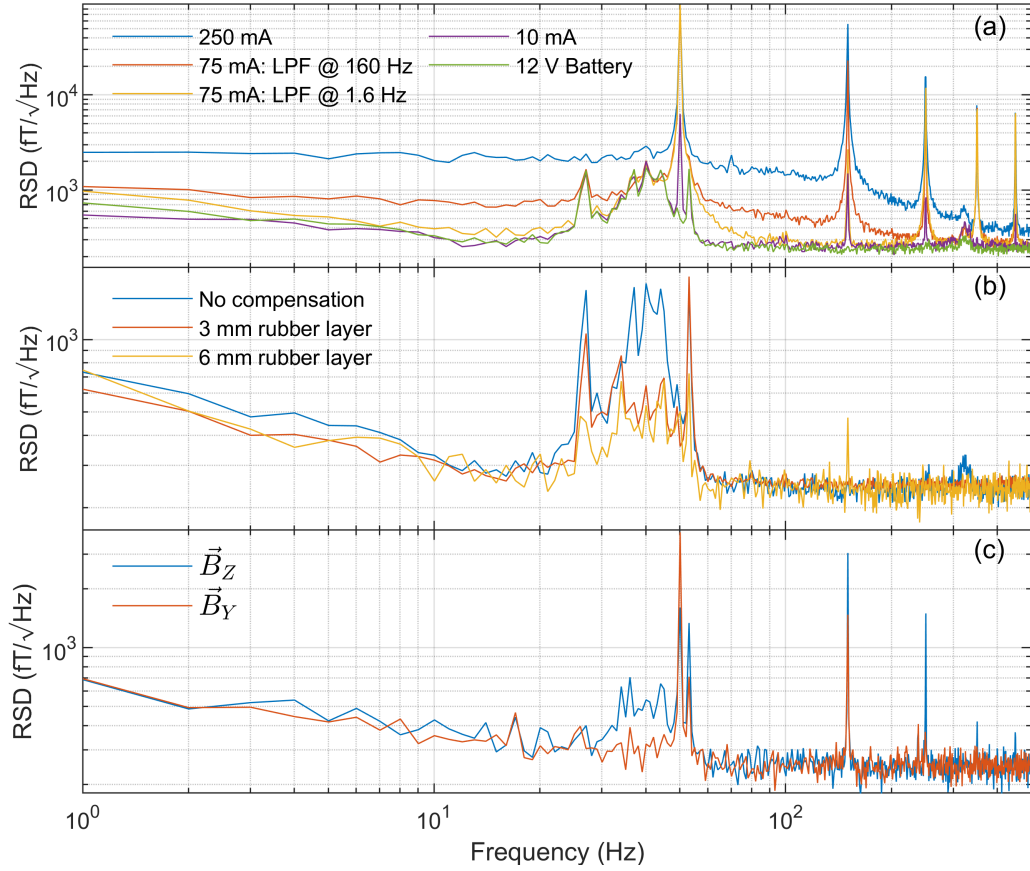
Figure 3.9: (a) Measured noise floor from various coil driver current sources. The lowest noise was found using either a 10 mA driver or a 12 V battery source. (b) Magnetic noise originating from an air-conditioning (AC) power generator, oscillating in the 27 - 55 Hz band. and additional vibrational noise. Rubber layers were placed underneath the μ-metal shield to attempt to reduce the amplitude of noise in this band. (c) Magnetic noise reduction observed when applying the field along the y-axis, altering the directional Larmor precession.

Primarily, measurements that involved varying the bias field strength, such as those presented in Chapter 4 were conducted using the $\pm$ 75 mA driver containing a low-pass filter (LPF) at 1.6 Hz. This decision was primarily motivated by practicality reasons, as integrating a USB input for the coil driver with GUI software allowed for comprehensive control over the bias field. Additionally, this provided much lower noise compared to other sources, such as the 250 mA and 75 mA (with a LPF with cutoff frequency at 160 Hz) drivers. The current sources producing the lowest noise in this thesis relate to the $\pm$ 10 mA driver and 12 V battery source. Despite the low-noise performance

of the former, the limited available current produced maximum bias fields of only a few µT, preventing its use for measurements at Earth's field strength. Therefore, the battery was predominately utilised when assessing the peak sensitivity performance of the OPM.

The location of the OPM setup is in close proximity to an air-conditioning (AC) generator. This supplies electric currents to the building, oscillating at $\approx$ 27 Hz, and subsequent harmonics. This magnetic noise is observable in the majority of sensitivity spectra included in this work, particularly in the 27 to 55 Hz band. This noise does vary in amplitude and also combines with vibrational noise present in this band in the OPM setup. This was observable when using a variety of cells, confirming that it was not simply an etaloning effect. Attempts to mitigate this level of noise are presented in (b). The amplitude of the vibrational noise was reduced by employing a rubber layer under the µ-metal shield, however, fully eliminating this was not possible. Therefore, the precision with which magnetic field changes are detectable in this band is lower than over the full extended bandwidth. This would limit the quality of the sensor for applications which require highly sensitive measurements within this band, such as the monitoring of neural activity [24]. The most sensitive type of OPM schemes tend to require multiple layers of magnetic shielding [72]. Typical SERF setups incorporate five layers of µ-metal shielding in conjunction with an inner ferrite layer [91]. This is required to reduce the ambient background field to within the sensors operational range between 1 and 200 nT. A primary advantage of total field OPMs is that they are designed to work at higher field strengths and as such have the dynamic range to do so. The three-layer µ-metal shield in this work proved to be sufficient for the work presented. However, the sensitivity across the full bandwidth would likely be improved with an upgraded magnetic shield.

The directional dependence of the magnetic noise is also illustrated in (c). Applying the bias field along the y axis mitigated a significant amount of noise in this band, verifying most of the magnetic noise from the AC generator in this band was along z. However, for reasons described in Chapter 6, a magnetic gradient across the cell was found when orientating the bias field along this direction. Therefore, the primary axis

producing the bias field used throughout this work is the z-axis, despite increased noise within the 27-55 Hz band.

3.3.3 Probe Frequency

A characterisation of the probe frequency is presented in this section. A 3 mm thick cell containing 220 Torr of N_2 was heated and maintained at a cell temperature of 80 °C. A consistent peak pump power of 120 mW operating at a 10% duty cycle strongly polarises the ensemble. The repetition rate was set to 1 kHz with 1 second of data captured during each measurement. Probe powers between 200 to 800 µW were employed with intensity stabilised via the AOM. The frequency of the probe is varied through adjusting the TEC (Thermo-electric cooler) output of the laser driver which displays a frequency coefficient of around 25 GHz/°C. The results are presented in Fig. 3.10.

The impact of the probe frequency is clear as it is swept from initially being red-detuned, through the F = 4 to F' and F = 3 to F' resonances, to being blue-detuned. (a) depicts an absorption measurement conducted through tracking the data from the two independent channels of the polarimeter. Summing the DC values of these provides a relative absorption measurement across the frequency range. This effectively maps out the optical spectrum of the MEMS cell. As expected, an offset is evident from the different probe powers. The oscillations either side of the F = 4 and F = 3 are a result of etaloning, with this imprint also evident from the variation in the perceived Larmor frequencies, displayed in (c). The period of oscillation can be converted to obtain the free spectral range (FSR), defined as $\Delta\nu = c/2L$. From the data $\Delta\nu \approx 38$ GHz providing L = 3.7 mm, in reasonable agreement to the 3 mm length of the cell plus 0.5 mm glass thickness either side of the cell.
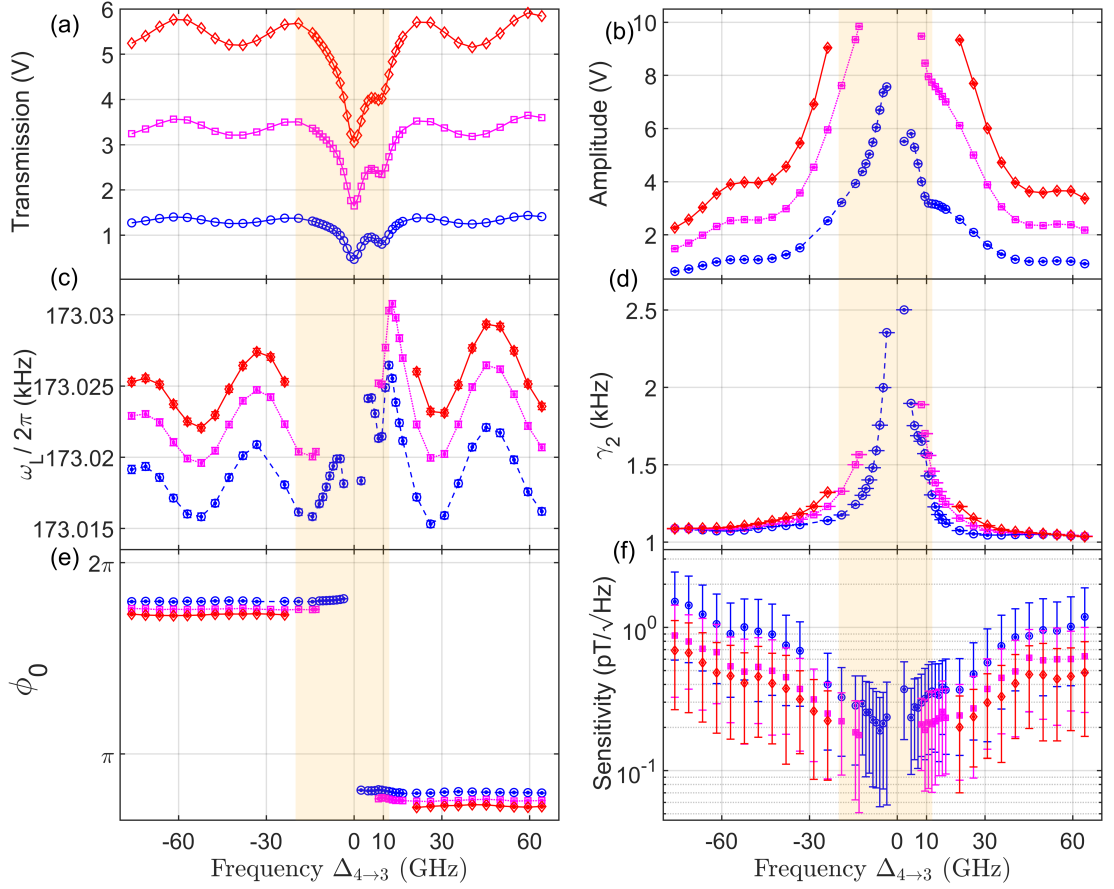
Figure 3.10: Probe frequency scan with the optical spectra (a) and (b-e) FID signal parameters from Eq. 3.3 displayed for probe powers of 200 µW (blue), 500 µW (magenta), and 800 µW (red). Data relates to a 3 mm thick cell heated to 80 °C. (f) Sensitivity performance calculated over 1 s. (a) provides the DC measured absorption (addition of both signals from the independent polarimeter channels), providing a frequency reference for the remaining data sets. The orange shaded region indicates the approximate zone where significant power broadening caused by the probe occurs. In this region, the probe acts to depopulate any polarised atoms, leading to errors in the FID fits, elevated relaxation rates, and increased AC stark shifts.

An offset in the extracted ω_L as a function of increased probe power is due to the heightened light shifts. A discrepancy between maximum and minimum values in the data set of 16 Hz (0.009 % of the mean) is present across this range. The action of the probe light inherently induces a light shift systematic. Nonetheless, reducing the light atom interaction by decreasing the optical power or operating far from resonance can decrease this effect. However, this comes at a possible cost of reduced SNR and

sensitivity.

Fig. 3.10 (b) presents the signal amplitude data which also increases as a function of probe power and increases closer to resonance. Due to the polarimeter's detection range limit being exceeded, several data points have been omitted. This is a consequence of operating where significant power broadening occurs, which also raises the γ_2 rate as displayed in (d). All corresponding data points in the other plots are therefore also omitted. (e) depicts the π phase flip that the probe experiences as it is swept over the two-peak optical resonance. The transition is characterised by a distinctive step change rather than a gradual shift. All of the data in (a) to (e) contain a low error from the standard deviation due to the numerous (1000) FID signals captured. (f) presents the sensitivity data along with a much larger error due to only 1 s of data collection. The sensitivity improves as a function of increased light-atom interaction, the result of improved SNRs. However, the FID sensors accuracy degrades when probing close to resonance due to an effective optical pumping action caused by the probe. The signals can exhibit an initially similar shape to those which are presented in Section 4.4. However, in the case here, a resonant probe serves only to expedite the relaxation rate and corrupt the accuracy of the measurement.

The data showcases that using this two-laser system enables a wide frequency range in which the probe induces substantial light-atom interaction, leading to a large range where high sensitivities can be achieved. The probe beam is typically tens of GHz detuned (blue or red) from the collisionally broadened resonance to avoid excessive power broadening and light shift systematics. The workhorse of this system is the intensive pump laser which sets the atomic state preparation. The three main remaining factors utilised to reach maximum sensitivities are the atomic vapour density, the probe power and the probe frequency. These parameters are optimised in order to boost the signal parameters according to Eq. 3.7. Data relating to the impact of cell temperature is provided in Section 5.3. The impact that pump power has is presented in Section 3.4.2.

3.4 Accurately Measuring a Relaxation Rate

This section describes the process and characterisation of accurately determining a relaxation rate. This demonstrates the impact of measurement time, the optical pumping parameters, and the filtering process on the reliability of extracting accurate data from the FID signals. These descriptions are pertinent to studies carried out and presented in Chapter 5, specifically in Section 5.2 which involved extracting γ_{10} rates from 6 mm thick cells at temperatures of 30 °C.

3.4.1 Measuring Beyond T$_2$

The FID modality provides a highly suitable platform for signal measurement, primarily owing to the observance within the temporal domain. This presents a particularly effective way of extracting a spin-relaxation rate. The relaxation time, T_2, is defined as the time taken for the signal to reach 1/e of its initial amplitude value. The general fitting process used to extract signal parameters, including the relaxation rate has been described in Section 3.2.1.

To ensure an accurate measurement of this spin-relaxation rate, it is self-explanatory that an adequate measurement period extending beyond the 1/e point is required. Reducing the repetition rate, f_d, of the pump-probe cycle allows the atoms to fully decohere before the next pumping cycle. This avoids a measurement induced error by circumventing memory effects in the atoms, i.e. the atoms should be at thermal equilibrium before each pump sequence to ensure they are not partially polarised or already weighted towards specific Zeeman states.

In conjunction with the reduced f_d is the increased duration between each pump-probe cycle, leading to an increased overall measurement time for each FID trace. This differs from the case when the sensor operates optimally for sensitivity, where f_d is set to repeat the pump-probe cycle before the signal fully decoheres (truncation). Consequently, an accurate value for the relaxation rate is only valid for a select portion of presented data in this thesis, which are denoted as γ_1 when spin-exchange collisions are fully suppressed, or γ_2 if spin-exchange collisions are present. Furthermore, when

the data is extrapolated to zero light power these are denoted as γ_{10} and γ_{20}.

The studies presented in Section 5.2 actively seek to extract the intrinsic longitudinal relaxation rate value γ_{10}. The data relating to these FID signals clearly show that the majority of employed probe powers yield relaxation rates below 200 Hz. This means that the coherence times extend beyond 5 ms ($1/\gamma = \tau$). This is evident from viewing an example extracted FID signal from the inset of Fig. 3.11.
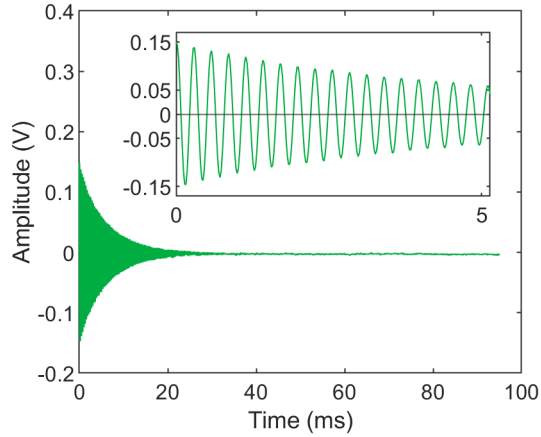
Figure 3.11: Raw signal data obtained at a probe power of around 540 µW for a cell containing 115 Torr of N_2, for which this data point is also included in Fig. 5.4. The signal has been allowed to fully re-thermalise. Prior to the FID fitting procedure, it is clear that the $1/e$ point extends beyond 5 ms.

Furthermore, data relating to the relaxation rate for the lowest probe power in Fig. 5.4 (a) provides a measured relaxation rate of around 145 Hz. This indicates that a measurement (probing) duration, denoted as T_{Pr}, well beyond 7 ms is required to provide a sufficient duration of data capture in order to assess the actual relaxation rate. Expanding on this, the impact that T_{Pr} has on the extracted relaxation rate for a cell containing $\approx$ 160 Torr of N_2 is depicted in Fig. 3.12. (a) Displays the measured values for a range of measurement times. The duration of T_{Pr} is displayed with the corresponding marker types in (b). This solidifies the requirement of measuring beyond several relaxation periods for an accurate measurement. Increasing T_{Pr} causes a sharp reduction in the extracted relaxation rate until a T_{Pr} of approximately 50 ms. Beyond this duration, negligible difference in the relaxation rate is obtained.
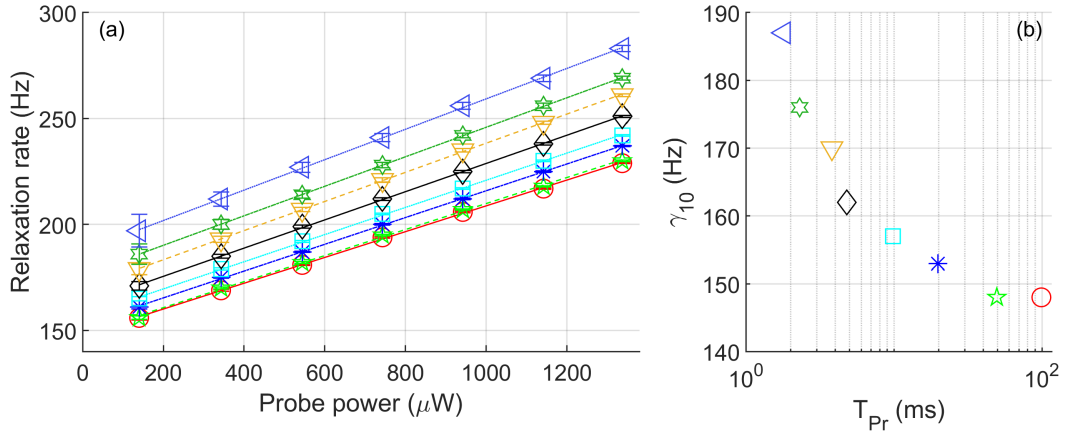
Figure 3.12: Relaxation rate determination as a function of T_{Pr}. (a) extracted relaxation rate data as a function of probe power obtained from the FID fitting procedure, along with a corresponding linear fit. The data was taken using a variety of repetition rates (thus a variety of measurement times). (b) measured intrinsic relaxation rate values which highlight the impact that measurement time has on this extraction. The corresponding marker types and colours from (a) relate to the extracted the values in (b) after extrapolating to zero light power.

3.4.2 Pump Duration and Power

An analysis of the impact of the optical pumping duration on the spin-polarisation and relaxation rate was also conducted. It was found from these results and other experimental analysis that employing a pump duration of at least 2 ms was sufficient to result in the same γ_{10} value. The high pump power of 120 mW also provided abundant optical power throughout the measurements. Measurements have been taken across a range of powers which display a negligible variation in signal amplitudes or relaxation rates when pumping exceeds around 50 mW for a cell at a higher vapour density of T = 70 °C. Therefore, any slight drift in the pump power e.g. from polarisation drift in the optical fibre, particularly at a lower vapour density of T = 30 °C would not present a discernible difference in the relaxation rate. The data from this is presented in Fig. 3.13.
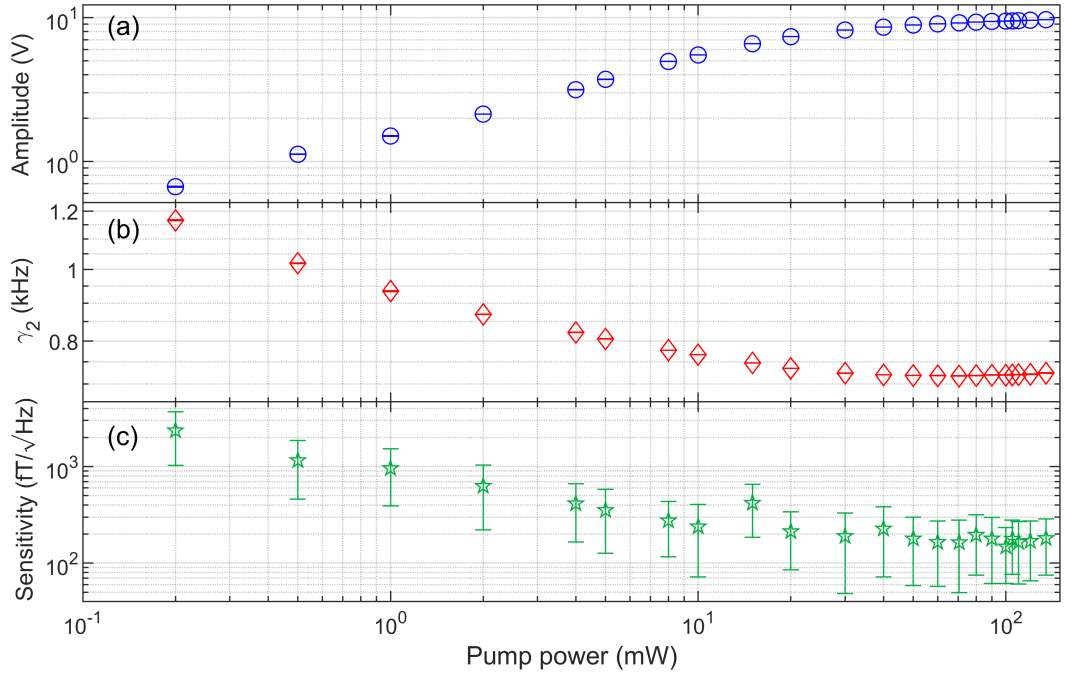
Figure 3.13: Pump power effect on (a) amplitude (b) γ_2 and (c) sensitivity for a temperature of T $\approx$ 70 °C and a bias field of $\vec{B} \approx$ 50 µT. Saturation occurs, particularly for the extraction of γ_2 at pump powers exceeding 50 mW. The measured sensitivity is also presented. The sensitivity is prone to fluctuations when only 1 dataset is used. A more consistent sensitivity method is to average multiple datasets.

Analysis of the duration of measurement time and optical pumping parameters in order to achieve a consistent γ_{10} value was critical for ensuring consistency across measurements. Based on the data acquired, an optical pumping duration of 5 ms, with a peak pump power of 120 mW, along with a probe duration of 95 ms were selected to achieve this. This corresponded to a total pump-probe cycle duration of 100 ms at a repetition rate of 10 Hz.

3.4.3 Digital Filtering

This section describes the digital filtering procedure applied to the FID data, also only pertaining to the measurements of γ_{10} in Section 5.2. Figure 3.14 (a) displays 1 s (a full FID signal train) of data involving a probe power of 1337 µW at a buffer gas pressure of 162 Torr. The signal train contains 10 individual FID cycles which are subsequently

fit to in order to obtain the relevant signal parameters (described in Section 3.2.1).
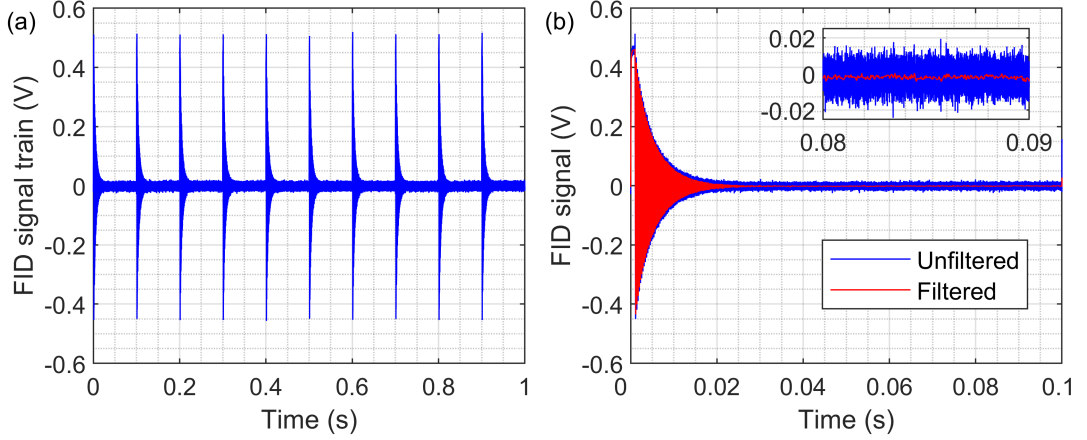
Figure 3.14: (a) Unfiltered (raw) FID data displaying consecutive FID traces over a measurement period of 1 s at $f_d = 10$ Hz. The pump and probe durations ensure that the spin-polarisation fully equilibriates after optical pumping. (b) Single FID cycle from (a) before and after filtering. The filtered data is used in this work to extract the relevant FID parameters when measuring γ_{10}. A low pass (cut-off) filter is applied post-process using a Butterworth filter with the data also down-sampled. This leads to an overall reduction in RMS noise as evident from the filtered data.

The DAQ was set to sample at a rate of 5 MHz. The oscillation frequency, f, at 1 µT ≈ 3.5 kHz, therefore, sampling at this rate results in a significantly high number of data points within each FID cycle. This can lead to improper fits of the data in determining the relevant fit parameters. Therefore, for each data-set analysed, a low pass Butterworth filter (2nd order) was applied to suppress any higher frequency noise potentially affecting the fit. Any higher frequency components in the signal are not relevant to the Larmor precession under study. Additionally, the data was down-sampled by a factor of 100, reducing the effective sample rate to $f_s = 50$ kHz. An example of this filtered data which aided in the fitting procedure is displayed in Fig. 3.14 (b). This also highlights the overall reduction in root-mean-square (RMS) noise, which is notably present in the unfiltered data beyond the $1/e^2$ point. After this filtering procedure, there still remained a sufficient number of data points within each Larmor precession cycle (≈ 14 points per cycle) to accurately determine the fit parameters. These post-processing techniques did not corrupt the overall extracted

values and served only to expedite the fitting analysis. This filtering procedure was not ordinarily applied when assessing the sensitivity performance of the various OPM configurations described in Chapters 4 and 6.

Chapter 4

Enhanced Spin Polarisation

This chapter discusses the detrimental effect that operating at higher magnetic fields has on both the signal amplitude and coherence time of the FID magnetometer. This is an effect commonly observed in total field magnetometer devices. A novel approach to mitigate this effect is presented, following the work by Hunter et. al. in [32]. This proved an effective method for enhancing the spin-polarisation and sensitivity, with encouraging prospects for future FID sensor integration outside the laboratory. Tuning of the optical pumping frequency is explored in the latter sections of the chapter. Results are presented where the atoms are either manipulated into a single ground-state hyperfine level, or evenly distributed between both, where the sensor can operate as a comagnetometer.

4.1   Magnetic Field Magnitude

Finite field magnetometers have an advantage over zero-field (SERF) sensors in that they are inherently capable of operating over a wide range of field strengths. Exhibiting a significantly higher dynamic range, they have the ability to effectively measure magnetic fields in both shielded and unshielded environments. However, despite this, increased bias field magnitudes lead to increased γ_2 rates, which is detrimental to these sensors. This issue is particularly noticeable when employing only a single pulse of optical pumping light as the data in Fig. 4.1 displays.

64
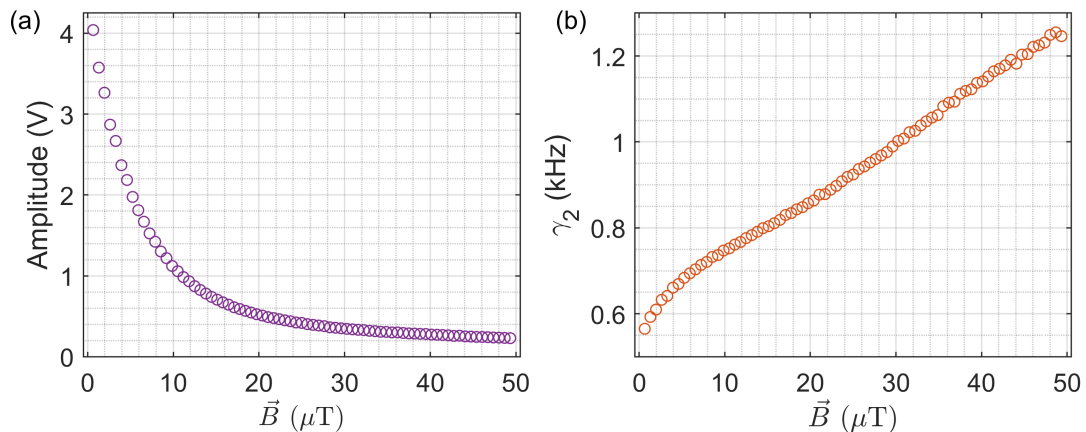
Figure 4.1: Extracted amplitudes (a) and γ_2 rates (b) for a 3 mm thick cell. Stronger bias fields result in lower spin-polarisation being generated when optical pumping involves only a single pulse of light. Statistical errors are smaller than the markers. The magnitude of the transverse field has a drastic impact on the FID signal if no preventative mechanisms to combat this effect, such as either resonantly driving the system at ω_{L}, or employing more novel ways to maintain spin-polarisation are incorporated.

This phenomena can be pictured macroscopically; the transverse measurement field, $\vec{B}_{\mathrm{z}}$, deflects the atomic spin-polarisation created along the beam axis during the optical pumping stage. Methods to circumvent this depolarising mechanism in other systems include aligning the magnetic field parallel to the beam propagation direction. However, as $\sigma^{+/-}$ light induces an atomic orientation[1] in the sample, a parallel field would result in negligible atomic precession, making this scheme redundant. Instead, linearly polarised light would be required to create an atomic alignment[2]. Again, however, this scheme is ineffective in achieving a sufficient atomic polarisation buildup as there exists an alignment to orientation conversion phenomena [79,92,93]. It therefore arises that employing circularly polarised pump light, and aligning the measurement field transversely is a more effective route for measuring precession and thus, a magnetic field.

To counteract this effect, other works have sought to null the field during the optical

---

[1] An atomic orientation refers to a vectorial polarisation moment of rank one. The angular momentum is orientated along a specific axis with a preferred direction (see Fig. 1.1). In this work the atomic spin vector is orientated along the positive x-axis (i.e. the beam propagation direction).

[2] An atomic alignment refers to a tensor polarisation moment of rank two. In that case the angular momentum is aligned along a specific axis with no preferred direction.

pumping stage, thus preventing any deflection from the orientation moment during this period [28]. However, this approach requires prior knowledge of the field to be nulled. An initial measurement must be made to then produce an opposing field of the same magnitude. A more conventional approach is to employ synchronous modulation to the atoms as described in Section 3.1.1. However, again, prerequisite knowledge of ω_L is required to determine the modulation frequency with which to implement, which reduces the available measurement time. Although both of these methods have demonstrated their effectiveness, their disadvantage lies in integrating them into a feedback system, especially in situations where the magnetic field may be constantly changing, such as in portable measurement environments.
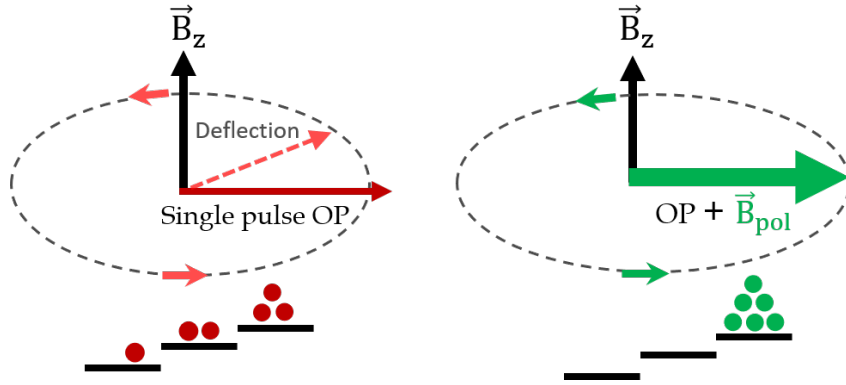
Figure 4.2: A transverse measurement field, $\vec{B_z}$, deflects the induced spin-polarisation away from the optical pumping axis. The spin-polarisation reduces as $\vec{B_z}$ increases. To circumvent this effect and maintain spin-polarisation, the optical pumping pulse can be combined with a strong magnetic field pulse applied along the quantisation axis.

With this in consideration, a more practical solution to addressing these issues was implemented in this work. This entailed producing a substantial magnetic field, $\vec{B}_{Pol}$, along the optical pumping direction during the optical pumping stage, which is illustrated in Fig. 4.2. Henceforth, this technique is referred to as enhanced spin polarisation (ESP). The magnetic field pulse is several mT, over two orders of magnitude greater than the applied measurement field $\vec{B_z}$. As such, it functions as the dominant magnetic field direction to which the atoms are orientated and is synchronised with the optical pumping light. With rapid demagnetisation of this pulse, ESP has demon-

strated its effectiveness in enhancing signal amplitudes and extending atomic coherence times, resulting in heightened sensitivities. Additionally, this technique proved valuable in expanding the dynamic range of the device. Furthermore, the magnetic field pulse also functions as the vapour cell heating mechanism. It capitalises on the conventional FID systems dead-time in order to raise the cell temperature to the optimal atomic vapour density through the resistive heat generated by the coils producing $\vec{B}_{Pol}$.

4.2 Enhanced Spin-Polarisation

To evaluate the effectiveness of ESP, a direct comparison was made with the two other optical pumping techniques described in Section 3.1.1 across a range of bias field strengths ranging from 4 µT to 50 µT. The bias field was applied using the $\pm$ 75 mA current driver [76], which exhibits a lower noise level than the noise floor of the sensor in this chapter.

The measurements were conducted using a 3 mm thick vapour cell containing 220 Torr N_2 under the same experimental setup illustrated in Fig. 3.1. In all cases, heating was performed through resistive heating of the PCB coils surrounding the cell. For the case of ESP, the heating is performed through the act of applying $\vec{B}_{Pol}$. The electronic circuitry which provides the current for $\vec{B}_{Pol}$ and facilitates rapid demagnetisation (1.4 A to $\approx$ 50 pA in 2.5 µs with a 90% to 10% fall time of t = 0.215 µs) is described in detail in [32]. Square copper tracks are printed in a spiral pattern on both sides of a two-layer PCB. Multi-layer PCBs can house more coil turns, thus they can generate greater current in a more compact area, providing a benefit for both magnetic field generation and heating efficiency. A theoretical field to current ratio of 2.7 µT/mA was predicted at the centre of the vapour cell.

The temperature of the cell was controlled by either changing the peak current or the duty cycle of the current pulse generated through the PCB coils. For the ESP scheme, a peak current of 1.4 A was adopted for a duration of $T_{OP} \approx 88$ µs. An identical pump duration was implemented for the SP technique. The repetition rate, f_d, was set to 1 kHz for all. This provided ample time to achieve close to a steady

state spin-polarisation and raised the cell to a temperature of 80 °C, which was found to produce an optimal atomic density. This temperature was maintained using all of the pumping techniques, however, synchronous and SP do not involve applying $\vec{B}_{Pol}$. Therefore, gated heating at 0.5 Hz was specifically introduced for these techniques. Measurements were exclusively enacted during the periods with no current flowing in the PCB coils to ensure that any magnetic interference from the heater did not affect the noise floor of the OPM.
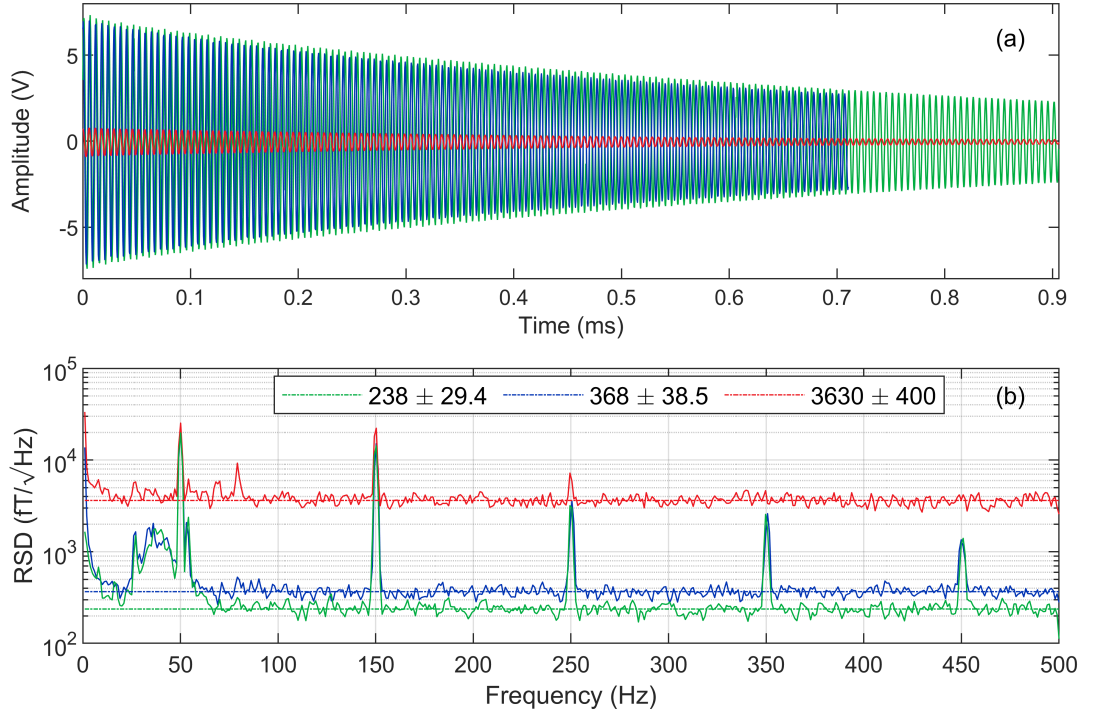
Figure 4.3: (a) FID trace captured using each optical pumping technique under conditions of $\vec{B}_z \approx 50$ μT and T ≈ 80 °C: ESP (green), synchronous (blue), SP (red). (b) Sensitivity spectra for each respective technique indicating the noise floor for each (in units of fT/$\sqrt{Hz}$). An estimation of the sensitivity, ρ_B, was calculated by averaging the spectra over a range between 70 - 500 Hz, outside of obvious technical noise peaks.

The probe frequency was set 20 GHz blue-detuned from the F = 4 to F' transition with a power of ≈ 450 μW for all techniques. Additionally, it was intensity stabilised as described in Section 3.1. This provided a sufficient probe-atom interaction whilst also ensuring that saturation of the detector did not occur. T_{OP} was increased for synchronous optical pumping as the number of cycles required to generate a sufficient

68

polarisation necessitated an increased duration. Saturation of the signal amplitude was found to occur at approximately $T_{OP} \approx 286$ µs. The greater pumping time required to reach saturation detrimentally impacts the OPM in two ways; it increases the dead time, reducing the potential magnetic field extraction efficiency, and also results in a lower T_{Pr}, which negatively impacts the sensors precision according to Eq. 3.7. A consistent peak pump power of 65 mW was maintained for all techniques.

Figure 4.3 (a) portrays a single FID trace relating to each pumping technique at a bias field $\vec{B}_z$ of 50 µT. A reduction in signal amplitude between SP optical pumping compared to the other techniques is immediately clear. Additionally, Fig. 4.3 (b) presents the RSD for each of these techniques. This was calculated as stated in Section 3.2.2, through applying a DFT to 1 second of time domain magnetic field data, found from the consecutive extraction of ω_L from 1000 FID traces. The dashed lines indicates an estimation of the sensitivity for each technique, calculated in the range of 70 to 500 Hz and ignoring technical noise peaks. This range also lies outside the known source of magnetic noise present in the 27 - 55 Hz band, highlighted previously in Section 3.3.2. The figure highlights the improvement in sensor sensitivity performance achieved through synchronous optical pumping, and ESP at this field strength. ESP exhibits the highest overall sensitivity, which is a consequence of a higher overall signal amplitude, coherence time, and a higher available measurement time using this technique compared with synchronous pumping.

4.2.1 Dynamic Range

Results across the full range of bias fields are presented in Fig. 4.4. In the SP regime, an increasing magnitude of $\vec{B}_z$ prevents a strong degree of spin-polarisation being generated. This leads to a significantly lower signal amplitude, A, as shown in (a), and an increase of spin-exchange collisions due to the lower suppression of this depolarising mechanism, directly leading to an increase in γ_2 as seen in (b). It is clear from this data that SP optical pumping is effective at low bias fields only.
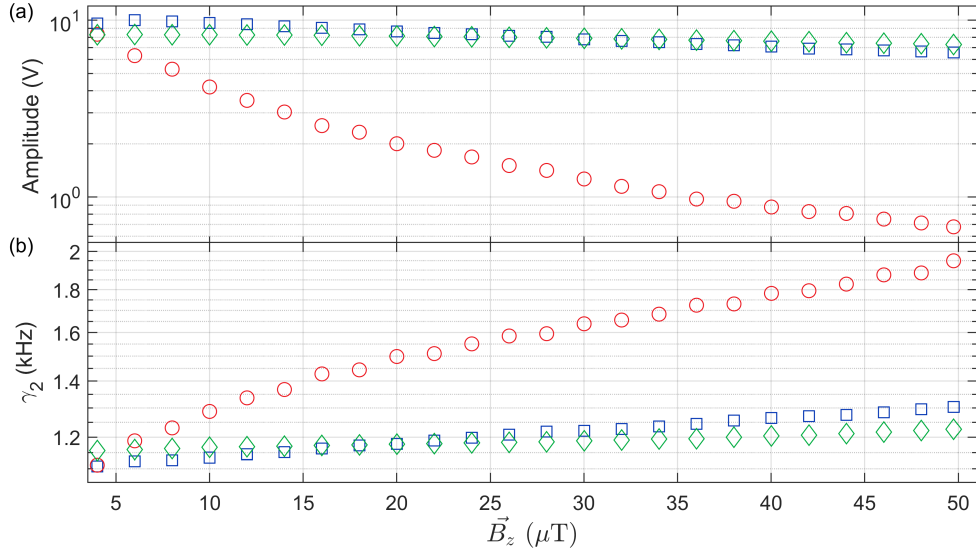
Figure 4.4: Results of extracted FID signal amplitude (a) and γ_2 (b) from the ESP (green), synchronous (blue) and SP (red) optical pumping techniques. Each data point relates to the mean value from ≈ 1000 FID signals, with the markers larger than the affiliated error bars. Improved spin-polarisation was achieved through synchronously driving the optical pump light at ω_L, or by applying a strong field $\vec{B}_{Pol}$ along the beam axis during the optical pumping stage which maintains the largest signal amplitude across the full dynamic range.

Both ESP and synchronous optical pumping generate a larger degree of spin-polarisation, enhancing both A and γ_2. The data demonstrates the sensors improved performance over the full dynamic range when implementing these techniques. As the magnitude of $\vec{B}_z$ approaches its maximum, the ESP displays the best performance. This is attributable to two effects; $\vec{B}_{Pol}$ preventing any significant torque exerted on the atoms from $\vec{B}_z$, which is not the case for synchronous optical pumping, and more importantly, a reduced broadening impact caused by nonlinear Zeeman splitting (NLZS) during ESP.

As described in Section 2.3.1, NLZS acts as to broaden the magnetic resonance. This expedites the spin-relaxation rate, becoming more influential at higher field magnitudes. This phenomenon results in only a slight loss in signal amplitude for ESP for increasing $\vec{B}_z$ values, with a clearer degradation observed for synchronous optical pumping. This is expected as the required process of resonantly driving the atoms at ω_L for the synchronous technique becomes more complicated. The non-linearity of the

Zeeman sublevel structure results in a spread of ω_L's (with a maximum $\Delta f = 54$ Hz) with which the optical pump light cannot resonantly address uniformly. A depiction of the overlap of the individual Zeeman coherences within F = 4 is provided in Figure 4.5, with arbitrary linewidths and amplitude values used. The optical pumping dynamics will severely influence the atomic distribution i.e. the majority of atoms will be pumped into the stretched state. This figure therefore serves as an illustrative example only. In other works, Radio-Frequency (RF) spectroscopy was successfully used to determine the individual Zeeman coherence amplitudes [35].
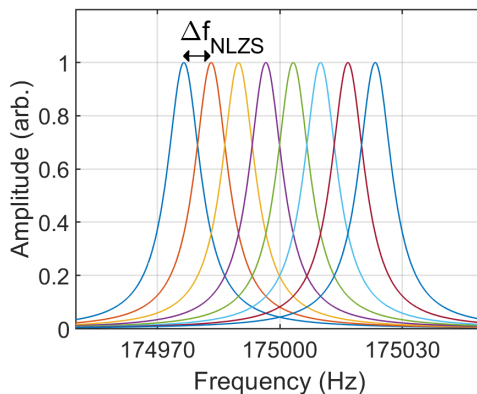
Figure 4.5: Illustrative effect of NLZS in the F = 4 ground state manifold. At geomagnetic field strengths $\Delta f_{\mathrm{NLZS}} \approx 6.7$ Hz, resulting in slightly different spin-precession frequencies between the Zeeman sublevels. Eight distinct overlapping Lorentzian profiles describe the Zeeman coherences in the respective order of $m_F = -4 \leftrightarrow m_F = -3$ to $m_F = 3 \leftrightarrow m_F = 4$. The Δf disparity ultimately leads to a broadening of the magnetic linewidth (increase of γ_2).

While the same nonlinear distribution is also present using the ESP technique, the lack of requirement to resonantly drive the system presents an inherent advantage. However, NLZS also impacts the OPM performance at higher bias field magnitudes for ESP. An increase of ≈ 80 Hz for γ_2 is observed over the full range which is mainly ascribable to the broadening caused by the NLZS. In this work, where the suppression of the NLZS has not been pursued, it is rather challenging to accurately quantify the exact linewidth broadening caused by NLZS. Other works such as [94], have demonstrated the NLZS broadening effect at $\vec{B} = 62$ µT, resulting in an effective magnetic linewidth

of 120 Hz, despite each Lorentzian peak exhibiting a linewidth of 9 Hz with adjacent separations of $\Delta f_{\mathrm{NLZS}} \approx 10$ Hz. It should be noted that this 120 Hz effective magnetic linewidth will also include all other broadening mechanisms incurred in the system. For the energy (frequency) splitting, Δf_{NLZS} between the Zeeman coherences has been measured in [95] with values ranging from 6.5 Hz to 8.7 Hz, in close agreement to the 6.7 Hz expected from theory.

In this work, the lower limit that broadening caused by a magnetic field gradient [96] across the vapour cell can, however, be quantified. The beam waist of 3.1 mm $(1/e^2)$ and coil geometry indicate a magnetic field discrepancy of only $\Delta_{\mathrm{B}} \approx 5.5$ nT (Eq. 6.1), resulting in a variation of only 19 Hz calculated through $\gamma_{\mathrm{grad}} \approx \gamma \Delta B$ [97]. Therefore, the NLZS effect is the main contributor to the 80 Hz broadening. As will be discussed in the latter sections of Chapter 5, a degradation in γ_2 remains true in this system, despite the clear improvement that ESP makes when operating at higher bias fields.

4.2.2 Noise Characterisation

A characterisation of the noise in the system was also assessed for each technique. This enabled the noise budget of each respective technique to be determined, as an accurate estimation of the noise level, ρ_{A}, facilitates an accurate estimation of the CRLB from Eq. 3.7. A RSD was computed for each pumping technique through averaging 20 successive DFTs, determined from their respective FID traces throughout the probe interval T_{Pr}, at $B_{\mathrm{z}} \approx 50$ µT. Additionally, noise spectra was captured under the same experimental conditions, however, with no pump light applied and also no probe light applied. In these cases the spectra were also collated using 20 successive time series traces, however, over the full 1 ms interval set by f_{d} due to there being no optical pumping which reduces the duration to $T_{\mathrm{Pr}} = T - T_{\mathrm{OP}}$.

The RSD for each of the aforementioned conditions is presented in Fig. 4.6. This highlights the improved SNRs attained using the synchronous and ESP techniques. The extended duration T_{OP} allocated to optical pumping in the synchronous approach leads to a slightly broader spectral peak compared to ESP. Incorporating independent pump and probe lasers in the scheme enables the noise density from the probe to be

determined in the absence of any pump light. Consequently, for each technique, the background noise level at frequencies far from ω_L closely approximates the spectra obtained in the absence of pump light.
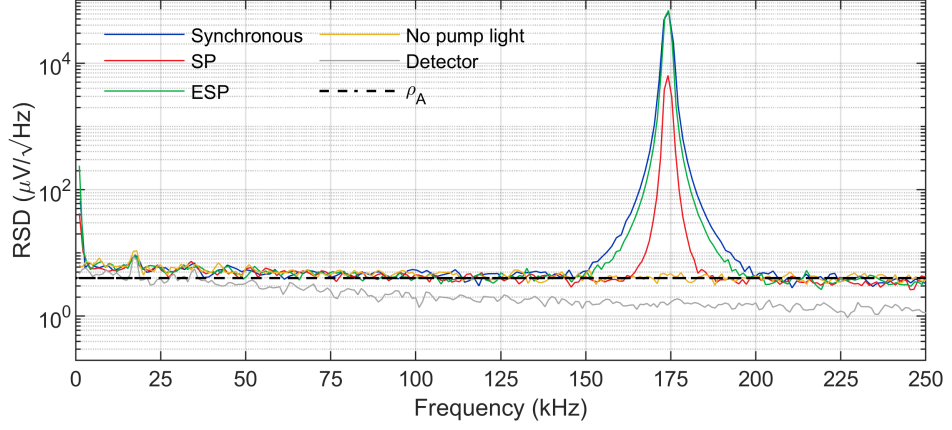
Figure 4.6: RSD data for each pumping technique along with the noise spectra determined in the absence of pump light (orange). The detector noise is also displayed when no light is present (grey). The dashed line indicates the average noise density ρ_A, calculated across a 2 kHz range centered at $\omega_L \approx 2\pi$ x 175 kHz.

A determination of 4 $\mu V/\sqrt{Hz}$ for ρ_A was found from calculating the average noise level spread over a 2 kHz range centered about ω_L. This process provides an accurate estimation of the true noise level in the system and can be utilised in the calculation of the ultimate sensitivity achievable under these conditions set by the CRLB. In these experiments, approximately 63% of probe light remains after atomic absorption and other losses in the system, equating to around 283 μW reaching the detector. This provides a ρ_{SN} value of 3.7 $\mu V/\sqrt{Hz}$ according to Eq. 3.9. Consequently, the value for ρ_A agrees with the theoretical expectation from adding ρ_{SN} in quadrature to the inherent detector noise of the system which was measured as 1.5 $\mu V/\sqrt{Hz}$ as shown in Fig. 4.6 (grey trace).

4.2.3 Sensitivity Performance

The calculated experimental sensitivities, ρ_B, and the CRLBs found for each pumping technique are displayed in Fig. 4.7. These were computed following the procedure

described in Sections 3.2.2 and 3.2.3. The effectiveness of the ESP technique is clear across a large dynamic range. One may expect the degradation of both A and γ_2 for increasing $\vec{B}_z$ amplitudes to negatively impact the sensitivity performance. However, this is not the case as the overall noise level ρ_A reduces at higher bias fields (see Figs. 3.8 (b) and 4.6). The uncertainty on the respective ρ_B values is accounted for by the error bars which are determined from calculating the standard deviation over the 70 - 500 Hz band in the absence of the technical noise peaks. The main source of uncertainty in the CRLB values arise from assessing ρ_A, as the statistical error determined from 1000 FID traces for A and γ_2 are negligible. The uncertainty on ρ_A is also calculated from measuring the standard deviation across a 2 kHz frequency range around ω_L from Fig. 4.6.
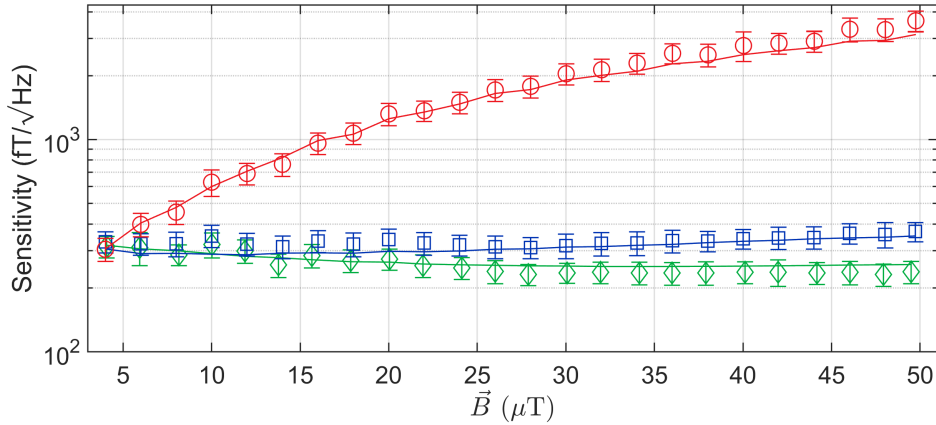
Figure 4.7: Sensitivity comparison for the ESP (green), synchronous (blue) and single pulse (red) pumping techniques. The calculated CRLBs for each, found to match the experimental sensitivities, are also included as solid lines for each respective technique. The associated errors on the CRLB are similar to those of the experimental data points.

Imparting magnetic noise via heating of the vapour cells can be problematic in OPM systems. In this work, the values for ρ_B agree with those set by the CRLB for each technique. This confirms that any magnetic noise introduced either through the $\vec{B}_{Pol}$ heating approach, or from the magnetic current source producing the bias field are below the noise floor of the sensor, thus not negatively impacting the sensor performance. A swift demagnetisation of the field generated by applying $\vec{B}_{Pol}$ takes place through the

electronic circuitry, diminishing to approximately 135 fT, as detailed in [32]. Further improvements in the sensitivity performance may therefore only be gained by improving any of the parameters listed in Eq. 3.7. As the sensor is photon-shot noise limited, a sensible route forward for improved sensitivity at high bias fields will be to incorporate the ESP technique with thicker vapour cells, which facilitate larger SNRs whilst exhibiting longer coherence times. Results relevant to this are the subject of a sensitivity assessment study of 6 mm thick cells, presented in Section 5.4.

ESP has proved the most effective in terms of sensitivity performance over the full range. Additionally, it has resulted in an improved dynamic range, and reduction in dead-time, demonstrating its suitability for sensing within geomagnetic field strengths.

4.3 Improved Accuracy

The accuracy of any FID magnetometer relies on generating a strong spin-polarisation to minimise heading error [98], and on minimising light shift systematics. The temporal separation of the pumping and probing stages in the FID configuration includes extinguishing of the pump light via the AOM, circumventing this intensive light-atom interaction during the detection stage. Light shifts due to the probe-atom interaction can occur, however, which can be reduced by detuning the probe beam further from resonance [51]. Moreover, they can be almost fully eliminated through applying a delay between the end of the pump and beginning of the probe stage [33].

A lower overall degree of spin-polarisation was achieved using the less efficient SP optical pumping at fields exceeding a few µT. At geomagnetic field strengths, the technique becomes completely inefficient at generating a large spin-polarisation in the ensemble. This is reinforced by comparing the linearity of the OPMs response as a function of bias field amplitude using the SP and ESP techniques. The data in Fig. 4.8 (a) displays the residuals of a linear fit to the measured magnetic field data.
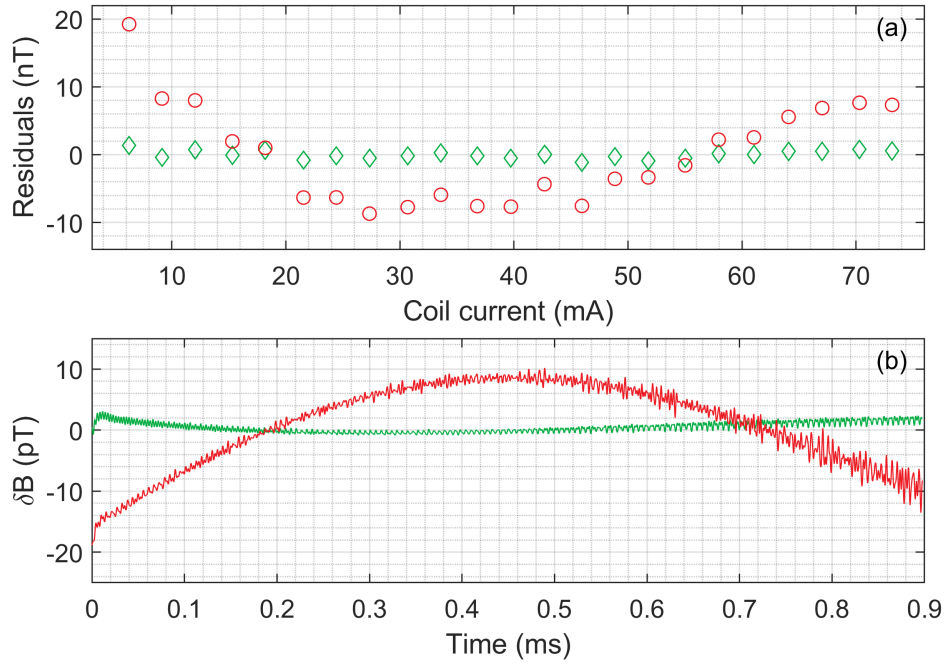
Figure 4.8: (a) Residuals from a linear fit of recorded magnetic field data (1 s) as a function of bias field coil currents. (b) Variation in residuals in the instantaneous magnetic field recorded over a full FID probe cycle for both ESP and SP. The data here, calculated using a Hilbert transform, is an average of 50 consecutive FID cycles Green (red) data points relate to the ESP (SP) techniques.

The coil supply current was incrementally increased, with 1 s of recorded magnetic field data captured at each interval. When employing ESP, the OPM produces a linear response as a function of increased bias field with the residuals fluctuating around zero with no clear trends. SP optical pumping, however, results in the residuals displaying a quadratic-like trend across the bias field. This is ascribed to the aforementioned lower spin-polarisation generated, resulting in the measured Larmor frequency being weighted by a significant contribution from atoms occupying both hyperfine states. To improve the accuracy of this, a double sinusoidal model would be required (see Section 4.4. All optical pumping techniques suffer from NLZS at elevated bias fields, however, for SP pumping this decohering effect is much lower than that caused by spin-exchange.

As presented in the previous sections, the ESP technique facilitates a significantly higher degree of spin-polarisation by circumventing the depolarising impact of the transverse measurement field. A large atomic population is created and maintained within

76

the F = 4 hyperfine manifold, which suppresses spin-exchange collisions. Consequently, this technique inherently offers superior accuracy compared to SP optical pumping, provided that the residual magnetic field diminishes rapidly. This was previously tested electronically, where the transient current response was measured with a $\approx$ 200 ns fall time and decay to 135 fT. The data relating to this measurement is provided in [32]. To address the transient magnetic response using the OPM, a separate signalling processing strategy using a Hilbert transform (HT) was implemented.

A HT, $\mathcal{H}\{S(t)\}$, calculates the instantaneous Larmor precession frequency by linearising the FID signal and retrieving the instantaneous phase through applying a $\pi/2$ phase shift to the original signal [31]. An analytic description of the signal phasor, $S_a(t)$, is represented by,

$$S_a(t) = S(t) + i\mathcal{H}\{S(t)\}, \tag{4.1}$$

where $S(t)$ is the original trace and $\mathcal{H}\{S(t)\}$ is the $\pi/2$ phase-shifted signal described by,

$$\mathcal{H}\{S(t)\} = \frac{1}{\pi}\mathcal{P}\int_{-\infty}^{\infty}\frac{S(\tau)}{t - \tau}d\tau \tag{4.2}$$

with $\mathcal{P}$ representing the Cauchy principal value [99]. From this equation, the instantaneous signal amplitude and phase are found from calculation of the radius and angle of $S_a(t)$ in the complex plane. ω_L and the initial phase are obtained from the gradient and intercept of the linearised phase. This alternative data processing greatly increases the bandwidth of the OPM. Resolution of frequencies up to the Nyquist limit of the DAQ device are enabled, therefore, in this case, extending the system bandwidth by a factor of 2500. As a result, the atomic response to the rapidly decaying magnetic field pulse becomes measurable.

The HT was applied to the FID data for both techniques for a bias field of $\vec{B}_z \approx$ 50 µT. A dual matched finite-impulse response filter, producing the full signal phasor was incorporated. This enabled the signal phase at each DAQ clock cycle to be retrieved, and then, therefore, the instantaneous ω_L. A consistent temporal variation

was observed over a full FID probe cycle when employing the SP technique, with less variation found for ESP. These trends were verified further by averaging 50 consecutive FID probe cycles with the results of the residual variation in the instantaneous magnetic field displayed in Fig. 4.8 (b). No current is passed through the PCB coils when employing SP, therefore, the observed systematic variation in the calculated ω_{L} (magnetic field) is not a result of demagnetisation. The behaviour is instead a consequence of the increased rate of spin-relaxation, in addition to an increased NLZS induced heading error.

The NLZS effect at geomagnetic field amplitudes creates a relation between the measured Larmor frequency and the Zeeman sublevel populations. The ground-state spin-relaxation is a dynamic process, therefore the populations evolve throughout the FID cycle as the field is calculated at each clock cycle of the DAQ. ESP maintains a more steady atomic population compared to SP. A lower fluctuation in the calculated magnetic field is therefore found, indicating that a less pronounced population evolution occurs compared to SP. Overall, the FID traces were devoid of any detectable imprints of the demagnetisation at the start of the measurement i.e. at t = 0. As a result of the improved spin-polarisation, spin-coherence, sensitivity, and accuracy, the ESP technique is implemented in all future data presented in this thesis.

4.4   Altering the Atomic Distribution

Throughout the majority of the work presented in this thesis, the intentional dual distribution of atoms was avoided, through optically pumping on the F = 3 to F' transition of the N_2 pressure broadened cells. However, interesting results are found when pumping on the F = 4 transition, as a sizeable proportion of atoms are found in both ground-state hyperfine levels. This section explores this effect with a discussion of its use for comagnetometry purposes.

4.4.1 Pump Frequency Impact

As outlined in Section 2.4.4 and illustrated in Fig. 2.7, the optical pumping dynamics have a significant impact on the distribution of atoms in the ground-state hyperfine levels. These have different Landé g_F factors, i.e. $g_F \approx 1/4$ for F = 4 and $g_F \approx -1/4$ for F = 3, resulting in their atomic precession occurring in opposing directions as seen from Eq. 2.3. Additionally, they precess at slightly different frequencies with the approximate difference in spin precession frequency given by $\gamma_3/\gamma_4 \approx 1.00319$ [100]. Thus, the independent sets of atoms are identifiable through their respective Larmor frequencies.

The approach used in this work to induce a sufficient atomic population in both ground states is to purposefully tune the pump laser to the F = 4 to F' transition. To extract information regarding the distinctive atomic spin-precession, including measuring both Larmor frequencies, a double sinusoidal model is required, given by:

$$
\begin{aligned}
S_n = A_3 \sin\left(\omega_{L_3} \, n \, \Delta t + \phi_{0_3}\right) e^{-\gamma_{2_3} \, n \, \Delta t} \\
+ A_4 \sin\left(\omega_{L_4} \, n \, \Delta t + \phi_{0_4}\right) e^{-\gamma_{2_4} \, n \, \Delta t} + \epsilon_n,
\end{aligned}
\tag{4.3}
$$

where the subscripts 3 and 4 relate to atoms identified as belonging to these respective ground states. This model provides both respective amplitudes, phases, spin-relaxation times, and Larmor frequencies for each set. The temporal separation of pumping and probing reveals a distinct visual discrepancy in signal shape when varying the pump frequency. This effect is illustrated in Fig. 4.9 which presents a select portion of signal data for a 3 mm cell containing around 220 Torr of N_2 buffer gas, heated to a temperature of 79 °C.
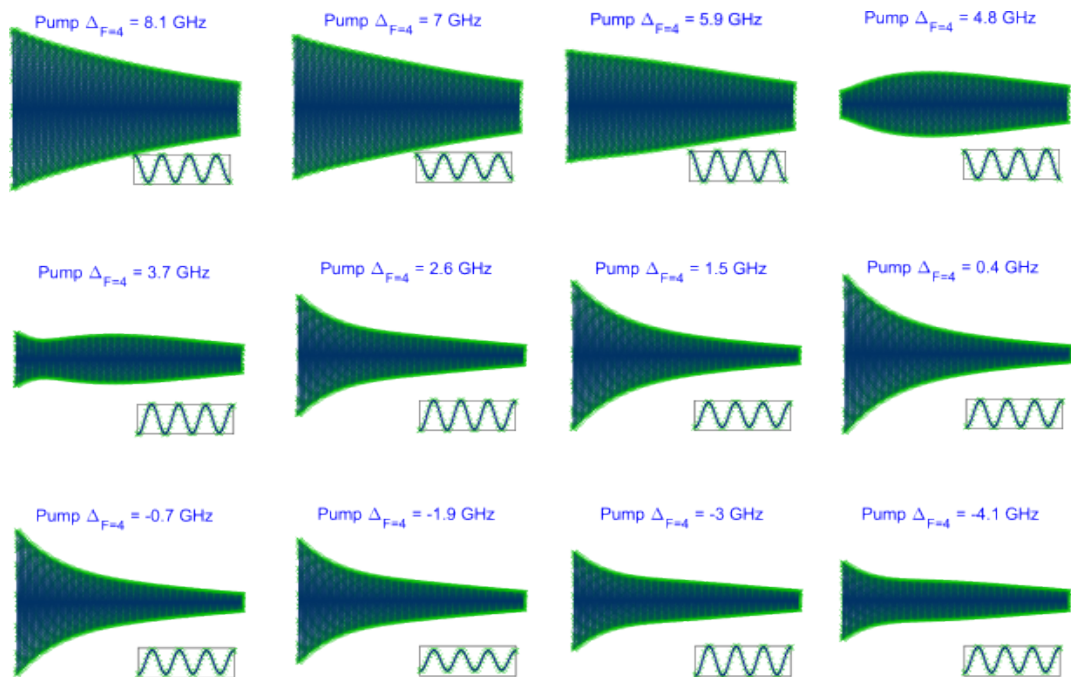
Figure 4.9: Visualisation of selected FID signals for a varying pump frequency. All plots are on the same vertical scale. Each pump frequency variation shown here is $\Delta_f \approx 1.1$ GHz. The pump frequency is set to be blue-detuned from the F = 3 to F' transition and then incrementally varied until it is red-detuned from the F = 4 to F' level. The experimental setup involved utilising the following parameters: $P_{probe} = 595$ µW, $P_{pump} = 63$ mW, and the temperature was 79 °C. Additionally, a magnetic field of 50 µT was applied.

The recorded amplitudes from this dataset are presented in Fig. 4.10 (a). Additionally, Fig. 4.10 (b) showcases the respective amplitude values when an alternative probe frequency was used, while maintaining the same optical pumping conditions. In (b) the probe frequency was set 40 GHz red-detuned from the F = 4 to F' transition, with a power of 243 µW, resulting in a comparatively weaker probe-atom interaction strength.

The figure quantitatively displays the clear disparity in the signal amplitudes obtained as a result of altering the optical pumping frequency. A sizeable proportion of atoms are found in both ground states when pumping on F = 4. This is in contrast to the preferred case of pumping on the F = 3 transition (highlighted with green dashed vertical line), which leads to an almost full evacuation of atoms into the F = 4 state. The purpose of this data is twofold; it firstly demonstrates clear evacuation of

atoms from the F = 3 ground state when pumping on F = 3, and secondly, provides clarity on the population disparity achieved when pumping close to F = 4. Although dual atomic distribution is conducive for obtaining independent spin-precession measurements, it is directly related to increasing the rate of spin-exchange collisions and, therefore, reducing the overall spin-relaxation T_2 time.
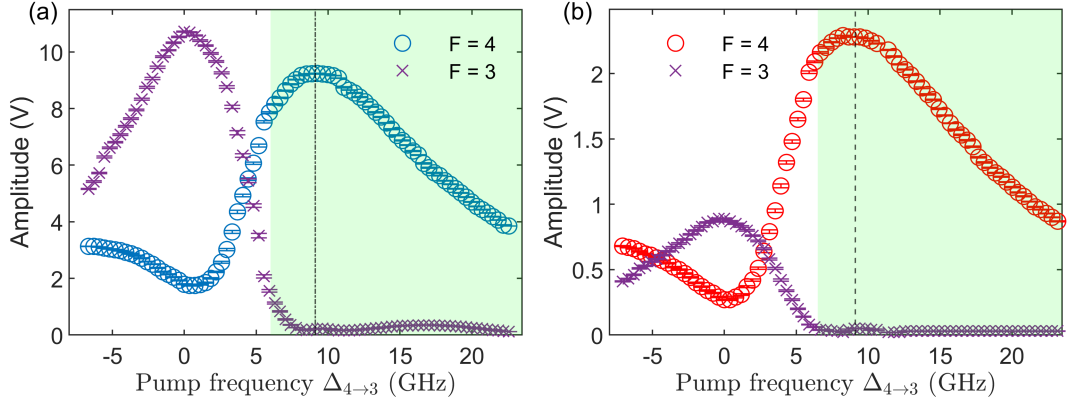
Figure 4.10: (a) The probe beam is 20 GHz blue-detuned with the pump frequency varied. Atoms determined to be occupying F = 4 using Eq. 4.3 are in blue whilst those in F = 3 are purple. (b) Probe beam is 40 GHz red-detuned with the F = 4 atoms displayed in red. Two different probe detunings and probe powers were used for (a) (593 µW) and (b) (243 µW), providing different light-atom interaction strengths, thus measured signal amplitudes. The figure highlights that pumping on F = 3 results in the vast majority of atoms being distributed in the F = 4 level, with a negligible amount found in F = 3. Conversely, when pumping on F = 4 there is a considerable amount found in both. The dashed vertical lines indicate the F = 3 to F' transition. The green shaded area indicates the optical pumping frequency region which effectively polarises atoms into F = 4. The non-shaded zone displays the pump frequency range which can be exploited for comagnetometry.

It should be noted that the interaction strength i.e. the signal amplitude is impacted by the probe's frequency and intensity. This is particularly evident from considering only the data when pumping on F = 4. In (a) the probe frequency is in closer proximity to the F = 3 to F' transition leading to a greater interaction strength with F = 3 atoms and a large signal amplitude. Conversely, in (b) the probe frequency is closer to the F = 4 to F' transition, resulting in a stronger interaction with the F = 4 atoms. An equal interaction strength for both sets of atoms is found at the intersection points.

The double sinusoidal model also aids in improving the accuracy of the sensor for the case where low spin-polarisation is generated. Incomplete evacuation of the F = 3 hyperfine level causes a skewing of the measured Larmor frequency, which is essentially a form of heading error [101]. This skewing can be compensated for analytically in the regime of high spin-polarisation, i.e. the green shaded region in Fig. 4.10.

4.4.2 Atomic Comagnetometry

Atomic comagnetometers operate by concurrently measuring the distinct spin precession of two or more coinciding species. The ratio between their independent Larmor precession frequencies is insensitive to magnetic field changes, however, the sensor maintains sensitivity to nonmagnetic spin interactions [102]. This aspect can be utilised and used for fundamental physics research [103]. There are also practical applications for these in inertial rotation sensing.

Typically, an alkali metal is paired with one or more noble gas species such as helium (He) or xenon (Xe) [104, 105]. However, comagnetometers employing different species can suffer from systematic errors due to magnetic field gradients. If present, these can result in each species experiencing slightly different average positions, thus sensing a different magnetic field. Several mechanisms cause this disparity, including differences in thermal diffusion rates, spin-polarisation buildup, the resulting transverse relaxation rate, and from the force of gravity. Recent methods have sought to suppress these errors by temporally separating the pumping and probing stages, and measuring the spin precession of noble gas species in the absence of light i.e. in the dark. For example, in [105], ^{87}Rb atoms are employed and used to facilitate a measurement of the ratio of the ^{3}He to ^{129}Xe spin-precession, providing sufficient accuracy to measure the Earth's own rotation. Nonetheless, a single atomic species would naturally not experience such severe systematics caused by experiencing a magnetic field discrepancy. Works such as [100, 106] have demonstrated suppression of systematic errors by using singular alkali-metal species of Cs and ^{87}Rb respectively.

Attaining an equitable parity of polarised atoms is advantageous for comagnetometry. Employing D_2 line optical pumping on the F = 4 to F' transition in conjunction

with collisionally broadened Cs vapour cells facilitates this. OPM systems that do not incorporate sufficient buffer gas pressures may exhibit spectroscopically resolvable ground to excited state transitions. However, the eventual distribution of atoms within the ground state can display a slight bias towards one state, making an equal ratio difficult to achieve without additional measures i.e. employing an additional pump laser [100]. The FID configuration permits a fairly straightforward observation of these counter precessing signals.

In light of this, the intentional dual distribution of atoms is now presented for a 6 mm thick cell containing around 180 Torr N_2. Optical pumping on F = 4 to F' was carried out with the probe frequency adjusted until an approximate 1:1 ratio of detected amplitudes were reached. The bias field along $\vec{B_z}$ was set to 50 µT, providing adequate Δf spacing to be able to view the distinct components in the frequency domain. Maximising the coherence time was key to achieve this, therefore, a comparatively low cell temperature of $\approx$ 45 °C was employed.

Figure 4.11 (a) and (b) presents the respective temporal FID signal and frequency domain data. The double sinusoidal signal is evident, with the counter precessing atoms initially with opposite phase and close to equal amplitudes. As the precession evolves they decohere through the mechanisms described in Section 2.5, with the signal reviving before reaching thermal equilibrium, akin to the signal displayed in [107]. The approximate T_2 times for the F = 4 and F = 3 atoms are 1.4 ms and 1.2 ms respectively. The coherence time sets the frequency resolution with which the frequency domain data is displayed. Utilising alternative atomic species, such as the natural isotopes ^{85}Rb and ^{87}Rb, would induce a significant difference in precession frequency, leading to the generation of two entirely separate peaks. However, there is the additional added complexity of atomic distribution across four separate ground states.
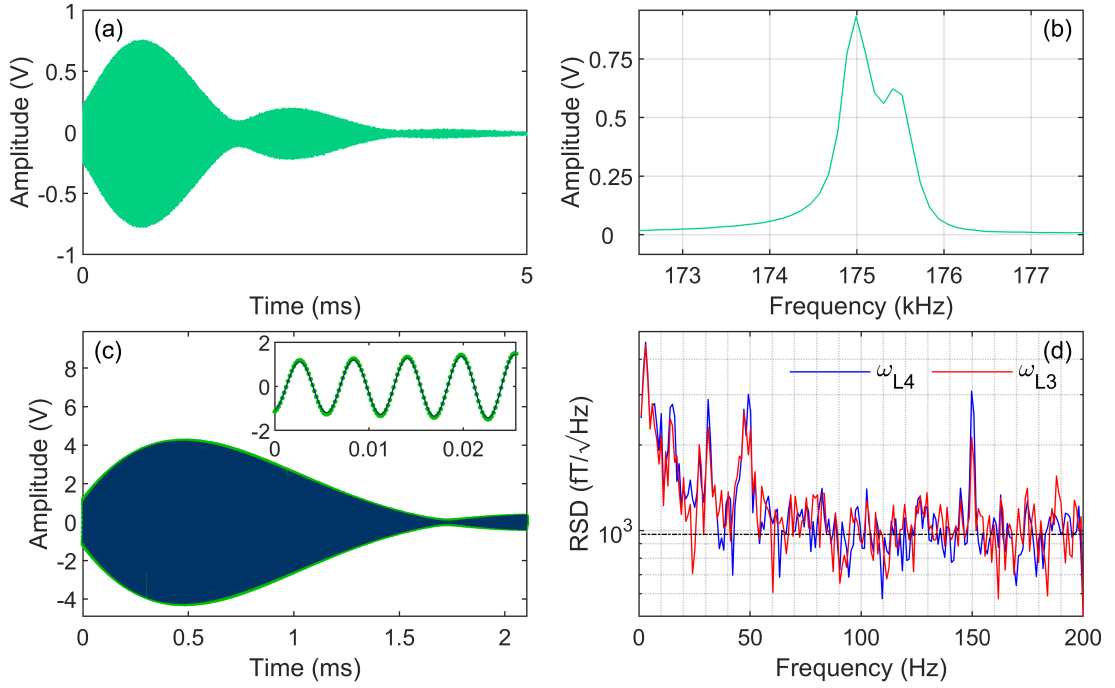
Figure 4.11: (a) FID cycle comprised of two independently precessing frequency components. The net signal decays and revives before reaching thermal equilibrium. The high bias field (50 µT) combined with a low vapour density facilitates a longer coherence time with sufficiently spaced $\Delta\omega_L$, observable in the frequency domain (b). (c) FID cycle and associated double sinusoidal fit relating to an increased vapour density which provides a better sensitivity performance. (d) Comagnetometry: Magnetic sensitivity extracted for the two counter precessing sets of atoms in the ground states F = 4 and F = 3 from (c). A sensitivity below 1 pT/$\sqrt{\text{Hz}}$ is achieved for both.

The sensitivity performance of the comagnetometer was also examined. The atomic vapour density was increased to $\approx$ 45 °C to achieve a larger SNR. An example FID trace from the signal train, along with associated fit using Eq. 4.3 is displayed in Fig. 4.11 (c). This data pertains to a peak optical pumping power of 120 mW at a repetition rate of f_d = 400 Hz. The Nyquist limited bandwidth is therefore limited to 200 Hz. The sensitivity data for both ground state atoms in this dataset is presented in Fig. 4.11 (d), which relates to 10 averaged FID signal trains. Sensitivities of 950 ± 160 fT/$\sqrt{\text{Hz}}$ and 970 ± 180 fT/$\sqrt{\text{Hz}}$ were determined for F = 4 and F = 3 respectively. These were calculated outside the range of known technical noise sources such as the low frequencies, and the magnetic noise band already described in Section 3.3.2. This appears the

first demonstration of a Cs MEMS cell comagnetometer system achieving sub $\mathrm{pT}/\sqrt{\mathrm{Hz}}$ level sensitivities. Additionally, the comagnetometer performance at Earth's magnetic field amplitude is competitive with conventional portable magnetometer devices [108]. The uncertainty in these measurements would be improved by utilising Welch's method over a longer period (see Section 3.2.2).

Rotational sensing constitutes a key application for atomic comagnetometers. Measuring the Earth's rotation using a Cs MEMS cell would be challenging. For example, Earth's rotational rate, Ω_{Earth}, of ≈ 1.15 x 10^{-5} Hz will induce a fictitious magnetic field of approximately 3.3 fT ($\Omega_{\mathrm{Earth}}/\gamma \approx 3.3$ x 10^{-9} µT). Consequently, the resulting shift in the Larmor frequency falls below the current sensitivity limit of the setup, with rotations $\geq 3.5 \times 10^{-3}$ Hz being more achievable at present. Improvements on the stability of the system are necessary in order to detect this variation, such as implementing improved magnetic shielding, i.e. additional layers. However, with some restructuring the idea is not completely unfeasible. An advantage lies in the fact that only one pump and probe laser is required, therefore, laser instabilities are likely to be common mode to both sets of Cs ground state atoms. Alternatively, detecting systems with faster rotational rates or utilising the sensor for inertial navigation is applicable. The required sensitivity would be less demanding due to the greater measurable shift in the distinct precession frequencies i.e. a 1 Hz rotational rate would require a sensitivity of only around 0.3 nT.

The utilisation of a single-atomic species within a compact cell volume is useful. Notably, it reduces the impact of magnetic gradients, which is a drawback that larger cells suffer from. Smaller cells, however, do produce lower spin-coherence times, limiting their sensitivity. Single species vapour cells are most commonly manufactured, making them more easily accessible. Cs distinguishes itself over other alkali species due to its higher vapour density, presenting the inherent advantage of operating at lower temperatures, therefore, reducing the power consumption. Clearly, this is beneficial in the context of portable magnetic sensing, where the design of practical sensors is motivated by low size, weight, cost and power [56]. Accordingly, a device such as this may be implemented in space applications [109], with the ability to employ the system

85

either as a magnetometer or a comagnetometer.

Chapter 5

Intrinsic Relaxation Rates

This chapter discusses and expands on the technique described in [54], in which the N_2 buffer gas pressure is incrementally reduced through the heating of a Cs dispenser pill. The pill, placed within a 6 mm thick MEMS vapour cell is irradiated with intense laser light, releasing Cs and acting as a getter to consume N_2. A characterisation of the impact of N_2 pressure on the performance of the OPM is presented.

Commonly, micro-machined cells are manufactured with a uniform target pressure intended across the entire wafer [48]. A buffer gas is necessary to reduce the rate of alkali-wall collisions. However, the optimal pressure varies according to cell geometry and OPM application. For example, in magnetic imaging applications, higher buffer gas pressures reduce the rate of alkali diffusion (see Chapter 6). However, at elevated pressures the increased spin-destruction collisions incurred between alkali and buffer gas atoms can lead to a decline in performance. Therefore, having a method to tune the pressure to the optimal value efficiently and controllably is a valuable technique for the MEMS cell industry, including for atomic magnetometers and clocks [110]. This technique serves as a pathway for reducing the buffer gas content of any cell at the wafer level after fabrication.

The spin-relaxation rate sets a limit on an OPMs total possible measurement time. Both of these parameters impact the sensitivity performance according to Eqs. 3.6 and 3.7. The FID configuration is well-suited for accurately assessing the spin-relaxation rate. Various intrinsic relaxation mechanisms inherent to vapour cells have been pre-

viously described in Section 2.5. The intrinsic longitudinal relaxation rate, γ_{10} (Eq. 2.28), is the ultimate spin-relaxation limit. In order to measure γ_{10}, all other decohering contributions, including those induced through typical experimental operation such as power broadening have to be circumvented. Magnetic gradients across the cell should also be eliminated. Furthermore, the primary depolarising mechanism for this OPM, spin-exchange, must be suppressed. Successful extraction of γ_{10} therefore required the system to be operated at a low bias magnetic field strength (1 µT), where magnetic gradients are effects are minor, and a low cell temperature (30 °C), where the influence of spin-exchange is negligible. The impact of spin-exchange collisions increases significantly with vapour density, leading to an elevation in γ_{20}. However, an insignificant increase in γ_{10} occurs for higher vapour densities, as illustrated in Fig. 5.1.
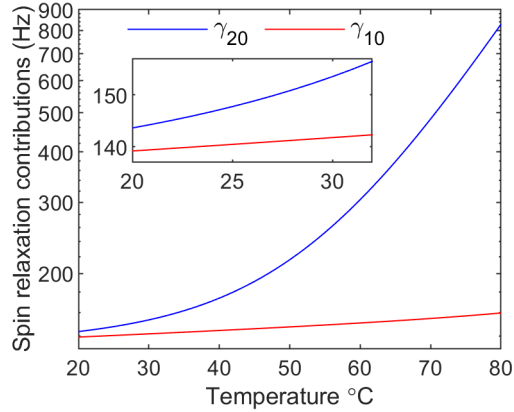
Figure 5.1: Theoretical dependence of the longitudinal (γ_{10}) and transverse (γ_{20}) spin-relaxation rates against temperature for a 120 Torr cell resembling the 6 mm thick cell geometries used in this work. Calculated using Eqs. 2.28 and 2.30 from Section 2.5. γ_{10} rates do not significantly increase as a function of temperature in contrast to γ_{20} rates.

Sequential measurements were conducted across various pressures after each iterative depletion, facilitating confirmation of the N_2 pressure content that minimised γ_{10}. Based on the N_2 pressure range available, the expectation prior to the measurements was that there would not be a significant discrepancy between each extracted value. This was due to the theoretical model and the selected experimental conditions which suppressed spin-exchange.

Additionally, subsequent to the cell activation and each buffer gas reduction, the magnetic sensitivity performance across the range of N_2 pressures at a magnetic field amplitude of $|\vec{B}| \approx 50$ µT was assessed. The findings from this are presented in Section 5.4. Emulating Earth's magnetic field magnitude provides a more meaningful performance benchmark for a total field OPM sensor. Going forward, portable OPM devices will likely commonly incorporate MEMS vapour cells for utilisation in real world sensing applications.

5.1 Buffer Gas Characterisation

5.1.1 Pill Activation

The initial cell activation phase, in which the alkali is released, is a process only feasible under heightened thermal conditions (T > 600 °C). A high power and fibre-coupled Yb laser (3 W at 1070 nm) was aligned with a tight focus to the alkali dispenser pill, sized approximately 1 mm in diameter. This resulted in a thermal energy transfer as the temperature of the pill rapidly increased, leading to the release of Cs. The duration of irradiation under these conditions was between 10 - 40 s. As the Cs vapour in the cell was released via the alkali pill source, the initial atomic diffusion to the main spectroscopic chamber was not immediate. Instead, this diffusion is a heat driven process. Therefore, to expedite this, after the initial activation the cell was heated to a temperature of 100 °C. After approximately one hour of heating, the Cs diffused into the main spectroscopic chamber. A saturated Cs vapour was observed, permitting an analysis of the N_2 content based on the collisional shift and broadening. OPM measurements were then performed to extract the relevant metrics; namely the γ_{10} rate and the sensitivity performance. The cell was then irradiated again until an appropriate reduction in N_2 was spectroscopically determined. Figure 5.2 depicts this iterative and irreversible process.
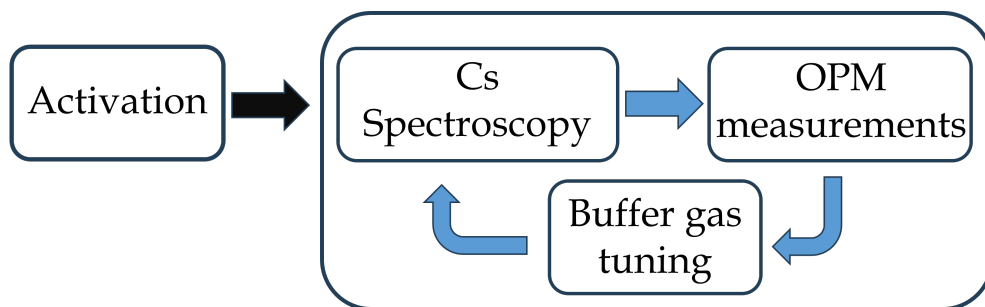
Figure 5.2: Process of activating the cell and measuring the buffer gas pressure before then assessing the OPM performance. Subsequently, the buffer gas pressure was reduced before continuing the cycle.

Multiple cell geometries were investigated throughout this work. Figure 5.3 (a) illustrates a sketch of the principal cell geometry, which was a cuboid cell of 6 x 6 x 6 mm. An extensive range of measurements across a N_2 pressure range of $\approx$ 57 to 162 Torr were conducted. However, to further corroborate the data, additional measurements were made using another cell with a cylindrical geometry, as also depicted in Fig. 5.3 (a). For the remainder of this chapter these cells will be referred to as the cuboid and cylindrical cells, respectively.
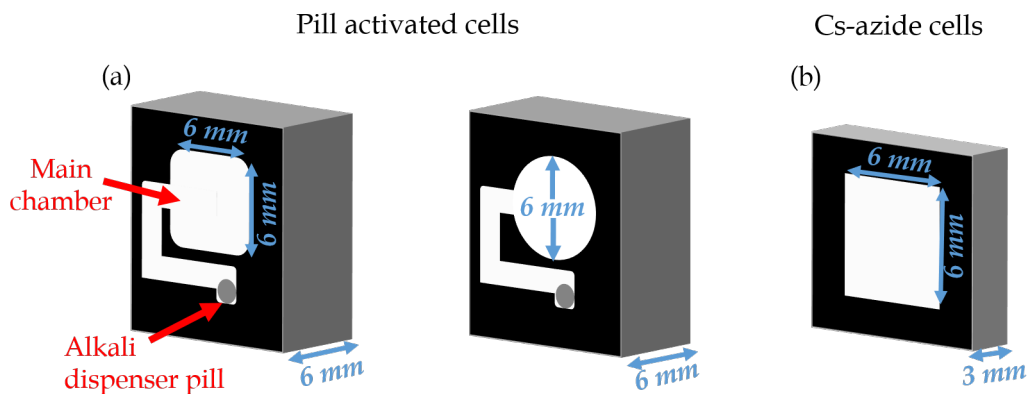
Figure 5.3: Illustrations of (a) the 6 mm thick cuboid and cylindrical cell geometries. Both cells contain an alkali dispenser pill which is separated via a connecting channel to the main chamber. The pill is irradiated as described in the text to activate the cell and then sequentially reduce the N_2 content. (b) 3 mm thick cell as described in Section 2.1. The buffer gas of these cells can not be reduced as they are produced using a Cs-azide deposition method.

The main purpose of examining an additional cell was to investigate the validity of the γ_{10} measurements for the cuboid cell, assessing the impact of cell geometry on the relaxation properties. As will be discussed, this difference in geometry had a negligible impact on the results, and served only to further solidify the experimental results of the cuboid cell.

5.1.2 Spectroscopy

A DBR laser (Thorlabs DBR895PN) tuned to the Cs D_1 transition at 895 nm was used to perform spectroscopic analysis using the setup illustrated in Fig. 2.5 (a). The design of the cells (Fig. 5.3 (a)) was such that the pill dispenser was positioned in the small, secondary chamber with the spectroscopy laser, aligned through the main chamber towards a photodiode (see Section 2.4.2 for details on probe intensity). This was employed in tandem with the high power laser facilitating a real-time approximation of reductions in N_2 to be observed through the optical spectra. The actual analysis of the N_2 content was performed post process. The DBR laser was driven via a low noise laser driver module (Koheron DRV300). The driver affords a temperature modulation via a TEC input. A function generator was used to provide this modulation via a 1 Hz scan across the pressure broadened D_1 line. Furthermore, a DAQ device (Picoscope model 5444D) captured data across the four photodiodes illustrated in Fig. 2.5 (a) at a scan rate of 1 Hz. This offered a sufficient temporal resolution for the continuous monitoring of reductions in N_2, allowing for the timely cessation of any additional getter action from the pill by deactivating the high-power laser. Incremental reductions in buffer gas pressure on the order of 10 Torr were pursued. In-situ monitoring of N_2 content was crucial for this controlled depletion process, with the N_2 pressure content measurable to within $\pm$ 2 Torr.

As described in Section 2.4.1, the ratio of the collisional broadening and shift provides a reasonable conclusion that inadvertent gas species are not present in the cell. If this ratio varies between measurement iterations (which was an area of intrigue for this study of iterative laser irradiation), then this indicates that other gas species may be impacting the measurements. However, the ratio was found to be consistent at 2.24 $\pm$

0.02 throughout the spectroscopic characterisation in this study. Spectroscopic studies, demonstrated in the work by Dyer et. al. [54], confirmed no imprint of buffer gas in the cell after full irradiation of the dispenser pill, ensuring the full removal of any residual buffer gas. Other methods to assess the contents of the cell could be to utilise a mass spectrometer to attempt to identify any additional elements present, however, this was not performed.

5.2   Intrinsic γ_{10} Relaxation Rates

This section describes the process of measuring the intrinsic relaxation rate, γ_{10}, as a function of buffer gas pressure for both cell geometries. Initially, the full process depicted in Fig. 5.2 was exhausted for the cuboid cell. After the extent of measurements for the cuboid cell were conducted, the cylindrical cell underwent the same process for a smaller number of measurements. The results are presented in the following sections.

5.2.1   Experimental Methodology

Figure 3.1 displays an illustration of the OPM experimental setup. To accurately measure γ_{10} as a function of N_2 pressure, care had to be taken to ensure that all other experimental parameters were consistent throughout. The magnetic field, generated using a bipolar $\pm$ 75 mA low noise current driver (see Section 3.3.2), and orientated along the z-axis was set to 1 μT. Any magnetic field gradients present from this bias field were calculated to contribute < 1 Hz to the relaxation rate.

The measurements were conducted at a cell temperature of 30 °C. Operating the vapour cell at a value slightly above room temperature avoided any external ambient temperature fluctuations impacting the experiment. Heating of the cell was carried out using two PCBs placed on adjacent sides of the cell. This enabled the ESP and resistive heating described in Chapter 4 to be performed in tandem. The magnetic (and heating) pulse was synchronised to that of the optical pumping pulse to ensure that no residual magnetic field was present when probing. As demonstrated in [32], any stray field leaking is on the order of the sensor noise floor, which is negligible compared to

the 1 μT bias field.

To monitor the temperature, three non-magnetic T-type thermocouple sensors were attached to separate ends of the cell. All agreed to within 0.1 °C, confirming a uniform temperature across the cell. The cell was also not found to drift by more than 0.1 °C over the course of each set of measurements. Nonetheless, any temperature fluctuations that may have occurred are not a considerable factor as γ_{10} does not significantly vary as a function of these, unlike γ_{20} (see inset of Fig. 5.1).

The pump and probe beams, both with an approximate $1/e^2$ beam diameter of 3.1 mm were aligned to overlap at the centre of the cell. Therefore, both laser beams were sufficiently well contained inside the cell volume to avoid beam clipping or reflections with glass surfaces. The pump frequency was set to the F = 3 to F' transition to expel atoms from the F = 3 level, minimising spin-exchange collisions and facilitating the extraction of γ_{10}.

The pump-probe cycle was applied at a repetition rate, f_d, of 10 Hz, providing a total time of 100 ms for one sequence. A peak pump power of 120 mW was applied for a pulse duration, T_{OP}, lasting 5 ms, to achieve the most extensive evacuation of F = 3 atoms. This resulted in a total probing duration, represented as T_{Pr}, of 95 ms. As the results will show, γ_{10} was measured to be approximately 140 Hz under these operating conditions. Consequently, a probe measurement time of 95 ms ensured ample duration for the atoms to completely decohere and re-thermalise between subsequent optical pumping cycles. For additional information regarding the characterisation and the rationale behind the selection of these laser powers and durations, please refer to Section 3.4.

5.2.2 Relaxation Rate Results

The initial N_2 pressure of the cuboid cell was 180 Torr when measured at 70 °C, corresponding to a pressure of 162 Torr when scaled to 30 °C. The lowest pressure and final measurement conducted for the cuboid cell for which any N_2 remained was 57 Torr. The probe frequency was $\approx$ 21 GHz blue-detuned from the F = 3 to F' transition. To obtain γ_{10} under these conditions, measurements were taken for a variety of probe

powers, at a maximum of around 1337 µW, in linearly decreasing steps until around 140 µW. This was measured before transmission through the cell where the typical transmission was ≥ 70 %. The FID signals were extracted and fit to using Eq. 3.3, as described in Section 3.2.1. The individual data-sets obtained from the FID fitting procedure for each probe power and buffer gas pressure are shown for the cuboid (a) and cylindrical (b) cells in Fig. 5.4.
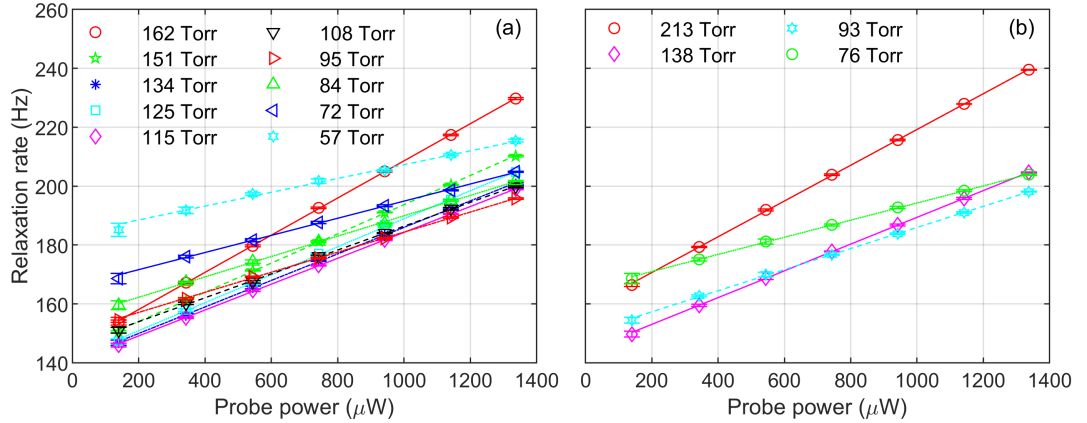
Figure 5.4: Probe power dependence on the measured relaxation rate for (a) the cuboid cell and (b) the cylindrical cell. The linear dependence validates the extrapolation to zero light power in order to determine the overall γ_{10} value. This eliminates power broadening and operationally induced decohering effects. The gradient of each data set is a result of the spin-polarisation generated and subsequent probe-atom interaction.

As displayed, the data exhibited a linear dependence which enabled a linear extrapolation to zero light power and subsequent inference of the γ_{10} value [71]. Employing a variety of probe powers essentially circumvented the effect of operational power broadening factors, caused by probe-atom interactions which elevate the relaxation rate. As the intensity of the probe is decreased there is less optical pumping by the probe. Due to the pressure broadened vapour cells, this is a linear process when under the saturation limit. Measurements for all pressures and cells produced small statistical errors for each data point on the order of 1 Hz.

The slope of each data set is a result of the spin-polarisation generated and the probe's interaction with the atoms. As the buffer gas reduces, the gradient also reduces.

The fixed probe frequency results in a comparatively larger detuning as the N_2 pressure is reduced, thus leading to lower interaction strengths. Stronger interactions at higher buffer gas pressures were evident based on the measured FID signal amplitudes at each data point. Due to the evolving process of iterative activation of the pill in order to perform these measurements, solid Cs droplets became visible on the glass surfaces. However, throughout the set of measurements, transmission of both laser beams remained above 70 %. Partial realignment of the beams through the cell was occasionally necessary, due to the unpredictable effect of pill irradiation and alkali release.
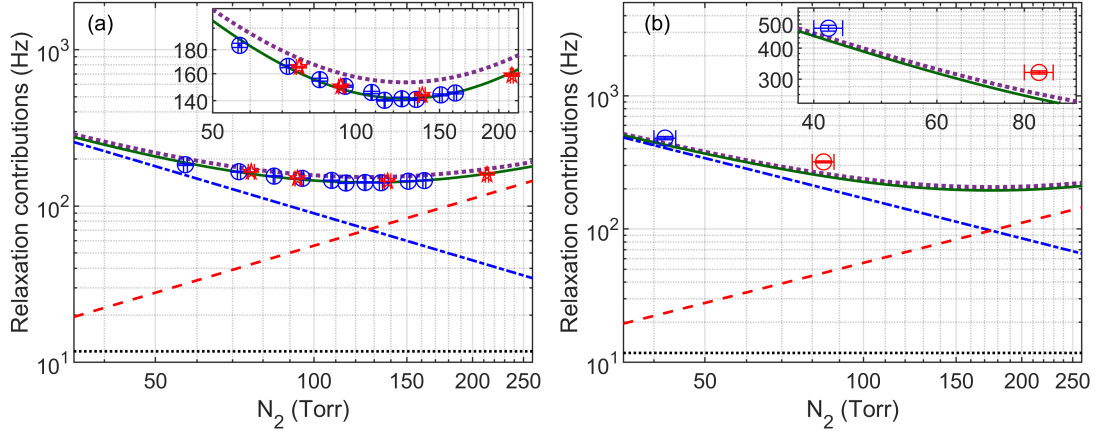
Figure 5.5: (a) Intrinsic relaxation rates (γ_{10}) as a function of N_2 pressure. Blue (red) data points relate to measurements using the cuboid (cylindrical) cell respectively. The y-axis error bars are generated from the error in linear extrapolation to zero light power in the data from Fig. 5.4. The x-axis error bars are statistical errors from measuring the N_2 pressure. The various lines relate to the theoretical spin-relaxation mechanisms outlined in Section 2.5: γ_{20} (purple dotted line), γ_{10} (green solid line), Cs-wall collisions (γ_{WC} blue dot-dashed line), Cs-N_2 collisions (γ_{BG} red dashed line) and Cs-Cs spin-exchange collisions (γ_{SE} black dotted line). (b) depicts the same theoretical contributions for a 3 mm thick cell together with experimental data for two separate cells containing different N_2 pressures.

Figure 5.5 (a) displays the overall γ_{10} data, found after extrapolating the data from Fig. 5.4 to zero light power, along with the various theoretical depolarising contributions described in Section 2.5. A negligible depolarising mechanism (< 0.1 Hz) arises from Cs-Cs spin destruction (γ_{SD}) collisions, thus, this has not been depicted in the

figure, although it has been incorporated in the overall model. Further data with the cylindrical cell was taken (red data points) to assess whether similar results were found with a different cell geometry. The data shows agreement in γ_{10} values between these two distinctive cell geometries. The comparative values at similar N_2 pressures enables the independent data sets to be collated and presented together due to the strikingly similar extractions of γ_{10} at similar N_2 pressures.

The theoretical model is heavily dependent on two parameters; the diffusion constant, $D_{0:Cs-N_2}$, of Cs in the N_2 buffer gas, and the total collisional spin-destruction cross section, σ_{Cs-N_2}, from Cs-N_2 collisions. Values relating to these which have been published in the literature are shown in Table 5.1, highlighting the discrepancy between authors. The size of the investigated cell (both radius and thickness) also has an impact on these (i.e. a comparatively larger value for σ_{Cs-N_2} is found for larger cells).

$D_{0:Cs-N_2}$ (cm^{2}s^{-1})	σ_{Cs-N_2} (10^{-26} m^2)	Cell r & t (cm)	Ref
0.11	3.3	0.3, 0.6	This work
0.073 ± 0.015	5.52 ± 0.44	2.75, 7.5	[111]
0.22	0.47	Pyrex bulb	[112]
0.098 ± 0.01	5.52 ± 0.55	3.45, 7.4	[113]
0.12	30	0.95, 0.1	[114]

Table 5.1: $D_{0:Cs-N_2}$ is in units of cm^{2}s^{-1} and Cs-σ_{Cs-N_2} is in units of m^2 (10^{-26}) as amassed from various sources employing cells of different radii (r) and thicknesses (t). The table highlights the discrepancy in measured values, particularly with respect to σ_{Cs-N_2}.

Across the buffer gas pressure range, the values for the model that match the γ_{10} data points in Fig. 5.5 (a) are: $D_{0:Cs-N_2} = 0.11$ cm^{2}s^{-1} and $\sigma_{Cs-N_2} = 3.3$ x 10^{-26} m^2. This value for $D_{0:Cs-N_2}$ matches well within the range of published values. σ_{Cs-N_2} falls within a fairly wide spectrum of published data. More recent data for these parameters are not readily available. The disparity of measured values from the literature makes it reasonable to incorporate these values in the model which aligns well with the observed data. This alignment is further supported by the reliability of the measurements in this work, involving multiple data points with two distinct cells.

The data demonstrates a reduction in γ_{10} when lowering the N_2 pressure from

212 Torr to 115 Torr, which is where it is minimised. γ_{10} begins to increase as the N_2 is reduced further, inferring that from here the Cs-wall collisions (γ_{WC}) become the dominant depolarising mechanism and the contribution from Cs-N_2 collisions (γ_{BG}) diminishes. Across a range of approximately 150 Torr (from ≈ 212 to 57 Torr), γ_{10} varies from ≈ 140 to 184 Hz. This equates to intrinsic spin-coherence times of between 5.4 and 7.1 ms. Moreover, γ_{10} maintains a consistency of 140 to 145 Hz between a range of 110 to 160 Torr, showcasing a fairly wide pressure range that permits excellent coherence times. This is a significant time period in which magnetic sensing measurements can be made before spin-relaxation occurs.

Data was also taken at room temperature, without heating the cell or applying $\vec{B}_{Pol}$ to ensure that its influence did not impact the signal. This was effectively verified by retrieving a relaxation rate of 139 Hz at a N_2 pressure of 125 Torr. Notably, this value is 2 Hz lower than the 141 Hz obtained when the cell was heated to 30 °C, aligning with the theoretical expectation of $\Delta\gamma_{10}$.

5.2.3 Caesium Azide Cell Results

In addition, supplementary experiments were conducted using cells resembling the dimensions used in much of this thesis i.e. 3 x 6 x 6 mm, including in Chapters 4 and 6. These were fabricated by KNT, and related to the Cs-azide fabrication method described in Section 2.1. A sketch of these is provided in Fig. 5.3 (b). Two distinct cells containing different buffer gas pressures were employed. The N_2 buffer gas content of cells produced via this method of fabrication cannot be tailored after the wafer-bond has been hermetically sealed. The same duration of optical pumping and probing was employed. An identical filtering and fitting procedure was also exercised. Sequential measurements were taken under the same experimental conditions as those described for the 6 mm cells, with linearly decreasing probe powers, and an extrapolation to zero light power for extraction of γ_{10}. Figure 5.5 (b) displays the extracted γ_{10} for these (displayed using respective blue and red data points) along with the various theoretical depolarising contributions using the same values of $D_{0:Cs-N_2}$ and σ_{Cs-N_2}.

From the data it is clear that values above the theoretical model were determined.

However, a full analysis across the same buffer gas range was not possible due to a limitation of available Cs-azide cells with corresponding pressures. Measuring reliable spin-relaxation rates of cells which are limited to smaller cell dimensions can be challenging. Other works utilising OPMs to extract relaxation rates for cells with smaller dimensions, i.e. with either cell thickness, t, i.e t = 4 mm in [71] or radius, r, i.e. r $\approx$ 1 mm in [40] have also found slight deviations from the model. A full characterisation across a larger buffer gas range would illuminate this issue more clearly.

5.2.4   Discussion

Originally, a more extensive range of pressures for the 6 mm pill-activated cells was desired. This was not possible due to a lack of availability of cells containing higher N_2 content after the initial activation i.e. when the N_2 was at its maximum. Additionally, there was difficulty in precisely controlling the N_2 depletion throughout the pressure range. Specifically, too much N_2 was depleted resulting in a gap in data between 57 to 0 Torr. This unintentional loss of the N_2 content was a result of excessive energy transfer during the laser reactivation of the pill. There was data taken at < 1 Torr, however, such little N_2 content made any pressure reading using the existing setup non-resolvable, therefore the exact pressure was unknown. The relaxation rate for this measurement was around 200 kHz which is orders of magnitude above those containing N_2, due to the ballistic motion of atoms colliding with the cell walls, and a large degree of radiation trapping. This is an effect also observed in [40], in which a determination of the relaxation rate for a Rb vapour cell with approximately 3.8 Torr of N_2 was found to be 38 kHz.

It should be noted that the γ_{10} values, and the N_2 pressure that minimises this can only be stated to be the case for the conditions in which this experiment was operated, i.e. at 30 °C and at a low magnetic field of 1 µT. At raised cell temperatures and field strengths, spin-exchange collisions are not completely minimised; instead, they are merely reduced. This effect is presented in Sections 5.3 and 5.4.3.

Overall, the data showcased an initial reduction in γ_{10}, enabling the minimal point to be determined. This demonstrates a successful application of buffer gas pressure

tuning to obtain the optimal value for two geometrically differing 6 mm thick MEMS cells. Of significant note are two key points. The first is that these results indicate that the differing geometry of the 6 mm cells does not markedly impact the cell performance characteristics. This is an encouraging result which bodes well for mass cell fabrication as this indicates a level of consistency between cells. A second and even more noteworthy finding is the large buffer gas pressure range at which prolonged relaxation times are found.

5.3   Spin Exchange Suppression

As stated in Chapter 4, the ESP technique is a far more practical approach to the future of geomagnetic field sensing using a FID magnetometer. Combining this with larger mass producible MEMS cells could yield high sensitivities, yet also retain a small footprint and overall package size. Nonetheless, due to the previously mentioned NLZS effect, and potential magnetic gradients, a slight degradation in the spin-polarisation is found when under the presence of heightened bias field strengths such as the Earth's. The impact of the reduced signal amplitudes and γ_2 rates as a function of magnetic field strength and cell temperature are displayed in Fig. 5.6.

Although an increased magnetic field results in both a lower signal amplitude and increased γ_2 rate, the effect of increasing the temperature is more significant. An elevated vapour density can improve the magnetic sensitivity, however, the heightened spin-exchange collision rate ultimately increases the overall relaxation rate. This can be suppressed to some extent as demonstrated in the previous sections, through operating at low cell temperatures and magnetic fields and evacuating atoms from F = 3.
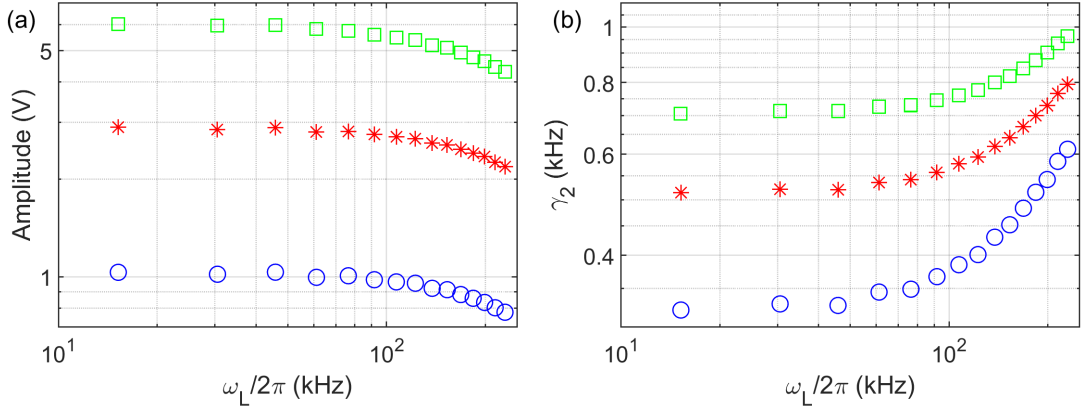
Figure 5.6: Effect of the magnetic field strength on the signal amplitude (a) and γ_2 (b) for a 6 mm thick cell operated at various temperatures. Spin-relaxation increases as a function of temperature and bias magnetic field strength. Blue, red and green datasets relate to T = 45 °C, 55 °C and 60 °C respectively. Statistical errors are smaller than the markers. Respective pump and probe powers of 125 mW and 1.13 mW were employed.

Evidence of this suppression is demonstrated in Fig. 5.7 (a) where the optical pumping frequency was set to compare pumping on F = 4 with that of F = 3 at select buffer gas pressures using the cuboid 6 mm cell at T = 30 °C. A heightened relaxation rate is observed when pumping on F = 4 compared to the more favourable F = 3. As described in Section 2.4.4 there is a closer parity to which ground state the atoms occupy when pumping on F = 4. The atomic populations become distributed across both hyperfine levels to a far greater extent. This is supported by an increase in the measured γ_{20} values across the N_2 range with an approximate 20 Hz increase observed. An increase of only 11 Hz is expected due to γ_{SE} under these conditions. This approximate two-fold increase is due to the inaccuracy of using a single sinusoidal model when pumping on F = 4. However, the model remains valid for F = 3 pumping.

Further measurements showcasing the suppression of spin-exchange collisions as a function of cell temperature are displayed in Fig. 5.7 (b). These were performed using 120 mW of pump light and 400 µW of probe light under the same applied magnetic field of 1 µT for $N_2 \approx 162$ Torr. However, no extrapolation to zero light power was performed, leading to an overall measurement of γ_2, instead of γ_{20}. The increased γ_2 rates for higher temperatures when pumping on F = 4 is evidence of increased spin-

exchange collisions as described in the previous paragraphs. It can be seen however, that pumping on F = 3 does not fully prevent spin-exchange collisions, as these strongly increase with temperature.
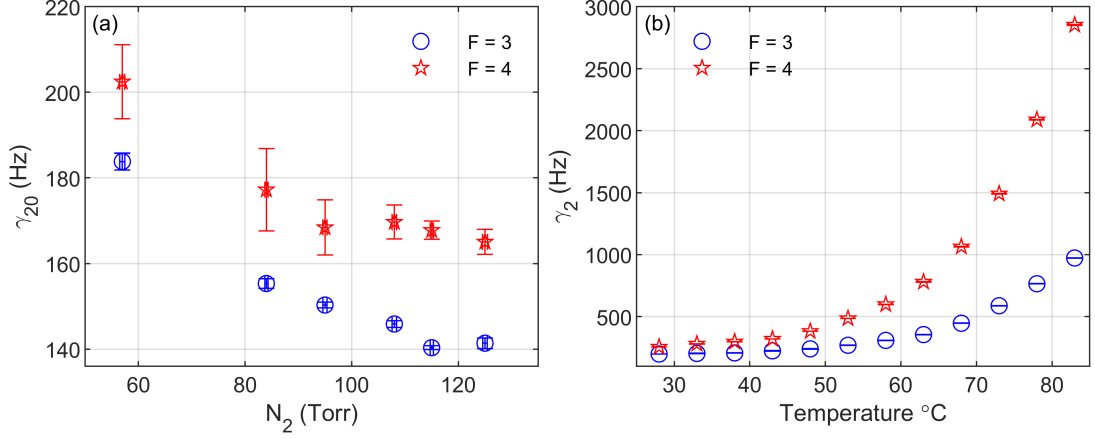
Figure 5.7: (a) γ_{20} for select buffer gas pressures under the same experimental conditions described in Section 5.2. The legend in both figures describes pumping on F = 3 (blue) compared to F = 4 (red). A heightened relaxation rate is measured when pumping on F = 4 (where $\gamma_{20} = \gamma_{10} + \gamma_{SE}$) compared to F = 3 (where $\gamma_{SE} = 0$). (b) Spin-exchange suppression as a function of cell temperature. At the lower cell temperatures the increased relaxation rate for F = 4 pumping is primarily caused by power broadening effects due to the probe frequency being closer to F = 3.

An initial γ_2 offset of 57 Hz at low temperatures was found when pumping on F = 4. Again, this is higher than the expected intrinsic 11 Hz offset caused by γ_{SE}. The discrepancy of 46 Hz is ascribable to power broadening effects caused by probing closer to the F = 3 hyperfine level, where many of the atoms occupy when pumping on this transition (see also Fig. 4.10), along with the single sinusoidal model inaccuracy. Operating with 400 µW of probe power also induces an increase in the relaxation rate of around 55 Hz at T $\approx$ 30 °C when pumping on F = 3 compared to the data from Fig. 5.5 (a).

5.4 Sensitivity Performance

5.4.1 Experimental Methodology

Assessment of the achievable sensitivity performance of the sensor required raising of the vapour density. Therefore, the cell was heated to 70 °C for each N_2 pressure iteration. Demonstrating the system's candidacy for unshielded applications required increasing the bias field, $|\vec{B_z}|$, to 50 µT. This field was generated using a 12 V battery connected to a resistor in series. The battery provides low noise current, minimising additional magnetic noise added to the system, which is essential for optimal lab-based operation. Consistent pump and probe powers of 120 mW and 1200 µW were respectively employed throughout. The repetition rate, f_d, was set to 500 Hz with an optical pumping duty cycle of 10 %. This equates to an optical pumping period of 0.2 ms and a 1.8 ms probe duration during each FID cycle. The higher repetition rate applied here aids the sensitivity performance, which can be optimised based on the decoherence rate and the CRLB condition. In contrast to Section 5.2, this commences subsequent optical pumping cycles before the atoms have fully decohered or re-thermalised.

Owing to the variations in buffer gas pressure, adjustments were made to fine-tune the probe frequency detuning for each measurement. Specifically, at the highest N_2 pressure, a relative probe detuning approximately 10 GHz lower than that used at the lowest pressure was needed. To accommodate the limitations of the detection polarimeter, the probe frequency was set to attain a FID signal amplitude between 9 and 10 V. This ensured that the full signal could be directly captured by the detector and avoided saturation.

5.4.2 Sensitivity Results

Each assessment of the magnetic sensitivity involves capturing a signal train of data. Consecutive FID cycles were captured over 40 independent 1 s time periods using Welch's method. Figure 5.8 displays the sensitivity results across the full buffer gas range for the cuboid and cylindrical cells. For the cuboid cell, the experimental sensitivities slightly degraded as a function of reduced buffer gas pressure. Nevertheless,

over the full buffer gas range a consistent performance was found with measured experimental sensitivities between 130 to 155 fT/$\sqrt{\text{Hz}}$. The highest sensitivity of 130 $\pm$ 11 fT/$\sqrt{\text{Hz}}$ was found to occur at a buffer gas pressure of 180 Torr. Sensitivities below 150 fT/$\sqrt{\text{Hz}}$ are easily attainable in these 6 mm cells using the experimental construction described in this thesis, across a fairly large range of cell temperatures, pump and probe powers, probe frequencies and also N_2 pressures.
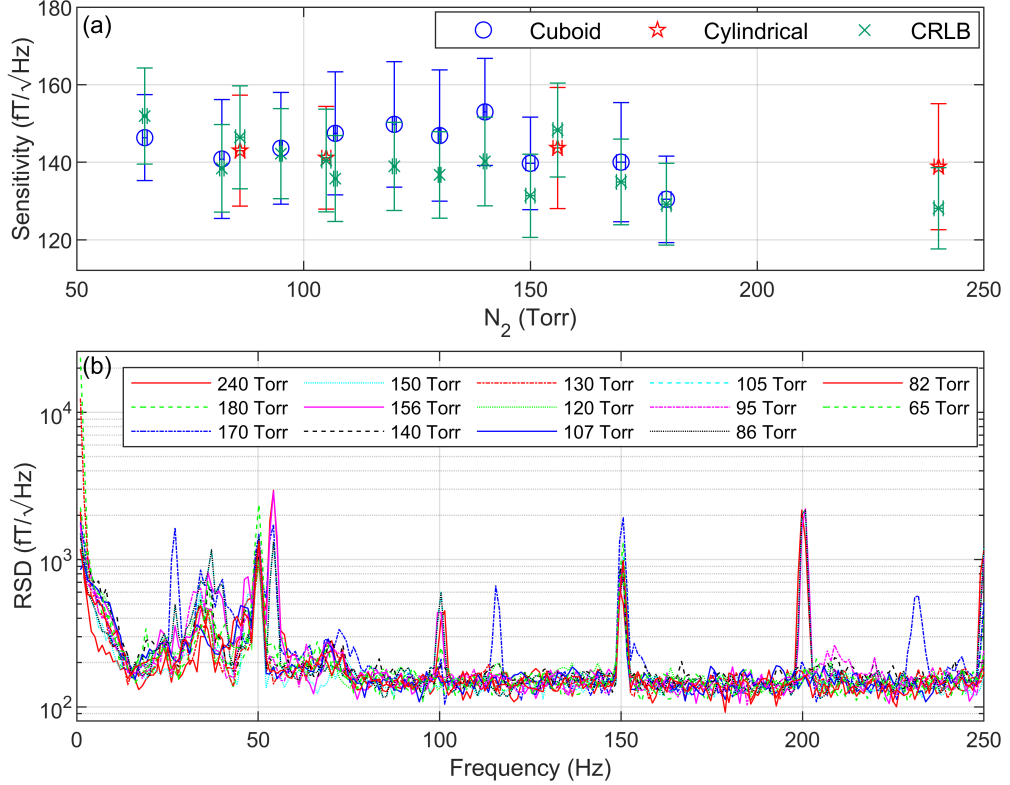
Figure 5.8: Sensitivity performance as a function of buffer gas pressure. (a) Experimental sensitivities for the cuboid and cylindrical cells, displayed in blue and red respectively. The associated CRLB is in green. (b) The respective RSD data relating to each N_2 measurement, highlighting the generally flat noise floor despite prominent peaks and variation in the external magnetic environment.

The noise densities calculated from the equations described in Section 3.2.3 are also displayed. The CRLB for each matched the experimental sensitivities, reiterating that $\vec{B}_{\text{Pol}}$ was sufficiently demagnetised. The external magnetic environment, however, varies which is evident from fluctuating amplitudes in the RSDs. Sensitivity improvements

103

across the full bandwidth range i.e. over the line noise peaks would likely be found by implementing additional layers of magnetic shielding.

The buffer gas pressure under these conditions which resulted in the lowest γ_2 value occurred at 180 Torr. Interestingly, the extracted relaxation rates for these measurements do not corroborate with where the minimum relaxation rate occurred in Section 5.2. There, the N_2 pressure that minimised γ_{10} occurred at 115 Torr, which translates to around 130 Torr at 70 °C. This disagreement is a result of the higher bias field and temperature causing different spin-decoherence dynamics, which is discussed in the next section.

5.4.3   Identifying the Decoherence

An additional investigation to quantify the distinct depolarising contributions attributed to the increased bias field and the elevated operating temperature was conducted. This was undertaken in conditions matching those discussed throughout this section i.e. at 70 °C, with the same pump and probe durations and peak powers employed. By maintaining a consistent temperature and performing measurements at both a 1 µT and 50 µT field, the individual decohering impacts of relaxation due to increased cell temperature and increased field can be determined. A linear extrapolation to zero light power was performed using the cylindrical cell at an approximate N_2 pressure of 85 Torr. A single FID trace relating to a 1337 µW probe power for both the low and high field is displayed in Fig. 5.9 (a) and (b). The extracted γ_2 and amplitude results are displayed in Fig. 5.9 (c) and (d).
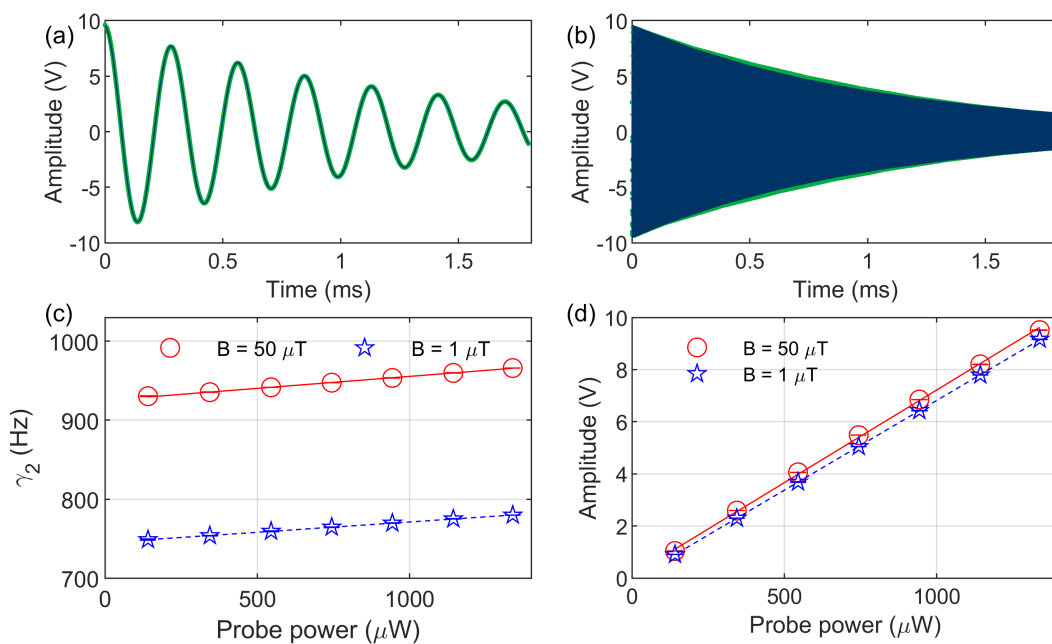
Figure 5.9: FID trace at 1 µT (a) and 50 µT (b) bias fields at a cell temperature of 70 °C. γ_2 (c) and signal amplitude (d) values for both field strengths, with corresponding linear fits. The probe beam was 2.5 GHz further blue-detuned when operating at 1 µT to avoid saturating the detector.

The intercepts indicating the γ_2 values are 750 and 925 Hz for the low and high field respectively, confirming a much larger contribution to spin-exchange is caused by the elevated cell temperature. The contribution arising from the increased bias field strength is 175 Hz (925-750 Hz). The expected gradient, γ_{Grad}, across the cell using this coil apparatus is approximately 32 Hz ($\Delta B = 9$ nT).

5.4.4 Sensitivity Discussion

A separate pursuit of realising the highest experimental precision possible using a 6 mm thick cell produced a sensitivity of 118 ± 11 fT/$\sqrt{\text{Hz}}$. This was also calculated over 40 independent 1 s periods, and was found at a cell temperature of 65 °C at a pressure of $N_2 = 180$ Torr. This lower operating temperature which translates to lower power consumption is advantageous. Due to the similarity in the sensitivity trend from Fig. 5.8 it is probable that this performance is achievable across the full buffer gas range. A single FID trace along with the RSD is displayed in Fig. 5.10. Notably, line and

technical noise peaks are observable, indicating coupling through the electronics and magnetic environment. Variations in the amplitude and frequencies of these peaks are also evident in Fig. 5.8.
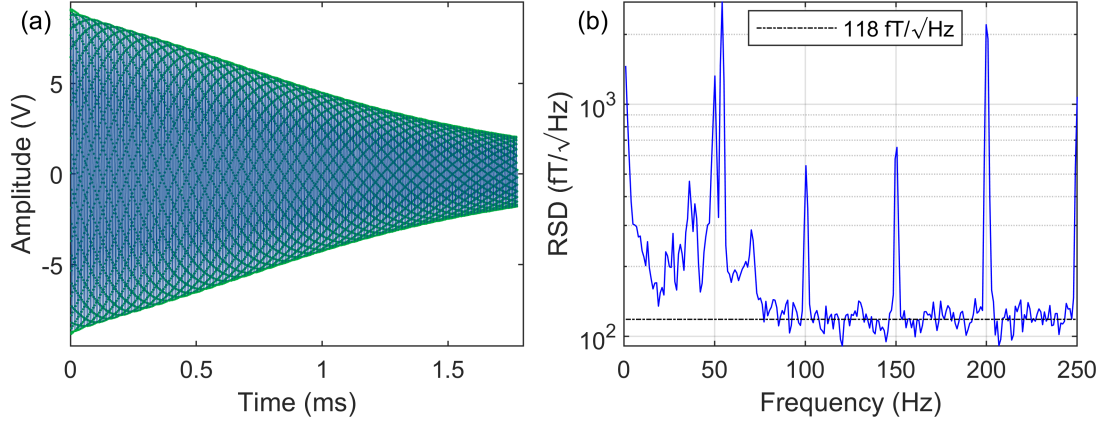
Figure 5.10: (a) FID cycle for $N_2 = 180$ Torr at 70 °C and a 50 µT bias field. Data is displayed by green markers whereas the fit is in blue (b) Magnetic sensitivity spectrum (blue) which is a result of 40 consecutive and distinctive 1 s datasets. The dashed black line provides an indication of the magnetic sensitivity which is relatively flat outside the regions with line and technical noise peaks.

This result equates to 2-3 ppb in fractional sensitivity terms (118 fT/ 50 µT). To the authors knowledge, this represents the highest fractional sensitivity achieved experimentally using a MEMS OPM device. This compares favourably to [115] in which a higher sensitivity of ≈ 21 fT/$\sqrt{\text{Hz}}$ was demonstrated, albeit at a lower field of 2.5 µT, leading to a fractional sensitivity of around 9 ppb. These findings owe much to the quality of the vapour cell, which is a crucial component in any total field OPM scheme. Additionally, the constructed dual-beam configuration combined with the ESP technique greatly assists in maintaining the spin-polarisation during the atomic state preparation. MEMS cells have previously shown higher sensitivities than the work here, however, also at lower magnetic fields i.e. in [28]. In that work, magnetic field nulling was used during the optical pumping stage, ultimately producing a sensitivity of around 100 fT/$\sqrt{\text{Hz}}$. While demonstrating excellent sensitivity, the advantage of the ESP approach used in this work is that it circumvents the need for measuring the field and subsequently nulling it. This presents an advantage for unshielded sensing

as it reduces dead-time and bypasses potential issues incurred in dynamic magnetic environments i.e. sensing on board moving vehicles or vessels.

Sensitivities at these levels validate the fabrication and activation approach employed for these cells. Additionally, this study has demonstrated the large buffer gas pressure range at which exemplary sensor performance is attainable. The data also suggests that mass fabrication of cells with higher pressures can be produced which will also yield excellent results. One of the main advantages of the buffer gas tuning approach is the ability to decrease the pressure post fabrication. Magnetic gradiometers would undoubtedly benefit from this, as the capacity to finely adjust the pressure to be equal for identical cell geometries is desirable [116, 117]. Furthermore, this alkali and buffer gas sourcing approach avoids the use of hazardous Cs-azide.

Chapter 6

Magnetic Image Reconstruction

This chapter explores the utilisation of the sensor for magnetic imaging applications. Imaging using measurements of a magnetic field can provide effective mapping of an object with high precision and accuracy. This capability is valuable for scanning large areas, such as those encountered in human exploration of new territories. The inclusion of MEMS cells proves more practical in smaller-scale environments, enabling the identification of defects in electronic circuits or batteries.

The FID sensor is an ideal candidate for imaging applications as it has the dynamic range and sensitivity, in conjunction with a high and adjustable bandwidth. The sensor is scalable, therefore, conducive for deploying a modular sensor in production-line settings. For example, PCB inspection or diagnostics of batteries could be performed with high sensitivities in potentially unshielded environments, with immediate practicality and cost benefits.

Other devices, such as nitrogen vacancy (NV) diamond sensors, demonstrate exemplary spatial resolution at the nanoscale; however, they do not achieve sensitivities equivalent to or competitive with OPMs [118, 119]. Alternative OPMs, such as the SERF sensor do demonstrate excellent sensitivities, however magnetic shielding and extensive magnetic field nulling is required due to the limited dynamic range. Additionally, the bandwidth and thus potential signals of interest are limited due to the extended spin-coherence times during SERF operation. RF sensors also have excellent sensitivity and a tuneable detection frequency which enables magnetic sensitivities to be

obtained away from prominent magnetic noise or technical 1/f noise sources. Similarly to SERF sensors, however, the dynamic range of these are limited which means that either active or passive (or both) shielding is required, again impacting their viability in real-world unshielded imaging.

6.1 Experimental Configuration

A modification to the experimental setup detailed in Section 3.1 was applied. A 3 mm thick MEMS vapour cell featuring internal dimensions of 6 x 6 x 3 mm^3 was employed as the sensor head. This cell contained 220 Torr N_2 buffer gas, resulting in a collisionally broadened linewidth (FWHM) of 4.3 GHz. The ESP technique (detailed in Chapter 4) was utilised to resistively heat the cell to a temperature of 88 °C, and generate a strong magnetic field $\vec{B}_{Pol}$ along the beam propagation axis (x), bolstering the signal. This elevated vapour density was found to maximise the sensitivity.
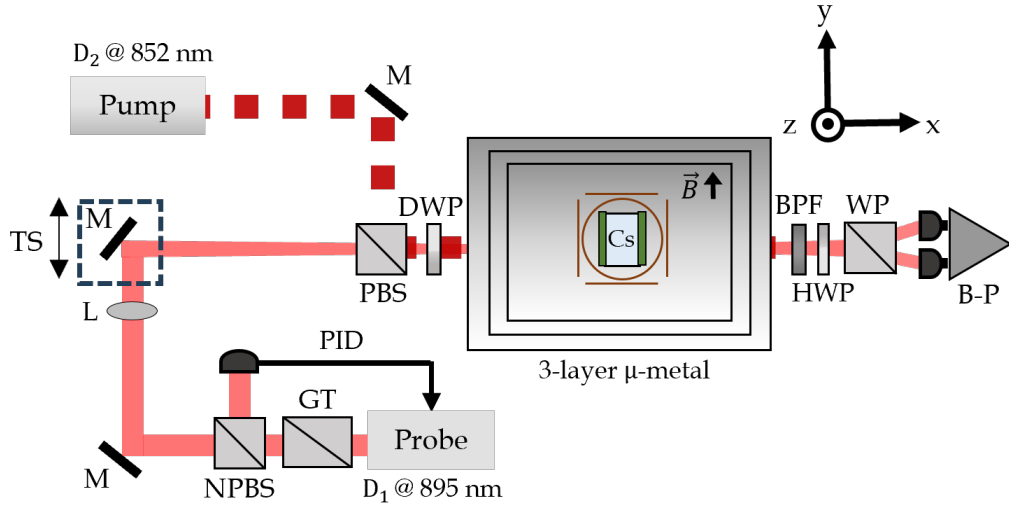
Figure 6.1: Simplified experimental schematic used for magnetic imaging. A slight modification to the setup described in Section 3.1 was to incorporate a focusing lens in order to reduce the probe beam size to 175 μm, measured at the position of the vapour cell. A mirror, mounted on a translation stage (TS) permitted adjustment to the horizontal position of the beam along the y-axis. Vertical adjustments along the z-axis were also performed through tilting of this mirror.

A schematic of the experimental setup is provided in Fig. 6.1. The repetition rate f_d

of the device was set to 1 kHz, producing a Nyquist limited bandwidth of 500 Hz. A peak pump power of 65 mW, tuned to the F = 3 to F' transition was employed for a duration of 110 µs before being switched off during the probing stage. The extinction ratio of the AOM (> 20000:1) reduces any residual optical pump light during the off-period to < 3 µW. Additionally, after the pump light exits the optical fibre, a Keplerian telescope configuration expands the beam diameter to 4.5 mm ($1/e^2$), increasing the effective interrogation area within the cell and improving the imaging coverage. The pump beam was aligned to a fixed position at the centre of the cell to maximise optical pumping, and to avoid beam clipping. The waist of the probe beam constrains the OPMs spatial resolution and, therefore, the potential image quality. To enhance this resolution, the probe beam was focused to a reduced $1/e^2$ beam diameter of 175 µm.
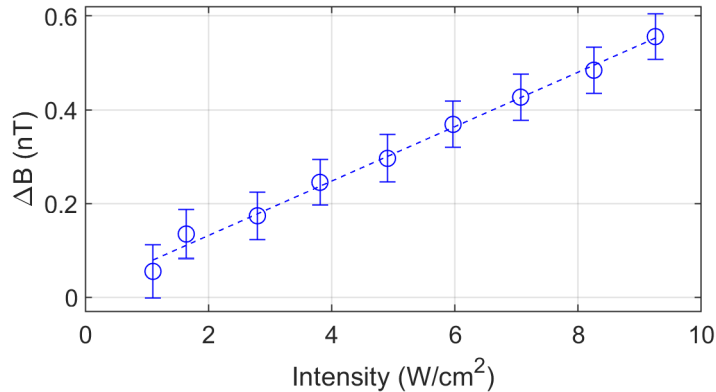
Figure 6.2: Extracted deviation in measured magnetic field as a function of probe intensity. Δ_B was calculated after extracting ω_L from the FID signal data for a variety of probe powers which were converted to probe intensity. A Stark shift of around 0.5 nT was found when employing a probe intensity of ≈ 9.25 W/cm^2, corresponding to the 1.12 mW of optical power used.

The Rayleigh length [120], (given by $Z_R = \frac{\pi w_0^2}{\lambda} = 2.7$ cm) exceeds the cell thickness by an order of magnitude, rendering intensity gradients along the beam propagation axis insignificant. A probe power of 1.12 mW was employed, thereby elevating the optical intensity and ensuring ample light-atom interaction, which in turn maximised the sensitivity performance. To account for the heightened intensity, the probe beam was set 60 GHz blue-detuned from the F = 4 to F' transition, reducing excessive

broadening of the magnetic resonance from residual optical pumping. The considerable detuning aids in reducing light shift systematics, which were determined to contribute 0.5 pT/µW to the measured Larmor frequency. This was calculated through obtaining FID data across a range of probe powers and extrapolating to zero light power as displayed in Fig. 6.2.

The probe beam's position along the y-axis of the cell was adjusted through the use of a mirror mounted on a translation stage with 0.25 mm resolution. The stationary MEMS cell could be successfully imaged along this axis through translation of the reflected probe beam. Vertical adjustments along the z-axis were performed by tilting this mirror.
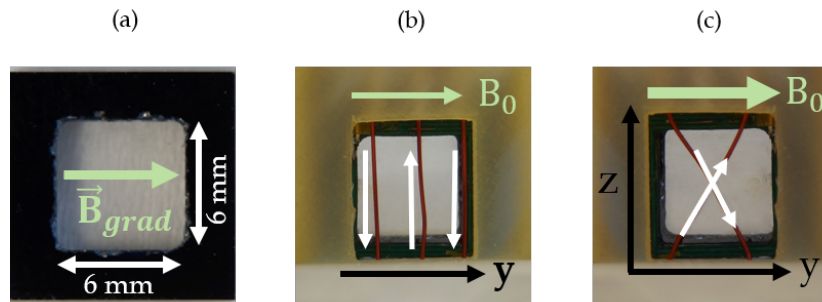
Figure 6.3: Arrangements for generating field distributions for magnetic re-imaging. (a) A first order magnetic gradient is applied along the y-axis via a single turn anti-Helmholtz coil pair. (b) A copper wire was used as the field imaging source in a 's' configuration, enabling 1D mapping along y. (c) A cross-wire arrangement facilitated a 2D image reconstruction both spatially and temporally for $\vec{B}_y \approx 50$ µT .

The spatial resolution is ultimately limited by the diffraction limit, which sets a lower bound on the beam waist size. Nonetheless, the impact of spin diffusion, which is contingent on the N_2 pressure in the cell should also come into consideration. A buffer gas vapour cell can be considered as an array of locally independent sensors, each with a size determined by the distance travelled by the atoms during the measurement. This is referred to as the crosstalk-free distance, and is estimated by $\Delta x = \sqrt{2DT}$, with D representing the diffusion constant of Cs in a cell containing N_2 at a particular pressure and temperature, and T is the total spin-coherence time [121, 122]. This results in a value of $\Delta x \approx 200$ µm for this configuration which closely resembles the probe beam

diameter size. Δx can be reduced by increasing the buffer gas pressure of the cell or reducing the operating temperature, to the detriment of sensitivity.

Three distinct magnetic field distributions emanating from different applied sources were investigated. More specifically; 1) applying a distinct magnetic gradient across the cell, 2) placing a copper wire in an 's' structure and characterising the distribution from this across the y-axis, and 3) adapting the shape of the wire to a cross configuration, permitting a 2D translation across the y and z axes against in a 50 µT bias field. In this final arrangement, the sensor was also able to temporally characterise the vapour cell, through demodulating an oscillating AC signal, in conjunction with passing a DC current through the wire. The results from these three field sources are presented in the following sections.

6.2   Magnetic Gradient

An initial calibration, conducted to gauge the sensors ability to differentiate between a varying magnetic field distribution across the cell was performed. A well-defined first order magnetic field gradient, produced using a single turn counter-wound anti-Helmholtz coil pair with radius R = 16 mm and a separation distance of s = 19.7 mm, was applied along the y-axis. Varied currents between $\pm$ 2.5 mA were applied to this coil in order to demonstrate the effect of these different gradient strengths and directions on the OPMs measured field. A constant bias field of $\vec{B_0}$ = 0.95 µT was also applied along the y-axis Helmholtz coil pair. The probe beam's position was initially centered vertically using the mirror. Following this, it was horizontally translated along the y-axis. A 1 s FID signal train was captured, providing an average magnetic field at each position.

Figure 6.4 (a) displays the field distribution for two applied gradients in opposing directions. A non-uniform magnetic field distribution was observed using this $\vec{B_0}$ coil assembly as evident from the data (black). A second-order gradient dependence was observed when no current was applied along the gradient coil i.e. for the sensor background. Nevertheless, each applied gradient can be verified through subtracting this

112

background measurement from each probe beam position, as shown in (b).
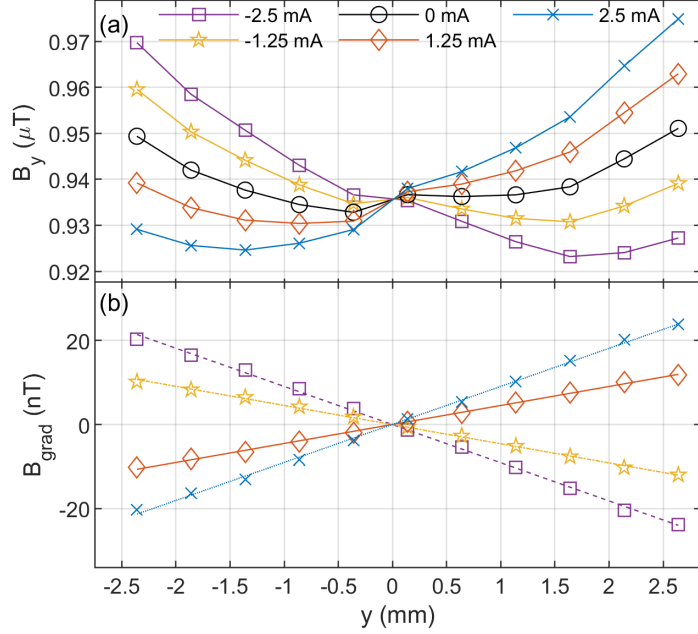
Figure 6.4: (a) Measured field distribution after a first-order magnetic field gradient is applied along the y-axis at various coil supply currents. Data points in black circles denote the background OPM reading with no current applied. The solid lines are used to guide the eye. (b) Measured field gradients and respective linear fits for the associated supply currents after sensor background subtraction. All data points relate to 1 s of FID data providing a negligible statistical uncertainty with error bars smaller than the markers.

The background field variation can originate from unintentional gradients produced along the bias field, and from inhomogeneous optical pumping effects. The pump beam exhibits both a Gaussian intensity profile and a finite beam waist, leading to differences in the degree of spin-polarisation generated, depending on the position within the cell. Although the expanded pump beam size encapsulates a larger area within the cell, a reduction in signal amplitude is observed at the edges due to the lower intensity. This confirms that the distribution of atomic population across both hyperfine ground states varies depending on the position within the cell. The measurement of the Larmor frequency is therefore weighted by these populations, due to the ground states possessing slightly differing Landé g_F factors (see Section 2.3.1), giving rise to a source of heading error.

113

Nonetheless, the influence of the applied gradient is apparent. The majority of the overall field measured by the OPM stems from $\vec{B_0}$, however the impact of the applied gradient is observed in the data. The extracted magnetic field value at each position can be compared to the theoretical expectation of the overall field strength, calculated at a position, y, from the midpoint between two parallel and identical plane coils with current flowing in opposing directions. This yields the predicted gradient field distribution, given through the following analytical expression,

$$\text{B(y)} \approx \frac{\mu_0 \text{NIR}^2}{2} \left([\text{R}^2 + (\text{y} - \text{s}/2)^2]^{-3/2} - [\text{R}^2 + (\text{y} + \text{s}/2)^2]^{-3/2} \right), \qquad (6.1)$$

where μ_0 is the magnetic permeability, N, is the number of coil turns, I, is the applied current, R, is the coil radius and, s, is the coil separation distance. A linear relationship between the field measured and the probe beam's position was observed as expected. The data in Fig. 6.4 (b) correlates well with the theoretical estimate, with the values agreeing to within 7%. This consolidates the OPMs ability to distinguish different spatial field distributions as expected. The minor difference between data and theory stems from slight inaccuracies in the theoretical calculations, which are highly sensitive to any distortions in the coil geometry. This is confirmed by comparing the ratio between each experimental and theoretical gradient which are 0.934, 0.931, 0.943 and 0.937 (in ascending current order), agreeing to within $\pm$ 0.6% of each other.

6.3   1D Image Mapping

A more complex field distribution was produced along the y axis through positioning a copper wire (32 AWG) approximately 4.5 mm from the cell, as illustrated in Fig. 6.3 (b). The wire comprises three adjacent segments, each separated by approximately 2.75 mm, strategically placed at the exit face of the cell to ensure unobstructed light-atom interaction. Alternating current flows are generated, providing a localised magnetic field source and enabling a mapping of the distribution as the probe beam is translated across the cell. Similarly to the magnetic gradient calibration, the bias field along y was set to $|\vec{B_0}| \approx 0.95$ µT. The data is presented in Fig. 6.5 relating to a variety of

currents passed through the wire ranging between ± 4 mA. The vertical dashed lines indicate the position of the wires, where data collection was not possible due to the hindrance of laser light reaching the polarimeter.
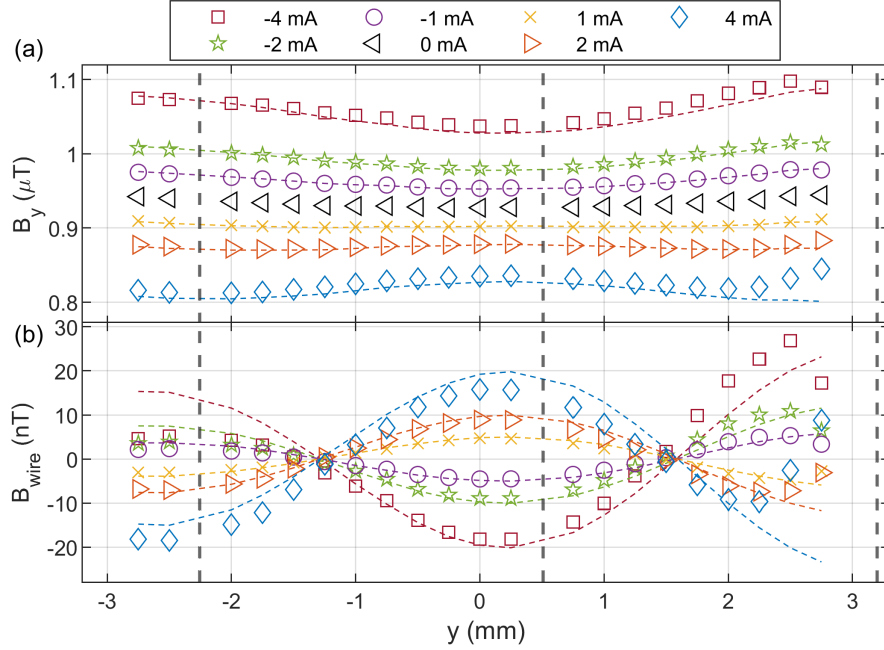
Figure 6.5: (a) Magnetic field mapping in 1D using the configuration illustrated in Fig. 6.3 (b). No current applied is denoted by black markers. The data from each supply current is compared to the theoretical expectation using Eq. 6.2. (b) Magnetic field distribution after the background and mean values for each respective supply current are subtracted. Deformations in the wire segments result in slight asymmetries and disagreement with the theory. An adjacent fourth wire on the right side (not pictured) also interferes with the data.

The background field, measured at 0 mA (black data points) across the cell closely resembles the second order gradient dependence discussed in Section 6.2. Applying positive current flow results in the field from the two outer wires adding constructively to B_0, while the central wire opposes this. Furthermore, the total measured field is increased due to the outer wire segments dominating. Reversing the current flow direction inverts this field distribution as expected, resulting in the total field being lowered, as the -4 mA data extremity (blue data points) clearly shows.

The dashed lines represent the theoretical predictions, which itself is calculated

through the Biot-Savart law,

$$\mathbf{B(r)} = \frac{\mu_0}{4\pi} \int \frac{I\,d\mathbf{l} \times \hat{\mathbf{r}}}{\mathbf{r.r}}, \tag{6.2}$$

where I is the applied current along increment d$\mathbf{l}$, and $\mathbf{r}$ is the position with unit vector $\hat{\mathbf{r}}$. Three straight wires $\mathbf{B(r)}_1$, $\mathbf{B(r)}_2$ and $\mathbf{B(r)}_3$ are used to approximate each wire segment's contribution for arbitrary positions in the cell, also being averaged over the optical path length that the probe beam passes through (L = 3 mm), providing $\overline{\mathrm{B}}$,

$$\overline{\mathrm{B}}(\mathrm{y,z}) = \frac{1}{\mathrm{L}} \int_0^{\mathrm{L}} ||\mathbf{B(r)}_1 + \mathbf{B(r)}_2 + \mathbf{B(r)}_3||\,d\,\mathrm{z}. \tag{6.3}$$

Atoms at the front face of the cell will experience a slightly different field from those at the back face, which is closer to the magnetic field source. Hence, the measurement is an overall average of the field experienced as a result of the probe beam traversing through the 3 mm path length. The theoretical calculation supposes the wire segments are 4.5 mm from the centre of the cell, matching the experimental condition. Deviations in the magnetic field experienced by the probe beam will differ depending on the thickness of the MEMS cell. A shorter optical path length would lead to a reduction of this averaging effect, however the sensitivity performance would be negatively impacted. The model does exhibit a slight deviation from the experimental data, which is particularly evident towards the right edge of the cell. An external connecting wire (not visible in the image or included in the theoretical calculation) will be the main cause of this due to the current flowing this interfering with the measurement.

Figure 6.5 (b) presents the same data with the background and mean values of each applied current both subtracted. The theoretical predictions also do not account for wire deformities which are noticeable from viewing the central wire configuration in Fig. 6.3 (b). Nonetheless, the data highlights the influence of each adjacent wire and the contrast from the opposing current flow as the probe is translated across.

6.4   2D Image Mapping

Generating a 2D image provides more valuable insights into the source of a magnetic field. Moreover, an ability to analyse magnetic field sources or patterns without the necessity of magnetic shielding in real-world conditions would result in substantial cost savings. Considering this perspective, the bias field was elevated to around 50 µT, and the copper wire was adjusted into the cross-wire configuration. This construction is depicted in Fig. 6.3 (c) with the wire placed 4.5 mm from the centre of the vapour cell, maintaining consistency with the 1D scan. The mirror was tilted vertically, enabling translation of the beam along the z-axis, facilitating the 2D image. The vapour cell was situated approximately 0.5 m from the scanning mirror, rendering the angle deviation of the beam traversing through the cell as insignificant. The vertical positions of the beam along the z-axis were calibrated using a CMOS camera (Thorlabs), which was temporarily placed at the position of the cell in order to photograph the beam. Using the camera's pixel size and the number of pixels illuminated by the beam, the respective distance between the camera and scanning mirror was used to calculate the adjustment required to traverse the beam's vertical position in 1 mm increments. This was methodically adjusted between each z-axis translation (5 vertical positions in total) to preserve the measurements accuracy and repeatability.
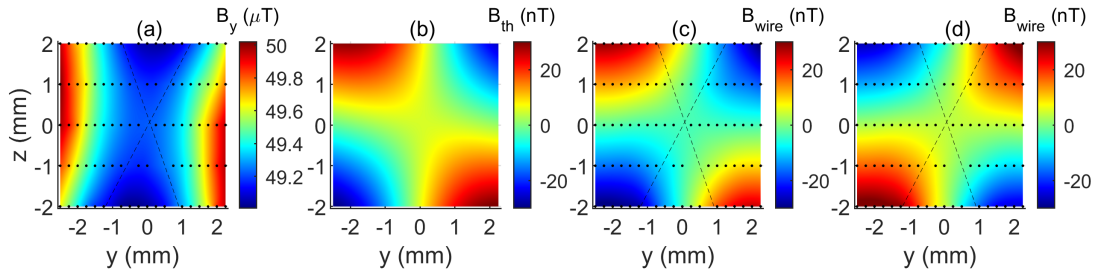
Figure 6.6: 2D magnetic image reconstruction from the cross-wire configuration depicted in Fig. 6.3 (c). (a) depicts the OPM output with 3.08 mA current applied through the wire. The bias field of $\approx$ 50 µT increases the magnetic gradient, which causes the majority of the field variation along the y-axis. (b) Theoretical field distribution emanating from the wire when 3.08 mA of current is applied. (c) and (d) display measured field distributions after background subtraction using currents of 3.08 mA and -3.13 mA respectively. Interpolation is used to enhance data visualisation.

117

Figure 6.6 (a) presents the total field measured across the vapour cell when a bias field of $\vec{B_0} \approx 50$ µT was applied in conjunction with passing a current of 3.08 mA through the wire. Immediately noticeable is the substantial magnetic field gradient present within the vapour cell, which greatly increased due to the heightened bias field. The distinct contribution arising solely from the current passing through the wire becomes apparent when examining Figures 6.6 (c) and (d), which represent the currents of 3.08 mA and -3.13 mA, respectively after background subtraction. The disparity between these images is evident, with reversing of the current flow yielding an inverted magnetic field image in the expected manner. Adding these distributions results in a standard deviation of 1 nT, which was 1.7 % of the wires total field variation across the imaging area. The field range produced by the wire (approximately 60 nT) was ≈ 0.1 % of that produced by $\vec{B_0}$, yet it accounts for around 6% of the total field gradient across the cell represented in (a). The image produced in (c) closely resembles the theoretical expectation based on the Biot-Savart law which is displayed in (b). Slight discrepancies are present due to the imperfections in the wire arrangement, however, a clear similarity is observed.

6.4.1 AC Signal Reconstruction

The OPM has thus far demonstrated an ability to detect DC magnetic field changes from the various current configurations. However, there are potential applications where oscillating magnetic fields are present. Therefore, to showcase the OPM is this context, a 0.55 mA RMS current modulation at a frequency of 376 Hz was superimposed onto the static bias field. As previously discussed in Section 3.2.2, it is important to note that the frequency and phase response of the sensor do not remain entirely flat within the Nyquist limited bandwidth. They are both influenced by the signal processing strategy employed. A study examining the anticipated OPM response resulting from the 376 Hz modulation was conducted and is presented in Fig. 6.7 (a).

Simulated data (purple) was created using a model which accounts for modulation of the Larmor frequency (black trace). The Larmor frequency (i.e. the magnetic field) is evaluated using the same nonlinear fitting technique applied to the experimental

118

data. The applied modulation results in each FID cycle sampling the modulation field at a different phase, therefore, the field changes significantly within a single FID cycle. However, the model used to extract the Larmor frequency, which assumes a single frequency component, depends on which segment of the modulation field is sampled during the readout stage. The frequency determination is weighted as a function of the exponential decay envelope caused by T_2 depolarisation. To ensure a consistent processing strategy when determining the magnetic field, the time stamp is set at the beginning of each FID cycle, i.e. the first value commences at t = 0.
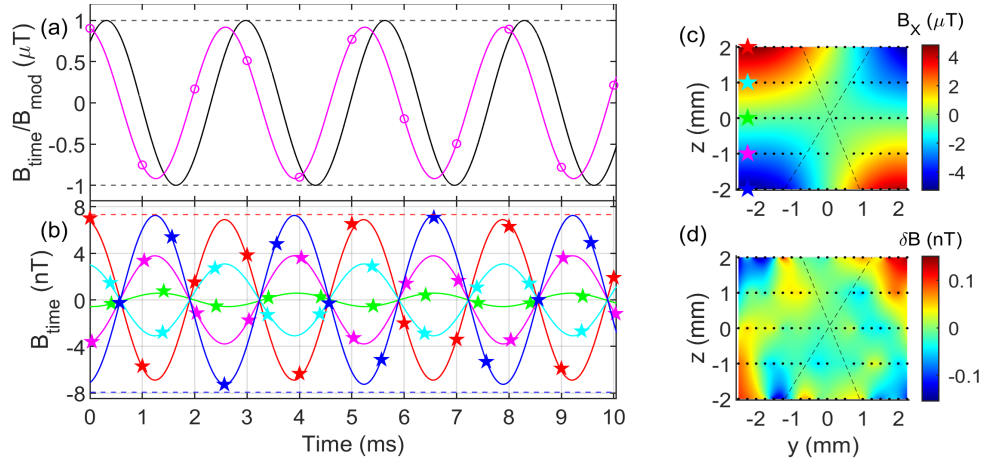
Figure 6.7: AC magnetic field reconstruction. (a) Simulated OPM response (purple) and corresponding fit to a modulation with amplitude B_m (black). (b) Experimental data over the first 10 ms recorded at various probe beam positions specified by the markers in (c), along with the respective sinusoidal fits. The dashed lines indicate the DC response measured for the red (top) and blue (bottom) positions. (c) Recovered magnetic field distribution produced by a 0.55 mA RMS current modulation at 376 Hz. (d) Deviation between the DC and AC field components after scaling, due to the current amplitudes and frequency response at 376 Hz.

In Fig. 6.7 (b), the magnetic field time series covering the initial 10 milliseconds is displayed for the experimental data, collected at specific probe beam positions denoted by the markers in Fig. 6.7 (c). Here the red data set is representative of the simulated phase and amplitude response from (a). The obtained signal amplitude undergoes a π phase flip as the probe beam is traversed along the vapour cell, where the current flowing in the opposite direction from the other wire segment starts to exert influence.

The dashed lines (red and blue) denote the DC response at the corresponding beam positions after scaling due to the AC current being approximately 5.6 x lower than that of the DC offset. Fig. 6.7 (c) depicts the AC field amplitude, B_x, extracted at each probe beam position across the cell through software demodulation. The AC magnetic image, aligns with the DC counterpart (Fig. 6.6 (c)), affirming the OPM's capability to also capture the AC field data. In Fig. 6.7 (d), a comparison between the DC and AC amplitudes at each position is illustrated, revealing a small fluctuation (approximately 0.6%) in the overall field variation attributed to the wire. This comparison takes into account the minor frequency-dependent roll-off effect, highlighted previously in Section 3.2.2.

6.5 Discussion

The optimised sensitivity performance of the OPM in this system is showcased in Fig. 6.8. A sensitivity of 0.43 pT/$\sqrt{\text{Hz}}$ is found at the centre of the vapour cell, in the region where maximum optical pumping occurs. The AC signal peak is immediately spotted in the frequency domain, in addition to the previously described magnetic noise peaks (see Section 3.3.2). An advantage that arises in performing these experiments at higher frequency is that no background subtraction is required, and a flat region of the noise spectrum can be selected. The AC demonstration highlights the effectiveness of this OPM in imaging high-frequency magnetic sources at geomagnetic field strengths. Successful mapping of both 1D and 2D image planes, with < 0.5 pT /$\sqrt{\text{Hz}}$ sensitivity demonstrates the sensors precision and extensive dynamic range. Additionally, the image has been successfully reconstructed with 175 µm spatial resolution. All of these factors show promise for future utilisation in unshielded magnetic imaging applications.
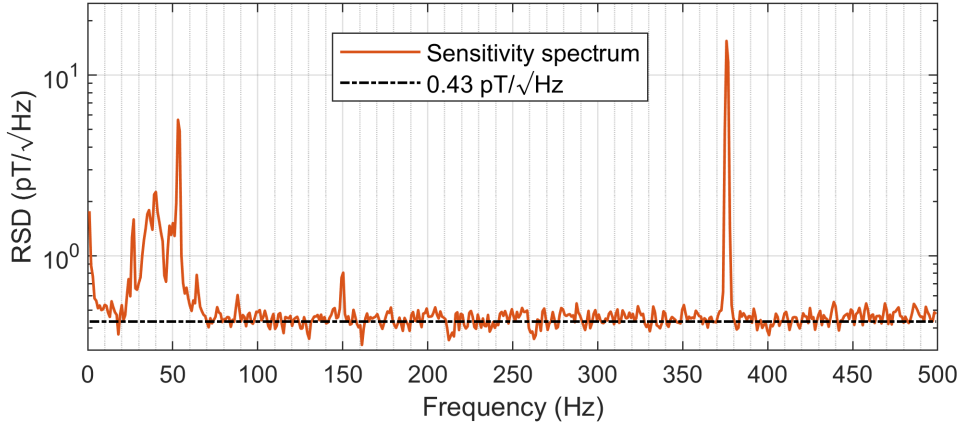
Figure 6.8: Sensitivity performance of the OPM in an approximate 50 µT bias field. This represents the optimal sensitivity performance (i.e. taken at a central region with optimal optical pumping efficiency), with the observed 376 Hz AC signal.

Both double and multi-pass systems have been shown to to increase the sensitivity of large vapour cells [123,124]. Additionally, MEMS vapour cells fabricated with reflective mirrors have been reported on in [48]. These have been successfully implemented in a portable OPM system, benefiting from the double pass signal improvement [88]. In future experiments, aligning the probe beam through the vapour cell in a double pass configuration would enhance the image reconstruction. This arrangement would simultaneously circumvent the obstruction of light caused by the imaging source (i.e. the cross-wire), and improve the sensitivity through increasing the optical rotation, owing to the greater optical path length. Placing a reflector on the back surface of a vapour cell prior to the imaging source would address these accessibility issues. This may be an invaluable tool for PCB inspection and quality assurance tests of integrated circuits (ICs). Their current output could be swiftly assessed in a production line environment by comparing them to already confirmed functional devices.

A more uniform pump beam intensity profile would improve the homogeneity in the optical pumping dynamics across the cell. Expanding the pump beam further to encompass the full portion of the cell would result in an isotropic spatial (sensitivity) profile. However, the reduced optical intensity and beam clipping at the edges of the cell would result in a lower spin-polarisation and sensitivity. Beam shaping techniques

such as employing a flat-top profile [125], sized to the cell dimensions, would avoid the clipping issues whilst maintaining a homogeneous spatial spin-polarisation. Again, however, this more complex beam shaping scheme would also induce optical losses. Instead, merging both the pump and probe beams within the same optical fibre, enabling simultaneous beam translation would guarantee that each spatial position experiences probing with maximum optical pumping efficiency. An effective design that provides smooth system integration could be to use a modular approach, where the optical components are separated from the interchangeable sensor heads. In this manner, a laboratory based platform such as this could be utilised for characterising a variety of electronic components, specifically in battery diagnostics [126].

Data collection efficiency and therefore image reconstruction speeds could be improved in future configurations through the use of technologies such as digital micromirror devices (DMD)s, which can deliver kHz refresh rates [127]. Spatially varying beam patterns would illuminate the cell and be captured on a single pixel detector i.e. a photodetector. The separate spatial light modes could be analysed to assess the Larmor frequency variation across the image source. Through correlating symmetries in the light modes with the magnetic field data, more complex and noteworthy images could be successfully mapped out.

Chapter 7

Summary and Outlook

This thesis has described a dual-beam FID magnetometer attaining excellent magnetic sensitivity performance. Conducted in a shielded laboratory setting, the magnetometer demonstrates near-optimal performance by reducing sources of magnetic noise. The experiment has yielded $fT/\sqrt{Hz}$ sensitivity levels matching the limit set by the CRLB. Moreover, these results were obtained at a field strength of 50 µT, chosen to emulate the Earth's magnetic amplitude. Thus, a benchmark for future real-world sensing using an FID configuration has been established. Notably, this extends to both 3 mm and 6 mm thick Cs MEMS vapour cells, with the latter exhibiting a peak sensitivity of 118 ± 11 $fT/\sqrt{Hz}$.

Additionally, the system exhibits photon shot-noise performance levels for up to $\approx$ 1 mW of probe light impinging on the detector i.e. the transmitted light after losses incurred through the vapour cell. In addition to the optical noise, magnetic noise in the system was also characterised in Chapter 3. The three-layers of µ-metal magnetic shielding is sufficient for demonstrating the capability of this finite field sensor. However, improvements in the achievable precision across the full Nyquist limited bandwidth range i.e. in the regions of technical noise would likely be found with additional shield layers.

An inventive method of producing a strong magnetic field pulse was showcased to simultaneously improve spin-polarisation while also raising the cell temperature. This innovative approach capitalises on the sensor's dead-time necessary for optical

pumping. Consequently, it not only extends the dynamic range, enhances the SNR, and improves sensitivity, but also addresses the practicality of incorporating heating into the system, providing a valuable benefit. Critically, rapid demagnetisation takes place upon switching this pulse off, preventing any influence on the sensor's noise floor from any lingering magnetic field.

The capability to temporally decouple the lasers grants independent control of the pump and probe, enabling optimal operation of each. Employing intense optical pumping on $F = 3$ to F' provided the most effective pumping method, enabling the extraction of the Larmor precession frequency using a FID fit consisting of a single sinusoid. Conversely, when pumping on $F = 4$ to F', a substantial atomic distribution was observed between both ground-state hyperfine levels. In this domain, two distinct atomic precession frequencies become observable and measurable. While this setup is not recommended for magnetometer operation, it can be utilised when the system is employed as a comagnetometer. Sub-pT/$\sqrt{\text{Hz}}$ levels were demonstrated using the system in this configuration.

In addition to examining different cell thicknesses, various N_2 buffer gas pressures have been investigated throughout this work. Chapter 5 presented OPM measurement results after laser irradiation of Cs dispenser pills housed in 6 mm cells. This was undertaken with an extensive characterisation of the cell as a function of N_2 pressure. Primarily, the focus was extracting the intrinsic longitudinal relaxation rate, γ_{10}, which required effective suppression of spin-exchange collisions. γ_{10} was minimised at $N_2 = 115$ Torr. Furthermore, a sensitivity assessment for each N_2 pressure was undertaken. Under identical experimental conditions, where N_2 was the sole variable, the cells consistently exhibited sensitivities of approximately 140 fT/$\sqrt{\text{Hz}}$.

Future work will seek to test cells with higher buffer gas contents. Higher pressures have been shown to boost the sensitivity performance of SERF magnetometers by 3 fT/$\sqrt{\text{Hz}}$/ Torr within the UoS's atomic magnetometry research group [128]. Similarly, higher pressures reduce the atomic diffusion time which is beneficial for magnetic imaging. Therefore, assessing the upper pressure limit which maximises performance will be valuable for both zero and finite field sensors. Furthermore, the newly developed

buffer gas tuning process can enable optimal pressures to be reached for a given cell geometry and magnetometer application, post fabrication. This will be particularly beneficial for gradiometric configurations where close to identical buffer gas pressures of separate cells are targeted. Furthermore, equivalent buffer gas pressures eliminate systematic magnetic gradient effects in comagnetometers.

The versatility of the sensor was showcased in Chapter 6, where a magnetic field imaging demonstration was conducted. Simple imaging sources were successfully reconstructed, highlighting the sensors viability for future magnetic imaging applications. The sensor effectively captured both DC and AC magnetic fields, characterising the field produced by a copper wire placed in close proximity to the cell. Future work will aim to enhance these results through more efficient data collection e.g. using DMDs, improving data collection efficiency. This will hopefully lead to future sensor integration in applications where the compact nature of MEMS vapour cells can offer excellent spatial resolution for imaging various sources. Diagnostics of batteries and electronic circuits are a sensible next step.

The FID scheme offers the capability for absolute field measurements in settings where accuracy is prioritised, with the obtainable sensitivities also extremely promising. Integration with MEMS vapour cells could streamline scalable deployment in various fields, including navigation, geophysical surveying, and mineral exploration. Unshielded, real-world sensing is the ultimate objective for MEMS cell technology with a vast number of sensors immediately available after a successful wafer fabrication. Research and development of these has the potential to drive meaningful advancements in magnetic sensing outside of the laboratory and into these areas.

Bibliography

[1] M. Caruso, C. Smith, T. Bratland, *et al.*, "A new perspective on magnetic field sensing," *Sensors (Peterborough, NH)* **15**, 34–46 (1998).

[2] M. A. Khan, J. Sun, B. Li, *et al.*, "Magnetic sensors - A review and recent technologies," *Engineering Research Express* **3**, 022005 (2021).

[3] H. Korth, K. Strohbehn, F. Tejada, *et al.*, "Miniature atomic scalar magnetometer for space based on the rubidium isotope 87Rb," *Journal of Geophysical Research: Space Physics* **121**, 7870–7880 (2016).

[4] H. Becker, "From nanotesla to picotesla - A new window for magnetic prospecting in archaeology," *Archaeological Prospection* **2**, 217–228 (1995).

[5] M. Nabighian, M. Ander, V. Grauch, *et al.*, "75th Anniversary - Historical development of the gravity method in exploration," *Geophysics* **70** (2005).

[6] S. Billings, C. Pasion, S. Walker, *et al.*, "Magnetic models of unexploded ordnance," *IEEE Transactions on Geoscience and Remote Sensing* **44**, 2115–2124 (2006).

[7] H. Koch, "Recent advances in magnetocardiography," *Journal of Electrocardiology* **37**, 117 – 122 (2004).

[8] I. Tavarozzi, S. Comani, C. Gratta, *et al.*, "Magnetocardiography: Current status and perspectives. Part I: Physical principles and instrumentation," *Italian heart journal : Official journal of the Italian Federation of Cardiology* **3**, 75–85 (2002).

[9] G. Bison, N. Castagna, A. Hofer, *et al.*, "A room temperature 19-channel magnetic field mapping device for cardiac signals," *Applied Physics Letters* **95**, 173701 (2009).

[10] T. M. Tierney, N. Holmes, S. Mellor, *et al.*, "Optically pumped magnetometers: From quantum origins to multi-channel magnetoencephalography," *NeuroImage* **199**, 598–608 (2019).

[11] H. Xia, A. Ben-Amar Baranga, D. Hoffman, *et al.*, "Magnetoencephalography with an atomic magnetometer," *Applied Physics Letters* **89**, 211104 (2006).

[12] M. Hämäläinen, R. Hari, R. Ilmoniemi, *et al.*, "Magnetoencephalography: Theory, instrumentation, and applications to noninvasive studies of the working human brain," *Reviews of Modern Physics* **65**, 413 (1993).

[13] D. Cohen, "Magnetoencephalography: Detection of the Brain's Electrical Activity with a Superconducting Magnetometer," *Science* **175**, 664–666 (1972).

[14] D. Budker and M. Romalis, "Optical Magnetometry," *Nature Physics* **3**, 227–234 (2006).

[15] L.-A. Liew, S. Knappe, J. Moreland, *et al.*, "Microfabricated alkali atom vapor cells," *Applied Physics Letters* **84**, 2694–2696 (2004).

[16] J. Kitching, "Chip-scale atomic devices," *Applied Physics Reviews* **5**, 031302 (2018).

[17] M. J. Brookes, J. Leggett, M. Rea, *et al.*, "Magnetoencephalography with optically pumped magnetometers (OPM-MEG): the next generation of functional neuroimaging," *Trends in Neurosciences* **45**, 621–634 (2022).

[18] H. B. Dang, A. C. Maloof, and M. V. Romalis, "Ultrahigh sensitivity magnetic field and magnetization measurements with an atomic magnetometer," *Applied Physics Letters* **97**, 151110 (2010).

[19] A. Kastler, "Optical Methods of Atomic Orientation and of Magnetic Resonance," *Journal of the Optical Society of America* **47**, 460–465 (1957).

[20] S. Pustelny, *Nonlinear magneto-optical effects.* PhD thesis, Jagiellonian University, Kraków Poland (2007).

[21] J. R. Zimmerman and D. Williams, "Nuclear Gyromagnetic Ratios of Be^9, Rb^{85}, Rb^{87}, and Cs^{133}," *Physical Review* **75**, 699–699 (1949).

[22] V. K. Shah and R. T. Wakai, "A compact, high performance atomic magnetometer for biomedical applications," *Physics in Medicine & Biology* **58**, 8153 (2013).

[23] U. Marhl, T. Sander, and V. Jazbinšek, "Simulation Study of Different OPM-MEG Measurement Components," *Sensors* **22**, 3184 (2022).

[24] M. J. Brookes, E. Boto, M. Rea, *et al.*, "Theoretical advantages of a triaxial optically pumped magnetometer magnetoencephalography system," *NeuroImage* **236**, 118025 (2021).

[25] T. Wang, D. F. J. Kimball, A. O. Sushkov, *et al.*, "Application of spin-exchange relaxation-free magnetometry to the Cosmic Axion Spin Precession Experiment," *Physics of the Dark Universe* **19**, 27–35 (2018).

[26] D. Hunter, S. Piccolomo, J. D. Pritchard, *et al.*, "Free-Induction-Decay Magnetometer Based on a Microfabricated Cs Vapor Cell," *Physical Review Applied* **10**, 014002 (2018).

[27] Z. Grujić, P. Koss, G. Bison, *et al.*, "A sensitive and accurate atomic magnetometer based on free spin precession," *The European Physical Journal D* **69**, 135 (2015).

[28] V. Gerginov, M. Pomponio, and S. Knappe, "Scalar magnetometry below 100 fT/Hz$^{1/2}$ in a microfabricated cell," *IEEE Sensors Journal* **20**, 12684–12690 (2020).

[29] F. Malz and H. Jancke, "Validation of quantitative NMR," *Journal of Pharmaceutical and Biomedical Analysis* **38**, 813–823 (2005).

[30] M. Ledbetter, I. Savukov, D. Budker, *et al.*, "Zero-field remote detection of NMR with a microfabricted atomic magnetometer," *Proceedings of the National Academy of Sciences of the United States of America* **105**, 2286–90 (2008).

[31] N. Wilson, C. Perrella, R. Anderson, *et al.*, "Wide-bandwidth atomic magnetometry via instantaneous-phase retrieval," *Physical Review Research* **2**, 013213 (2020).

[32] D. Hunter, M. S. Mrozowski, A. McWilliam, *et al.*, "Optical pumping enhancement of a free-induction-decay magnetometer," *Journal of the Optical Society of America B* **40**, 2664–2673 (2023).

[33] D. Hunter, T. E. Dyer, and E. Riis, "Accurate optically pumped magnetometer based on Ramsey-style interrogation," *Optics Letters* **47**, 1230–1233 (2022).

[34] M. Abdel Hafiz, G. Coget, M. Petersen, *et al.*, "Toward a High-Stability Coherent Population Trapping Cs Vapor-Cell Atomic Clock Using Autobalanced Ramsey Spectroscopy," *Physical Review Applied* **9**, 064002 (2018).

[35] W. Chalupczak, R. M. Godun, P. Anielski, *et al.*, "Enhancement of optically pumped spin orientation via spin-exchange collisions at low vapor density," *Physical Review Applied* **85**, 043402 (2012).

[36] S. Ingleby, C. O'Dwyer, P. Griffin, *et al.*, "Vector Magnetometry Exploiting Phase-Geometry Effects in a Double-Resonance Alignment Magnetometer," *Physical Review Applied* **10**, 034035 (2018).

[37] C. O'Dwyer, S. Ingleby, I. Chalmers, *et al.*, "A feed-forward measurement scheme for periodic noise suppression in atomic magnetometry," *Review of Scientific Instruments* **91**, 045103 (2020).

[38] E. Breschi, Z. Grujić, and A. Weis, "In situ calibration of magnetic field coils using free-induction decay of atomic alignment," *Applied Physics B* **115**, 85–91 (2014).

[39] L. Chen, B. Zhou, G. Lei, *et al.*, "A method for calibrating coil constants by using the free induction decay of noble gases," *AIP Advances* **7**, 075315 (2017).

[40] V. G. Lucivero, A. Zanoni, G. Corrielli, *et al.*, "Laser-written vapor cells for chip-scale atomic sensing and spectroscopy," *Optics Express* **30**, 27149–27163 (2022).

[41] J. Mora, A. Cobos, D. Fuentes, *et al.*, "Measurement of the Ratio between g-Factors of the Ground States of 87Rb and 85Rb," *Annalen der Physik* **531**, 1800281 (2019).

[42] J.-M. Leger, F. Bertrand, T. Jager, *et al.*, "Swarm Absolute Scalar and Vector Magnetometer Based on Helium 4 Optical Pumping," *Procedia Chemistry* **1**, 634–637 (2009). Proceedings of the Eurosensors XXIII conference.

[43] K.-M. C. Fu, G. Z. Iwata, A. Wickenbrock, *et al.*, "Sensitive magnetometry in challenging environments," *AVS Quantum Science* **2**, 044702 (2020).

[44] J. C. Allred, R. N. Lyman, T. W. Kornack, *et al.*, "High-Sensitivity Atomic Magnetometer Unaffected by Spin-Exchange Relaxation," *Physical Review Letters* **89**, 130801 (2002).

[45] R. Mhaskar, S. Knappe, and J. Kitching, "A low-power, high-sensitivity micromachined optical magnetometer," *Applied Physics Letters* **101**, 241105 (2012).

[46] V. Lucivero, W. Lee, N. Dural, *et al.*, "Femtotesla Direct Magnetic Gradiometer Using a Single Multipass Cell," *Physical Review Applied* **15**, 014004 (2021).

[47] M. Limes, E. Foley, T. Kornack, *et al.*, "Portable Magnetometry for Detection of Biomagnetism in Ambient Environments," *Physical Review Applied* **14**, 011002 (2020).

[48] T. Dyer, S. J. Ingleby, C. Dunare, *et al.*, "Micro-fabricated caesium vapor cell with 5mm optical path length," *Journal of Applied Physics* **132**, 204401 (2022).

[49] S. Dyer, P. F. Griffin, A. S. Arnold, *et al.*, "Micro-machined deep silicon atomic vapor cells," *Journal of Applied Physics* **132**, 134401 (2022).

[50] M. T. Graf, D. F. Kimball, S. M. Rochester, *et al.*, "Relaxation of atomic polarization in paraffin-coated cesium vapor cells," *Physical Review Applied* **72**, 023401 (2005).

[51] D. Hunter, *Chip-Scale Atomic Magnetometer Based on Free-Induction-Decay*. PhD thesis, University of Strathclyde, Glasgow, Scotland (2019).

[52] S. J. Seltzer, *Developments in Alkali-Metal Atomic Magnetometry*. PhD thesis, Princeton University, New Jersey (2008).

[53] G. Bison, *Development of an optical cardio-magnetometer*. PhD thesis, University of Fribourg, Switzerland (2004).

[54] S. Dyer, A. McWilliam, D. Hunter, *et al.*, "Nitrogen buffer gas pressure tuning in a micro-machined vapor cell," *Applied Physics Letters* **123**, 074001 (2023).

[55] D. Hunter, C. Perrella, A. McWilliam, *et al.*, "Free-induction-decay magnetic field imaging with a microfabricated Cs vapor cell," *Optics Express* **31**, 33582–33595 (2023).

[56] J. P. McGilligan, K. Gallacher, P. F. Griffin, *et al.*, "Micro-fabricated components for cold atom sensors," *Review of Scientific Instruments* **93**, 091101 (2022).

[57] L. Liew, J. Moreland, and V. Gerginov, "Wafer-level filling of microfabricated atomic vapor cells based on thin-film deposition and photolysis of cesium azide," *Applied Physics Letters* **90**, 114106 (2007).

[58] D. Steck, "Cesium D line data," https://steck.us/alkalidata/ (2010).

[59] B. Julsgaard, J. Sherson, J. L. Sørensen, *et al.*, "Characterizing the spin state of an atomic ensemble using the magneto-optical resonance method," *Journal of Optics B: Quantum and Semiclassical Optics* **6**, 5 (2003).

[60] G. Breit and I. I. Rabi, "Measurement of Nuclear Spin," *Physical Review* **38**, 2082–2083 (1931).

[61] A. Fabricant, I. Novikova, and G. Bison, "How to build a magnetometer with thermal atomic vapor: a tutorial," *New Journal of Physics* **25**, 025001 (2023).

[62] P. Siddons, C. Adams, C. Ge, *et al.*, "Absolute absorption on rubidium D lines: comparison between theory and experiment," *Journal of Physics B: Atomic, Molecular and Optical Physics* **41**, 155004 (2008).

[63] S. Piccolomo, *Chip-Scale Atomic Magnetometer*. PhD thesis, University of Strathclyde, Glasgow, Scotland (2016).

[64] G. A. Pitz, D. E. Wertepny, and G. P. Perram, "Pressure broadening and shift of the cesium D_1 transition by the noble gases and N_2, H_2, HD, D_2, CH_4, C_2H_6, CF_4, and ^{3}He," *Physical Review Applied* **80**, 062718 (2009).

[65] A. Andalkar and R. B. Warrington, "High-resolution measurement of the pressure broadening and shift of the Cs D_1 and D_2 lines by N_2 and He buffer gases," *Physical Review Applied* **65**, 7 (2002).

[66] D. W. Preston, "Doppler-free saturated absorption: Laser spectroscopy," *American Journal of Physics* **64**, 1432–1436 (1996).

[67] D. Budker and D. Kimball, *Optical Magnetometry*, Cambridge University Press (2013).

[68] A. F. Molisch, B. P. Oehry, W. Schupita, *et al.*, "Radiation trapping in atomic vapours in finite-cylinder vapour cells excited by a laser beam," *Journal of Physics B: Atomic, Molecular and Optical Physics* **30**, 1879 (1997).

[69] M. A. Rosenberry, J. P. Reyes, D. Tupa, *et al.*, "Radiation trapping in rubidium optical pumping at low buffer-gas pressures," *Physical Review Applied* **75**, 023401 (2007).

[70] V. Schultze, T. Scholtes, R. IJsselsteijn, *et al.*, "Improving the sensitivity of optically pumped magnetometers by hyperfine repumping," *Journal of the Optical Society of America B* **32**, 730–736 (2015).

[71] T. Scholtes, S. Woetzel, R. IJsselsteijn, *et al.*, "Intrinsic relaxation rates of polarized Cs vapor in miniaturized cells," *Applied Physics B* **117**, 211–218 (2014).

[72] J. C. Allred, R. N. Lyman, T. W. Kornack, *et al.*, "High-Sensitivity Atomic Magnetometer Unaffected by Spin-Exchange Relaxation," *Physical Review Letters* **89**, 130801 (2002).

[73] N. D. Bhaskar, J. Pietras, J. Camparo, *et al.*, "Spin Destruction in Collisions between Cesium Atoms," *Physical Review Letters* **44**, 930–933 (1980).

[74] N. D. Bhaskar, J. Camparo, W. Happer, *et al.*, "Light narrowing of magnetic resonance lines in dense, optically pumped alkali-metal vapor," *Physical Review Applied* **23**, 3048–3064 (1981).

[75] T. Scholtes, V. Schultze, R. IJsselsteijn, *et al.*, "Light-narrowed optically pumped M_x magnetometer with a miniaturized Cs cell," *Physical Review Applied* **84**, 043416 (2011).

[76] M. S. Mrozowski, I. C. Chalmers, S. J. Ingleby, *et al.*, "Ultra-low noise, bi-polar, programmable current sources," *Review of Scientific Instruments* **94**, 014701 (2023).

[77] B. S. Mathur, H. Tang, and W. Happer, "Light Shifts in the Alkali Atoms," *Physical Review* **171**, 11–19 (1968).

[78] F. Bloch, "Nuclear Induction," *Physical Review* **70**, 460–474 (1946).

133

[79] S. Rochester, M. Ledbetter, T. Zigdon, *et al.*, "Orientation-to-alignment conversion and spin squeezing," *Physical Review A* **85**, 022125 (2011).

[80] A. Weis, G. Bison, and A. S. Pazgalev, "Theory of double resonance magnetometers based on atomic alignment," *Physical Review Applied* **74**, 033401 (2006).

[81] S. L. AN118, "Improving ADC resolution by oversampling and averaging," https://www.silabs.com/documents/public/application-notes/an118.pdf (2019).

[82] I. Hughes and T. Hase, *Measurements and Their Uncertainties: A Practical Guide to Modern Error Analysis*, OUP Oxford (2010).

[83] D. Hunter, R. Jiménez-Martínez, J. Herbsommer, *et al.*, "Waveform reconstruction with a Cs based free-induction-decay magnetometer," *Optics Express* **26**, 30523–30531 (2018).

[84] P. Welch, "The use of fast Fourier transform for the estimation of power spectra: A method based on time averaging over short, modified periodograms," *IEEE Transactions on Audio and Electroacoustics* **15**, 70–73 (1967).

[85] Zurich Instruments, "Principles of lock-in detection and the state of the art," https://www.zhinst.com/europe/en/resources/whitepapers (2016).

[86] C. Gemmel, W. Heil, S. Karpuk, *et al.*, "Ultra-sensitive magnetometry based on free precession of nuclear spins," *The European Physical Journal D* **57**, 303–320 (2010).

[87] A. Jaufenthaler, T. Kornack, V. Lebedev, *et al.*, "Pulsed Optically Pumped Magnetometers: Addressing Dead Time and Bandwidth for the Unshielded Magnetorelaxometry of Magnetic Nanoparticles," *Sensors* **21**, 1212 (2021).

[88] S. Ingleby, P. Griffin, T. Dyer, *et al.*, "A digital alkali spin maser," *Scientific Reports* **12**, 1–7 (2022).

[89] D. Budker, W. Gawlik, D. F. Kimball, *et al.*, "Resonant nonlinear magneto-optical effects in atoms," *Reviews of Modern Physics* **74**, 1153–1201 (2002).

[90] V. G. Lucivero, P. Anielski, W. Gawlik, *et al.*, "Shot-noise-limited magnetometer with sub-picotesla sensitivity at room temperature," *Review of Scientific Instruments* **85**, 113108 (2014).

[91] Y. Chen, L. Zhao, N. Zhang, *et al.*, "Single beam Cs-Ne SERF atomic magnetometer with the laser power differential method," *Optics Express* **30**, 16541–16552 (2022).

[92] M. Auzinsh, A. Berzins, R. Ferber, *et al.*, "Alignment-to-orientation conversion in a magnetic field at nonlinear excitation of the D2 line of rubidium: Experiment and theory," *Physical Review Applied* **91**, 053418 (2015).

[93] V. Acosta, M. P. Ledbetter, S. M. Rochester, *et al.*, "Nonlinear magneto-optical rotation with frequency-modulated light in the geophysical field range," *Physical Review Applied* **73**, 053404 (2006).

[94] G. Bao, A. Wickenbrock, S. Rochester, *et al.*, "Suppression of the Nonlinear Zeeman Effect and Heading Error in Earth-Field-Range Alkali-Vapor Magnetometers," *Physical Review Letters* **120**, 033202 (2018).

[95] R. Zhang, T. Wu, J. Chen, *et al.*, "Frequency Response of Optically Pumped Magnetometer with Nonlinear Zeeman Effect," *Applied Sciences* **10**, 7031 (2020).

[96] X. Fang, K. Wei, Y. Zhai, *et al.*, "Analysis of effects of magnetic field gradient on atomic spin polarization and relaxation in optically pumped atomic magnetometers," *Optics Express* **30**, 3926–3940 (2022).

[97] S. Pustelny, D. F. Jackson Kimball, S. M. Rochester, *et al.*, "Influence of magnetic-field inhomogeneity on nonlinear magneto-optical resonances," *Physical Review Applied* **74**, 063406 (2006).

[98] M. Rosner, D. Beck, P. Fierlinger, *et al.*, "A highly drift-stable atomic magnetometer for fundamental physics experiments," *Applied Physics Letters* **120**, 161102 (2022).

[99] B. Boashash, "Estimating and interpreting the instantaneous frequency of a signal," *Proceedings of the IEEE* **80**, 520–538 (1992).

[100] Y. Yang, W. Teng, J. Chen, *et al.*, "All-optical single-species cesium atomic comagnetometer with optical free induction decay detection," *Applied Physics B* **127**, 40 (2021).

[101] W. Lee, V. G. Lucivero, M. V. Romalis, *et al.*, "Heading errors in all-optical alkali-metal-vapor magnetometers in geomagnetic fields," *Physical Review Applied* **103**, 063103 (2021).

[102] T. Wu, J. W. Blanchard, D. F. Jackson Kimball, *et al.*, "Nuclear-Spin Comagnetometer Based on a Liquid of Identical Molecules," *Physical Review Letters* **121**, 023202 (2018).

[103] D. F. Jackson Kimball, D. Budker, T. E. Chupp, *et al.*, "Probing fundamental physics with spin-based quantum sensors," *Physical Review Applied* **108**, 010101 (2023).

[104] J. M. Brown, S. J. Smullin, T. W. Kornack, *et al.*, "New Limit on Lorentz- and CPT-Violating Neutron Spin Interactions," *Physical Review Letters* **105**, 151604 (2010).

[105] M. E. Limes, D. Sheng, and M. V. Romalis, "^{3}He$-^{129}$Xe Comagnetometery using ^{87}Rb Detection and Decoupling," *Physical Review Letters* **120**, 033401 (2018).

[106] Z. Wang, X. Peng, R. Zhang, *et al.*, "Single-Species Atomic Comagnetometer Based on Rb 87 Atoms," *Physical Review Letters* **124**, 193002 (2020).

[107] K. Jensen, V. M. Acosta, J. M. Higbie, *et al.*, "Cancellation of nonlinear Zeeman shifts with light shifts," *Physical Review Applied* **79**, 023406 (2009).

[108] L. M. Rushton, T. Pyragius, A. Meraki, *et al.*, "Unshielded portable optically pumped magnetometer for the remote detection of conductive objects using eddy current measurements," *Review of Scientific Instruments* **93**, 125103 (2022).

[109] H. Korth, K. Strohbehn, F. Tejada, *et al.*, "Miniature atomic scalar magnetometer for space based on the rubidium isotope 87Rb," *Journal of Geophysical Research: Space Physics* **121**, 7870–7880 (2016).

[110] E. Kroemer, M. A. Hafiz, V. Maurice, *et al.*, "Cs vapor microcells with Ne-He buffer gas mixture for high operation-temperature miniature atomic clocks," *Optics Express* **23**, 18373–18380 (2015).

[111] N. Beverini, P. Minguzzi, and F. Strumia, "Foreign-Gas-Induced Cesium Hyperfine Relaxation," *Physical Review Applied* **4**, 550–555 (1971).

[112] F. A. Franz and E. Lüscher, "Spin Relaxation of Optically Pumped Cesium," *Physical Review* **135**, A582–A588 (1964).

[113] F. A. Franz and C. E. Sooriamoorthi, "Spin relaxation within the $6^2P_{\frac{1}{2}}$ and $6^2S_{\frac{1}{2}}$ states of cesium measured by white-light optical pumping," *Physical Review Applied* **10**, 126–140 (1974).

[114] J. Kitching, S. Knappe, and L. Hollberg, "Miniature vapor-cell atomic-frequency references," *Applied Physics Letters* **81**, 553–555 (2002).

[115] N. Wilson, P. Light, A. Luiten, *et al.*, "Ultrastable Optical Magnetometry," *Physical Review Applied* **11**, 044034 (2019).

[116] R. Zhang, R. Mhaskar, K. Smith, *et al.*, "Portable Intrinsic Gradiometer for Ultra-Sensitive Detection of Magnetic Gradient in Unshielded Environment," *Applied Physics Letters* **116**, 143501 (2020).

[117] D. Sheng, A. R. Perry, S. P. Krzyzewski, *et al.*, "A microfabricated optically-pumped magnetic gradiometer," *Applied Physics Letters* **110**, 031106 (2017).

[118] J. M. Taylor, P. Cappellaro, L. Childress, *et al.*, "High-sensitivity diamond magnetometer with nanoscale resolution," *Nature Physics* **4**, 810–816 (2008).

[119] F. M. Stürner, A. Brenneis, T. Buck, *et al.*, "Integrated and Portable Magnetometer Based on Nitrogen-Vacancy Ensembles in Diamond," *Advanced Quantum Technologies* **4**, 2000111 (2021).

[120] G. Gbur and E. Wolf, "The Rayleigh range of partially coherent beams," *Optics Communications* **199**, 295–304 (2001).

[121] K. Kim, S. Begus, H. Xia, *et al.*, "Multi-channel atomic magnetometer for magnetoencephalography: A configuration study," *NeuroImage* **89**, 143–151 (2014).

[122] H.-F. Dong, J.-L. Chen, J.-M. Li, *et al.*, "Spin image of an atomic vapor cell with a resolution smaller than the diffusion crosstalk free distance," *Journal of Applied Physics* **125**, 243904 (2019).

[123] D. Sheng, S. Li, N. Dural, *et al.*, "Subfemtotesla Scalar Atomic Magnetometry Using Multipass Cells," *Physical Review Letters* **110**, 160802 (2013).

[124] S. Li, J. Liu, M. Jin, *et al.*, "A kilohertz bandwidth and sensitive scalar atomic magnetometer using an optical multipass cell," *Measurement* **190**, 110704 (2022).

[125] A. Laskin and V. Laskin, "Variable beam shaping with using the same field mapping refractive beam shaper," *Proceedings of SPIE - The International Society for Optical Engineering* **8236**, 81–90 (2012).

[126] M. G. Bason, T. Coussens, M. Withers, *et al.*, "Non-invasive current density imaging of lithium-ion batteries," *Journal of Power Sources* **533**, 231312 (2022).

[127] A. B. Ayoub and D. Psaltis, "High speed, complex wavefront shaping using the digital micro-mirror device," *Scientific Reports* **11**, 18837 (2021).

[128] R. Dawson, *Development of a single beam SERF magnetometer using caesium atoms for medical applications.* PhD thesis, University of Strathclyde, Glasgow, Scotland (2023).